Raymond and Beverly Sackler
Faculty of Exact Sciences
School of Physics and Astronomy

Research Thesis for a Degree "Doctor of Philosophy"

Dynamics of Driven Colloids

Submitted to the Senate of Tel Aviv University by

Tomer Goldfriend

Advisor: Prof. Haim Diamant

January 2017

This research was carried out under the supervision of
Professor Haim Diamant
School of Chemistry, Tel-Aviv University

In memory of my grandparents:
Samuel and Hadassa Irena Goldfriend; Eliyahu and Debora Dekel

— אֵצֵא לִי עַל כֵּן, בִּמְעִיל קַיִץ פָּשׁוּט, לְטַיֵּל בֵּין פִּילֵי הַשָּׁמַיִם. ("אל הפילים", נתן אלתרמן)

Abstract

Colloidal systems are composed of mesoscopic rigid particles (10nm-10μm in size) dispersed in a molecular, viscous fluid. Earlier studies on a pair of, or a system of many, driven colloids mostly focused on symmetric objects, such as spheres or spheroids. General treatment of driven, asymmetric colloids has been recently presented on a single object level, demonstrating how the coupling between translation, rotation and the external drive can yield new types of controllable transport phenomena. In this Thesis I study the flow-mediated interactions between arbitrarily shaped, driven colloids, and their effects on orientational alignment and collective dynamics of asymmetric non-Brownian suspensions.

In the first part of the work we explore the hydrodynamic interactions between two arbitrarily shaped objects, which are driven through a viscous fluid, in the limit of zero Reynolds number. We study rigorously the general properties and symmetries of the pair-mobility matrix governing the instantaneous relative linear and angular velocities of the two objects. We treat analytically the leading (monopolar and dipolar) interaction, affecting the pair response at large separation. We focus, in particular, on self-aligning objects— a large class of irregular objects whose asymmetric shape causes them to orient with an external constant force, or further synchronize with a forcing protocol that varies in time. We prove that the instantaneous hydrodynamic interaction linearly degrades the orientational alignment between two such objects. The time-dependent effects of hydrodynamic interactions are explicitly demonstrated via numerically calculated trajectories of model self-aligning objects composed of four point-like particles (stokeslets). In addition to the orientational effect, we find that the interplay between the orientational interaction and the translational one, in most cases, leads over time to repulsion between the two objects. Consequently, in the presence of time-dependent aligning protocols, the mutual degradation of alignment weakens as the two objects move away from each other, and full alignment is restored at long times.

These findings— the instantaneous relative linear velocity and the effective repulsion over time— lead us in the second part of the work to study in more detail the implication of hydrodynamic interactions on the translational response of two arbitrarily shaped objects. It is well known that in the case of two identical rigid spheres in an unbounded fluid at zero Reynolds number, the hydrodynamic interaction does not produce relative translation. We demonstrate that, more generally, such an effective pair-interaction vanishes in configurations with spatial inversion symmetry; for example, an enantiomorphic pair in mirror image positions has no relative translation. We show that the breaking of inversion symmetry by boundaries of the system accounts for the interactions between two spheres in confined geometries, as previously observed in experiments. The same general principle also provides new predictions for interactions in other object configurations near obstacles. We examine in detail the time-dependent relative translation of two self-aligning objects. We show that the typical repulsion for this class of objects is qualitatively different compared to the more symmetric case of uniform prolate spheroids. The mutual separation between the objects, in each case, evolves with a different asymptotic power law of time.

In the third part we show that the distinctive effects in the motion of irregular object pairs have an impact on the many-body dynamics of driven colloids. In a sedimenting suspension

comprising self-aligning objects, the anisotropic response of the objects to flow, caused by their tendency to align with gravity, act as a mechanism which directly suppresses concentration and velocity fluctuations. This allows the suspension to avoid the anomalous fluctuations predicted for suspensions of symmetric spheroids. We show, using fluctuating hydrodynamics, how the suppression of concentration fluctuations leads to a correlated, hyperuniform structure. For certain object shapes, the anisotropic response may act in the opposite direction, destabilizing uniform sedimentation.

The findings of this Thesis thus show sharp qualitative differences between driven colloids of symmetric shapes and of irregular ones — on the level of a pair of objects, as well as in the collective dynamics.

Acknowledgments

First and foremost, I would like to express my gratitude to Prof. Haim Diamant for introducing me to the field of soft matter physics and for his guidance throughout the last four and a half years. Haim, thank you for sharing with me your intriguing thoughts and insightful ideas. You taught me how asking the right physical questions can bring a simple result to open a window to new inquiries, or give a hint when it is a good time to move on to the next challenge. I am grateful to you for your sincere dedication in mentoring my way to independent research, and for your typical kindness.

I feel privileged to thank Prof. Thomas A. Witten for fruitful collaboration and illuminating discussions. I am grateful for having the unique experience to follow, and being motivated by, Tom's deep and creative line of thought.

I wish to thank my friends and colleagues, Oz, Yulia and Chen, for helpful discussions and useful suggestions.

I thank my parents Orna and Dov, and my brothers Amir, Roee, and Nir for their encouragement and support. Last, but certainly not least, I would like to thank my wife, love of my life, Neta— you were there all the way, during my frequent pessimistic times or at my rare optimistic moments, keeping my sanity throughout this journey. Finally, I cannot complete this list without mentioning my daughter Reut, who came into my life several weeks ago and opened up for me a new perspective on life.

Contents

Chapter 1

Introduction

1.1 Background

Muddy water, proteins in our body cells, or the ink which brings forth the hard-copy of this very Thesis, are all examples of colloidal systems— 10 nanometer to 10 micron sized objects dispersed in a molecular liquid. Colloidal suspensions exhibit ubiquitous equilibrium phenomena and non-equilibrium processes [1]. The coupling between the fluid-flow and the motion of the dispersed objects leads to rich and complex dynamics with wide applicability in the context of designing synthetic materials, e.g., modeling drug-delivery nano-agents [2], and in understanding emergent phenomena of biological materials, e.g., collective motion of bacteria [3, 4].

The thermal fluctuations of the molecular fluid lead to a stochastic (Brownian) motion of the colloids. In addition, the medium affects direct, e.g., electrostatic and Van-der-Waals interactions among the suspended objects; induces entropic interactions such as depletion forces; and gives rise to flow-mediated interactions, i.e., the response of an object to a flow generated by another object. The latter effect— termed *hydrodynamic interactions*— is long-ranged and plays a central role in colloidal systems, especially in non-equilibrium phenomena. The study of dynamical processes in suspensions is divided into two classes, intrinsically (self-propelled[1]) and externally driven objects. Generally, in both cases, the system constantly dissipates energy and therefore, is always out of thermal equilibrium. This Thesis focuses on the latter class of externally driven systems, and on physical scenarios in which the long-ranged hydrodynamic interactions prevails all other inter-particle interactions.

Commonly used driving mechanisms are simple body forces such as gravity (sedimentation) and centrifugal forces (centrifugation), electric fields (electrophoresis), thermal gradients

[1] Systems of self-propelled objects are known as "active matter" [5].

(thermophoresis), concentration gradients (diffusiophoresis) and shear flows. These underlie various related non-equilibrium processes in biological and synthetic materials, and have many technological applications. For instance, manipulation of DNA molecules and proteins such as transport, aggregation, and chiral separation of enantiomers [6, 7], are standard procedures in many biochemical or biophysical laboratories. Other examples are bed fluidization that is widely used in reactors and water treatment [8] or the electrophoretic ink which is used in certain electronic displays [9].

The transport of a single symmetric object is well established. The fundamental theories were instituted more than 100 years ago. For example, the calculation of the drag force on a sphere of radius ℓ, moving with velocity $\mathbf{V}$ through a fluid of viscosity η, was derived by Stokes in 1851, $\mathbf{F}_{\text{drag}} = -6\pi\eta\ell\mathbf{V}$. Another example is the analysis of a charged sphere transport in electrolyte due to an external electric field, which was derived by Helmholtz [10] in 1879 and Smoluchowski [11] in 1903.

In several cases, the theory was generalized to include the transport of objects with arbitrary shape [12–15]. While the study of symmetric objects underlies the physics of driven systems and provides a simple example of transport phenomena, exploring objects of arbitrary shape is more practical since many biological and synthetic colloidal objects are not symmetric. Moreover, the absence of symmetry in the shape of the object may sometimes yield new phenomena, such as: chiral separation by shear flow [16, 17] or by capillary electrophoresis [7, 18]; programming lock-and-key binding between two asymmetric colloids [19]; efficient transport of chiral magnetic objects subjected to a rotating magnetic field [2]; and the application of an external body force to rotationally synchronize initially incoherent system of chiral suspensions. The latter system will be one of the focuses of this Thesis.

The rest of this Chapter is organized as follows: In Sec. 1.2 we introduce the hydrodynamic description of the molecular liquid, specializing to the inertia-less (zero Reynolds number) regime that characterizes colloidal systems. The fundamental properties of externally driven colloidal phenomena are discussed in Sec. 1.3. Then we elaborate on the established theories and phenomena of driven colloids, which are relevant to the work to follow, separating the review to the levels of a single-object motion (Sec. 1.4), pair of objects dynamics (Sec. 1.5), and collective behavior (Sec. 1.6). In Sec. 1.7 we present a useful mathematical representation for the dynamics of asymmetric objects. In Sec. 1.8 we summarize the main notations and symbols that are used throughout this Thesis. Finally, the outline of the Thesis is given in Sec. 1.9.

1.2 Hydrodynamics of the Dispersing Medium

In colloidal systems, there is a clear length- and time-scale separation between the suspended objects and the molecular liquid, hence, it is beneficial to describe the latter by a continuum

model [20]. The fluid is characterized by density, stress and velocity fields at position $\mathbf{r}$ and time t, indicated by $\rho(\mathbf{r},t)$, $\sigma(\mathbf{r},t)$, and $\mathbf{u}(\mathbf{r},t)$ respectively. Conservation of fluid mass is captured by the continuity equation

$$\partial_t \rho + \boldsymbol{\nabla} \cdot (\rho \mathbf{u}) = 0. \tag{1.1}$$

We will focus on *incompressible* fluids, where the density does not change locally and can be assumed to be a constant over space and time. We will denote it hereafter by ρ_f. In this case, Eq. (1.1) becomes

$$\boldsymbol{\nabla} \cdot \mathbf{u} = 0. \tag{1.2}$$

An additional equation that describes conservation of momentum is given by applying Newton's second law to any fluid volume, which, with the aid of Eq. (1.2), reads

$$\rho_f \partial_t \mathbf{u} + \rho_f (\mathbf{u} \cdot \boldsymbol{\nabla}) \mathbf{u} = \boldsymbol{\nabla} \cdot \sigma + \mathbf{f}_{\text{ext}}, \tag{1.3}$$

where $\mathbf{f}_{\text{ext}}$ refers to external force density. In simple viscous flows, in addition to an isotropic pressure term, the stress tensor includes terms that are proportional to the first derivatives of the velocity field (shear rate):

$$\sigma_{ij} = -p\delta_{ij} + \eta(\nabla_i u_j + \nabla_j u_i) + \zeta(\boldsymbol{\nabla} \cdot \mathbf{u})\delta_{ij}, \tag{1.4}$$

where p is the pressure field of the fluid, η is the *coefficient of shear viscosity*, ζ is the *coefficient of bulk viscosity*, and δ_{ij} is Kronecker delta. Substituting this stress definition into Eq. (1.3) and taking into account the incompressibility of the flow (Eq. (1.2)), we get

$$\rho_f \partial_t \mathbf{u} + \rho_f (\mathbf{u} \cdot \boldsymbol{\nabla}) \mathbf{u} = -\boldsymbol{\nabla} p + \eta \nabla^2 \mathbf{u} + \mathbf{f}_{\text{ext}}. \tag{1.5}$$

This is the *Navier-Stokes equation* describing the hydrodynamics of viscous incompressible fluids. Since the bulk viscosity ζ is irrelevant for incompressible flows, η will be referred hereafter as the viscosity of the fluid. In principle, a complete description of the fluid also includes equations for energy conservation. However, we will consider an isothermal liquid, in which the temperature is constant in space and time (i.e., any dissipation is immediately transferred to an external temperature bath). The above hydrodynamic equations determine a variety of complex nonlinear phenomena such as turbulence and lift forces. In this Thesis we will focus on colloidal processes, for which the Navier-Stokes equation can be simplified, as will be discussed next.

1.2.1 Stokes Equation

Consider a flow with a characteristic length L and a characteristic velocity U. By rescaling velocity, length, time, pressure and force density according to $\bar{u} \to u/U$, $\bar{r} \to r/L$, $\bar{t} \to tU/L$,

$\bar{p} \to pL/(\eta U)$, and $\bar{f} \to fL^2/(\eta U)$, respectively, the Navier-Stokes equations are given as

$$\mathrm{Re}\left(\partial_{\bar{t}}\bar{\mathbf{u}} + \bar{\mathbf{u}}\cdot\bar{\boldsymbol{\nabla}}\bar{\mathbf{u}}\right) = -\bar{\boldsymbol{\nabla}}\bar{p} + \bar{\nabla}^2\bar{\mathbf{u}} + \bar{\mathbf{f}}_{\mathrm{ext}}, \tag{1.6}$$

where

$$\mathrm{Re} \equiv \frac{\rho_f U L}{\eta} \tag{1.7}$$

is called the *Reynolds number* of the flow. At high Reynolds number, $\mathrm{Re} \gg 1$, the non-linear term dictates non-dissipative energy and momentum transfer between different layers within the fluid. At this limit, turbulent flow can be generated, and the fluid can be assumed as inviscid except for small length scales at which viscosity is important. At low Reynolds number, $\mathrm{Re} \ll 1$ the inertial-forces are negligible with respect to the viscous ones, the flow varies slowly in time and a turbulent behavior cannot occur. The Reynolds number sometimes provides useful experimental transformation between systems of different scales, namely, systems with the same Reynolds number are expected to exhibit similar phenomena[2]. For instance, the motion of a micron-sized object in water should be similar to the one of a mm-sized object moving with the same velocity in glycerol, since glycerol is $\sim 10^3$ times more viscous than water, but has approximately the same (1.4 times larger) density.

Colloidal systems are typically characterized by $\mathrm{Re} \ll 1$. For example, a μm-sized object in water ($\rho_f \sim 10^3$ kg·m^{-3}, $\eta \sim 10^{-3}$ Pa·s), moving with μm s^{-1} translational velocity or rotating with s^{-1} angular velocity, corresponds to $\mathrm{Re} \sim 10^{-6}$. Therefore, colloidal systems are analyzed at the limit of *zero Reynolds number*, in which the Navier-Stokes equation (Eq. (1.5)) becomes

$$0 = -\boldsymbol{\nabla} p + \eta\nabla^2\mathbf{u} + \mathbf{f}_{\mathrm{ext}}. \tag{1.8}$$

Eq. (1.8) is known as the *Stokes Equation*; it describes inertia-less flows (also termed as "creeping flows" or "Stokes flows"). The properties of the Stokes equation differ significantly from those of the Navier-Stokes equation— it is a linear differential equation; it describes a steady state flow; and it is time-reversible, i.e., invariant under inversion of time, velocities and forces. The consequences of these properties, in the context of driven colloids, will be dealt with in Sec. 1.3.

The inertia-less limit governs the fluid hydrodynamics in colloidal systems. Therefore, in the work to follow, the embedding fluid dynamics will be mandated by the Stokes equation, Eq. (1.8), together with the incompressibility of the flow, stated in Eq. (1.2). In the rest of this section we elaborate on the properties of hydrodynamic interactions and drag forces in inertia-less flows, both of these play an important role in the dynamics of driven colloids.

[2]This is true when there are no additional effects that are not scale-invariant, such as Brownian motion, which is negligible in large scales but not in small ones.

1.2.2 Hydrodynamic Interactions

Flows excited by moving objects induce effective *hydrodynamic interactions* among objects. The basic properties of these interactions in driven systems are clarified by examining the response of the fluid to external point force:

$$\begin{aligned} -\boldsymbol{\nabla} p + \eta \nabla^2 \mathbf{u} + \delta(\mathbf{r} - \mathbf{r}_0)\mathbf{F}_0 = 0, \\ \boldsymbol{\nabla} \cdot \mathbf{u} = 0, \end{aligned} \tag{1.9}$$

where $\mathbf{F}_0$ is a constant vector and $\delta(\mathbf{r} - \mathbf{r}_0)$ is the Dirac Delta function. A point force in the inertia-less regime is called *stokeslet*, as first coined by Hancock [21] in 1953[3]. Linearity implies that the solution to Eq. (1.9) has the form $\mathbf{u}(\mathbf{r}) = \mathbb{G}(\mathbf{r}, \mathbf{r}_0) \cdot \mathbf{F}_0$, where the tensor $\mathbb{G}$ is a Green's function of the Stokes equation that depends on the geometry of the boundaries, the boundary conditions, the fluid viscosity and the dimensionality of the flow. Below we consider the stokeslet flow in two specific 3D geometries— unbounded fluid and a fluid bounded by a plane wall. These two examples, especially the first one, will be the basis for the analysis in the following Chapters.

Unbounded 3D Fluid– the Oseen Tensor

The geometry of an unbounded system has translational invariance, thus, the Green's function depends only on the distance relative to the forcing point, i.e., $\mathbb{G}(\mathbf{r}, \mathbf{r}_0) = \mathbb{G}(\mathbf{r} - \mathbf{r}_0)$, and we can simplify further by taking $\mathbf{r}_0 = \mathbf{0}$. The solution to Eq. (1.9) can be obtained by transforming to Fourier space ($\mathbf{r} \to \mathbf{q}$), where for any function $g(\mathbf{r})$ we have

$$\tilde{g}(\mathbf{q}) = \int g(\mathbf{r}) e^{i\mathbf{q}\cdot\mathbf{r}} d\mathbf{r} \tag{1.10}$$

$$g(\mathbf{r}) = \frac{1}{(2\pi)^3} \int \tilde{g}(\mathbf{q}) e^{-i\mathbf{q}\cdot\mathbf{r}} d\mathbf{q}. \tag{1.11}$$

Fourier transforming Eq. (1.9) yields the algebraical equations

$$\begin{aligned} i q_m \tilde{p} - q^2 \eta \tilde{u}_m + F_{0,m} = 0, \\ -i q_m \tilde{u}_m = 0, \end{aligned} \tag{1.12}$$

whose solution reads

$$\tilde{p} = -\frac{i\mathbf{F}_0 \cdot \mathbf{q}}{q^2}, \tag{1.13}$$

$$\tilde{u}_m = \frac{1}{\eta q^2} \left(\delta_{mj} - \frac{q_m q_j}{q^2} \right) F_{0,j}. \tag{1.14}$$

[3] Historical note: the solution to Eq. (1.9) was first given in 1896 by Lorentz [22], whereas Stokes [23] was the one who found the flow generated by a moving sphere in 1851.

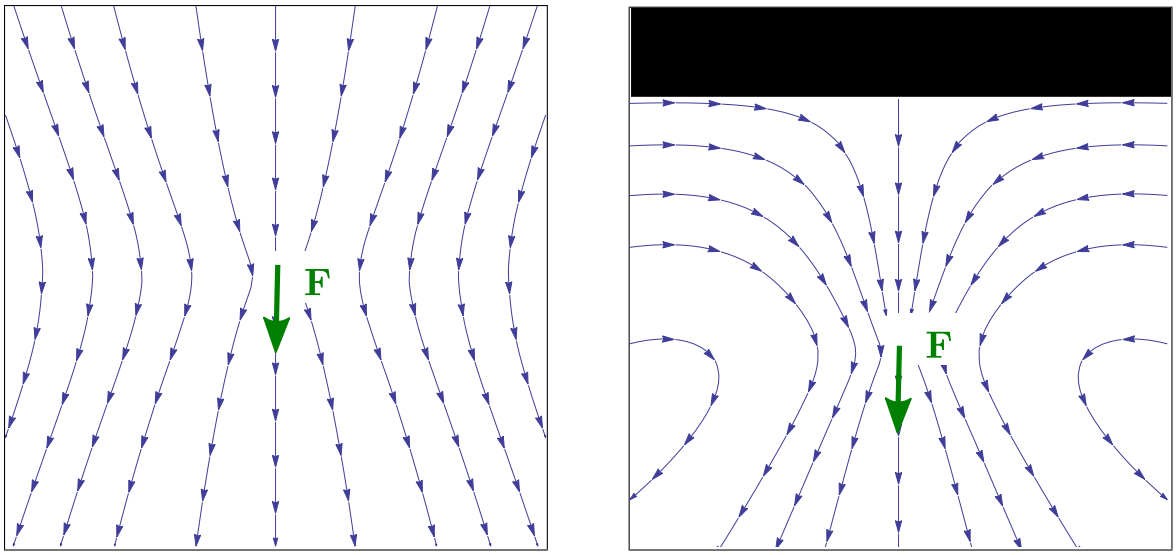

Figure 1.1: The flow lines (thin blue arrows) of the fundamental solutions corresponding to a stokeslet (green thick arrow) in an unbounded and semi-infinite geometries (left panel and right panel respectively). The black rectangle on the right panel indicates the plane wall on which the fluid's velocity vanishes. A 2D projection is presented as the flows have axial symmetry about the stokeslet direction.

By inverting Eq. (1.14) back to real space we have $\mathbf{u} = \mathbb{G}(\mathbf{r}) \cdot \mathbf{F}_0$, where

$$\mathbb{G}_{mj}(\mathbf{r}) = \frac{1}{8\pi\eta r}\left(\delta_{mj} + \frac{r_m r_j}{r^2}\right). \tag{1.15}$$

The tensor $\mathbb{G}$ is called the *Oseen tensor* [24], and it is at the core of hydrodynamic interactions, as it captures how applying a force at one point in the fluid affects the velocity at some other point. Eq. (1.15) states that the flow decays algebraically with the distance as r^{-1} from the forcing point. This slow decay manifests the long-range nature of hydrodynamic interactions.

The fact that $\mathbb{G} \sim 1/(\eta r)$ could have been drawn based on general considerations [25]. Momentum conservation requires that the total momentum flux through any envelope enclosing the source is constant, that is, for a spherical envelope of radius r the local flux is proportional to $1/r^2$. Since the local flux is given by the stress tensor $\sigma \sim \eta\nabla u \sim \eta u/r$, one finds that $u \sim 1/(\eta r)$. The flow resulting from a stokeslet in an unbounded geometry is given on the left panel of Fig. 1.1.

3D Fluid Bounded by a Wall with a No-Slip Boundary Condition

We consider a stokeslet in a semi-infinite medium $z < h$ confined by a wall at $z = h$. The problem is governed by Eq. (1.9) with a no-slip boundary condition at the wall

$$\mathbf{u}(x, y, h) = 0. \tag{1.16}$$

Before writing the solution to the above problem, it is essential to mention the analogy, and difference, between electrostatics and Stokes flows. The electrostatic potential ϕ_e generated by a distribution of charges n_{charge} in a medium of permittivity ε is dictated by the Poisson equation $\nabla^2\phi_e = -n_{charge}/\varepsilon$. The resemblance between the Poisson and Stokes equations (Eq. (1.8)) implies that finding the electrostatic potential for a given charge density is similar to the problem of determining a Stokes flow $\mathbf{u}$ generated by an external force density $\mathbf{f}_{ext}$. However, there is no exact equivalence between the two problems since the latter involves an additional pressure field (this field imposes incompressibility and thus is related to mass conservation, which is not included in electrostatics). This is the essential difference between the two systems. The current semi-infinite hydrodynamic problem highlights the usefulness of the analogy together with illustrating its incompleteness.

The analogy suggests that a convenient approach to find flow fields in bounded geometries is the method of images— placing image charges such that the boundary conditions are satisfied— which is widely used in electrostatics. Now, let us consider the hydrodynamic problem and assume that the stokeslet is placed at the origin $\mathbf{r}_0 = 0$. The analogous electrostatic problem is for a point charge placed near a grounded plane. A naïve solution based on this analogy is to place a mirror image stokeslet: $-\mathbf{F}_0\delta(\mathbf{r} - 2h\hat{\mathbf{z}})$. However, the flow resulting from the stokeslet and its image, which is proportional to $\mathbb{G}(\mathbf{r}) - \mathbb{G}(\mathbf{r} - 2h\hat{\mathbf{z}})$, does not vanish on the plane wall at $\mathbf{r} = (x, y, h)$ with $x, y \neq 0$. The correct solution [24, 26–28] includes additional singular solutions at the mirror position $\mathbf{r}^m = 2h\hat{\mathbf{z}}$, associated with a force-dipole and a fluid-mass-dipole[4]. The flow generated by these multipoles is given by the first derivatives of the Oseen tensor and the source flow ($\propto \mathbf{r}/r^3$), respectively. The total Green's function of a stokeslet near a wall then reads

$$\mathbb{G}_{ij}^{\text{wall}}(\mathbf{r}) = \mathbb{G}_{ij}(\mathbf{r}) - \mathbb{G}_{ij}(\mathbf{r} - \mathbf{r}^m) + 2h\mathrm{Y}_{skj}^{\text{FD}}\partial_s\mathbb{G}_{ik}(\mathbf{r} - \mathbf{r}^m) + 2h^2\mathrm{Y}_{kj}^{\text{MD}}\partial_k u_i^{\text{M}}(\mathbf{r} - \mathbf{r}^m), \tag{1.17}$$

where $\mathbf{u}^{\text{M}} = \mathbf{r}/(8\eta r^3)$ is a mass source flow, and the tensors of coefficients Y^{FD} and Y^{MD} contain numerical values that imply the direction of the force-dipole and source-dipole:

$$\mathrm{Y}_{skj}^{\text{D}} = \begin{cases} \delta_{sj}\delta_{k3} & j = 1,2 \\ -\delta_{sj}\delta_{k3} & j = 3 \end{cases}, \qquad \mathrm{Y}_{kj}^{\text{MD}} = \begin{cases} \delta_{kj} & j = 1,2 \\ -\delta_{kj} & j = 3 \end{cases}. \tag{1.18}$$

An example of the flow generated by a stokeslet pointing in a direction perpendicular to the wall is given in the right panel of Fig. 1.1.

1.2.3 Drag Forces on Moving Objects

A rigid body is defined as an object in which the distance between any two points is constant. The kinematics of a rigid object is represented by a translational velocity $\mathbf{V}$, and an angular

[4] In the hydrodynamic literature there is usually a usage of different terminology concerning singularities; see Refs. [28, 29].

velocity $\boldsymbol{\omega}$. More specifically, we choose an arbitrary reference point rigidly affixed to the object, designated hereafter as *the origin* of the object, and denote its instantaneous translational velocity with $\mathbf{V}$. Then, any point of the rigid object, at a position $\mathbf{r}$ from its origin, moves with translational velocity $\mathbf{V} + \boldsymbol{\omega} \times \mathbf{r}$, where $\boldsymbol{\omega}$ is the instantaneous angular velocity of the object. Note that the angular velocity is independent of the choice of origin, and that the origin does not necessarily lie on the instantaneous axis of rotation of the object.

A rigid object translating and rotating in a medium feels drag forces on its surface that resist its motion. The corresponding hydrodynamic problem is dictated by the Stokes equation together with specified boundary conditions at the object's surface. We will assume *no-slip* boundary condition on surfaces, i.e., the flow matches the object velocity at the surface:

$$\mathbf{u}(\mathbf{r}) = \mathbf{V} + \boldsymbol{\omega} \times \mathbf{r}, \quad \mathbf{r} \in \text{object's surface}. \tag{1.19}$$

The linearity of both the Stokes equation and the boundary conditions implies that the flow $\mathbf{u}(\mathbf{r})$ must be linear in $\mathbf{V}$ and $\boldsymbol{\omega}$. Therefore, the resulting drag on the object, given by integrating the hydrodynamic stress ($\sim p + \eta \nabla u$) on the object's surface, obeys a linear relation as well, which can be written in a matrix form:

$$\begin{pmatrix} \mathbf{F}_{\text{drag}} \\ \boldsymbol{\tau}_{\text{drag}} \end{pmatrix} = -\mathbb{P} \begin{pmatrix} \mathbf{V} \\ \boldsymbol{\omega} \end{pmatrix}, \text{ with } \qquad \mathbb{P} \equiv \begin{pmatrix} \mathbb{K} & \tilde{\mathbb{C}} \\ \mathbb{C} & \mathbb{H} \end{pmatrix}. \tag{1.20}$$

The matrix $\mathbb{P}$ is called the propulsion matrix[5], and it depends on the shape of the object and its orientation. The propulsion matrix is a generalization of Stokes' celebrated formula to an object with arbitrary shape. According to Stokes [23], for a sphere with radius ℓ: $\mathbb{K} = 6\pi\eta\ell\mathbb{I}_{3\times3}$, $\tilde{\mathbb{C}} = \mathbb{C} = 0$ and $\mathbb{H} = 8\pi\eta\ell^3\mathbb{I}_{3\times3}$, where $\mathbb{I}_{3\times3}$ is the identity matrix. For a general shape, the propulsion matrix is less trivial. Generally, a straightforward calculation of $\mathbb{P}$ involves solving the Stokes equation in a complex geometry, given by the shape of the object. The discussion on the properties of the propulsion matrix and the different numerical methods to calculate it is postponed to the next Section, where we consider the inverse matrix of $\mathbb{P}$.

1.3 Being Driven at Zero Reynolds Number

The Stokes equation, Eq. (1.8), possesses the three key features of (*i*) time reversibility, (*ii*) linearity, (*iii*) mediation of long-ranged hydrodynamic interactions. This nature leads to counter-intuitive consequences and distinct phenomena for the motion of colloids. For example, in his seminal work, Purcell [30] showed how the propagation of bacteria through water differs significantly from the swimming of a human. For μm-sized organisms in water, which live in the inertia-less regime, reciprocal motion— changing the organism shape back and forward in a reversible manner— cannot result in a net translation. This fact stems from the time-reversibility

[5] This term was coined by Purcell [30], in the literature it is also known as the resistance matrix.

of the Stokes equation. On the other hand, a human can efficiently swim in water, by applying periodic motions that generate inertial flows. The aforementioned characteristics of the Stokes equation play a crucial role in the context of externally driven rigid objects, as will be discussed in the following sections. In the rest of the section we introduce the main tools and framework in which general problems of driven suspensions are analyzed.

1.3.1 Mobility Matrix

Consider a rigid object driven through a viscous fluid by an external force $\mathbf{F}$ and external torque $\boldsymbol{\tau}$. The object's instantaneous linear and angular velocities follow Newton's and Euler's second laws, respectively,

$$m\dot{\mathbf{V}} = \mathbf{F}_{\text{drag}} + \mathbf{F}, \tag{1.21}$$

$$\mathbb{I}\cdot\dot{\boldsymbol{\omega}} = \boldsymbol{\tau}_{\text{drag}} + \boldsymbol{\tau}, \tag{1.22}$$

where m is the mass of the object and $\mathbb{I}$ is its tensor of inertia. The ratio between the change of inertia and the drag terms goes as $\rho_o/\rho_l \text{Re}$, where ρ_o is the object's mass density. Thus, the limit of zero Reynolds number corresponds to an *inertia-less regime*, where the inertia of both fluid and embedded objects are negligible. Under these conditions, at any given time we have $\mathbf{F}_{\text{drag}} = -\mathbf{F}$ and $\boldsymbol{\tau}_{\text{drag}} = -\boldsymbol{\tau}$. Using Eq. (1.20) we get the linear relation

$$\begin{pmatrix}\mathbf{V}\\ \boldsymbol{\omega}\end{pmatrix} = \mathbb{M}\begin{pmatrix}\mathbf{F}\\ \boldsymbol{\tau}\end{pmatrix}, \text{ with} \qquad \mathbb{M} = \mathbb{P}^{-1} \equiv \begin{pmatrix}\mathbb{A} & \tilde{\mathbb{T}}\\ \mathbb{T} & \mathbb{S}\end{pmatrix}. \tag{1.23}$$

The matrix $\mathbb{M}$ is the *self-mobility* matrix of the object. It is a geometric property that depends on the object's shape and orientation[6]. The mobility matrix is symmetric, i.e., $\mathbb{A} = \mathbb{A}^T, \mathbb{S} = \mathbb{S}^T$, $\tilde{\mathbb{T}} = \mathbb{T}^T$, and positive definite [31–33]. Onsager relations dictate the former property, whereas the latter one is demanded by positive energy dissipation rate,

$$\dot{E}_{\text{dissipation}} = (\mathbf{V},\boldsymbol{\omega})^T\cdot(\mathbf{F},\boldsymbol{\tau}) = \eta^{-1}(\mathbf{F},\boldsymbol{\tau})^T\cdot\mathbb{M}\cdot(\mathbf{F},\boldsymbol{\tau}) > 0.$$

The propulsion matrix, $\mathbb{P}$, being the inverse of $\mathbb{M}$, is symmetric and positive-definite as well. The linear response represented by $\mathbb{M}$ comprises tensors— the diagonal blocks $\mathbb{A}$ and $\mathbb{S}$, relating between two vectors or two pseudo vectors, respectively; and a pseudo tensor— $\mathbb{T}$, relating between a vector and a pseudo vector. Henceforth, for simplicity we will refer to $\mathbb{M}$ or its blocks as "matrices". Following the terminology of Ref. [34] for the 3×3 blocks of the mobility matrix we have: $\mathbb{A}$– the alacrity matrix, $\mathbb{S}$– the screw matrix, and $\mathbb{T}$– the twist matrix. We note that the different blocks scale as η^{-1}, but with different powers of the object's typical linear size ℓ: $\mathbb{A}\sim\eta^{-1}\ell^{-1}$, $\mathbb{T}\sim\eta^{-1}\ell^{-2}$, and $\mathbb{S}\sim\eta^{-1}\ell^{-3}$.

[6] The mobility matrix also depends on the boundary condition on the object surface. As specified above, we assume a no-slip boundary condition.

The mobility matrix depends on the choice of object's origin. Consider two frames, Σ and Σ', which differ only by the point about which the objects' linear velocity and external torque are measured. Let $\mathbf{h}$ be the vector pointing from the origin in Σ to the origin of Σ'. The relation between $\mathbb{M}$ and $\mathbb{M}'$ can be found by requiring that in both frames, the object feels the same net force and torque and thus responds with the same motion [32, 34]. This requirement entails $\mathbf{F} = \mathbf{F}'$, $\boldsymbol{\tau} = \boldsymbol{\tau}' + \mathbf{h} \times \mathbf{F}$, $\mathbf{V} = \mathbf{V}' - \boldsymbol{\omega} \times \mathbf{h}$, and $\boldsymbol{\omega} = \boldsymbol{\omega}'$, which in turn results in the following linear transformation [34]:

$$\mathbb{M} = \begin{pmatrix} \mathbb{I}_{3\times3} & \mathbf{h}^{\times} \\ \mathbf{0} & \mathbb{I}_{3\times3} \end{pmatrix} \mathbb{M}' \begin{pmatrix} \mathbb{I}_{3\times3} & \mathbf{0} \\ -\mathbf{h}^{\times} & \mathbb{I}_{3\times3} \end{pmatrix}, \tag{1.24}$$

where a vector $\mathbf{y}$ with a superscript $^{\times}$ indicates the matrix $(\mathbf{y}^{\times})_{ij} = \epsilon_{ikj} y_k$, and ϵ is the Levi-Civita tensor.

Hereafter we consider the following scenario: We focus on objects subjected only to an external force, with no net torque, e.g., as in sedimentation. This, in turn, allows us to use the following simplification: To resolve the ambiguity of mobility matrices referring to choice of different origins, we will choose the object's origin as the forcing point, *viz*, where the measured torque is zero. For instance, in the case of sedimentation, for an object with a uniform mass distribution the origin is taken at the center of buoyant mass.

The mobility matrix of an arbitrarily shaped object can be determined numerically by solving a hydrodynamic problem in the proper geometry, defined by the object's shape; see Sec. 1.2.3. There are equivalent numerical schemes, known as boundary integral methods, in which 2D boundary integral equations are solved instead of solving the 3D partial differential equations governing the Stokes flow [24, 28, 35]. There are more convenient methods for calculating analytically or numerically the mobility matrix of an object, without solving explicitly the hydrodynamic problem. For example, if the object consists of a discrete set of small spheres, separated by much larger rigid distances, the mobility matrix can be calculated analytically by approximating each sphere as a point-force (stokeslet). Since this type of objects will be considered in the following Chapters, we elaborate on their properties separately in Sec. 1.4.4. In the case of continuous smooth objects, there are three numerical routines known in the literature. The first technique uses extrapolation of the stokeslets approximation by smoothing the singularity of the stokeslets [36]; the second method uses hydrodynamic codes for objects composed of ellipsoids [37]; and the third method uses the known spherical harmonics, or force multipole expansion, of the Stokes flow outside a single sphere [38–40].

Péclet Number

Even in the absence of driving, a colloidal object suspended in a fluid undergoes a seemingly random motion due to its incessant collisions with the fluid molecules. This is the well known

Brownian motion, named after the botanist Robert Brown who observed this transport phenomenon in 1827. Einstein [41] showed that the Brownian motion of an object is equivalent to a diffusion process. His famous result connects the diffusion coefficients $\mathbb{D}$ to the mobility of the object via fluctuation-dissipation relations— $\mathbb{D} = k_B T \mathbb{M}$, where T is the fluid temperature. When a Brownian object is subjected to an external drive, its transport and orientation are dictated by a stochastic feature of diffusion and a deterministic response to the external drive. The relative strength between these two features is given by the corresponding Péclet numbers for translation and rotation, respectively:

$$\mathrm{Pe}_{\mathrm{T}} = \frac{\ell |\mathbf{V}|}{D_{\mathrm{T}}} \quad , \quad \mathrm{Pe}_{\mathrm{R}} = \frac{|\boldsymbol{\omega}|}{D_{\mathrm{R}}}, \tag{1.25}$$

where D_{T} are D_{R} are the translational and rotational diffusion coefficients. For $\mathrm{Pe} \gg 1$ the dynamics is essentially deterministic while for $\mathrm{Pe} \ll 1$ the dynamics is stochastic. Throughout this Thesis we will consider the limit of *high Péclet number*, $\mathrm{Pe} \gg 1$, where thermal effects will be neglected. This limit might not be applicable for very small colloidal objects. In the case of sedimentation, the translational Péclet number of an object with typical size ℓ is $\mathrm{Pe}_{\mathrm{T}} \sim \ell F / k_B T \sim \ell^4 \Delta\rho g / k_B T$, where $\Delta\rho$ is the density difference between the object and the fluid, and g is the acceleration of gravity. Therefore, for example, a polystyrene sphere with radius of 1μm suspended in water at room temperature ($\Delta\rho \approx 40$ kg·m^{-3}, $k_B T \approx 4 \cdot 10^{-21}$J) has a Péclet number of order 1, whereas a sphere with radius of 10μm at the same conditions has a Péclet number of order 10^4.

In the next Sections we consider the motion of driven, non-Brownian objects at zero Reynolds number.

1.4 Single Object Dynamics

The dynamics of an isolated rigid object subjected to an external force is fully captured by the mobility matrix in Eq. (1.23)— the instantaneous linear and angular velocities are given as

$$\mathbf{V} = \mathbb{A} \cdot \mathbf{F}, \tag{1.26}$$

$$\boldsymbol{\omega} = \mathbb{T} \cdot \mathbf{F}. \tag{1.27}$$

Below, we provide a general review on the motion of an isolated object— first we consider the case of regular objects whose $\mathbb{T}$ matrix vanishes, and then we discuss in detail the case of irregular objects with $\mathbb{T} \neq 0$.

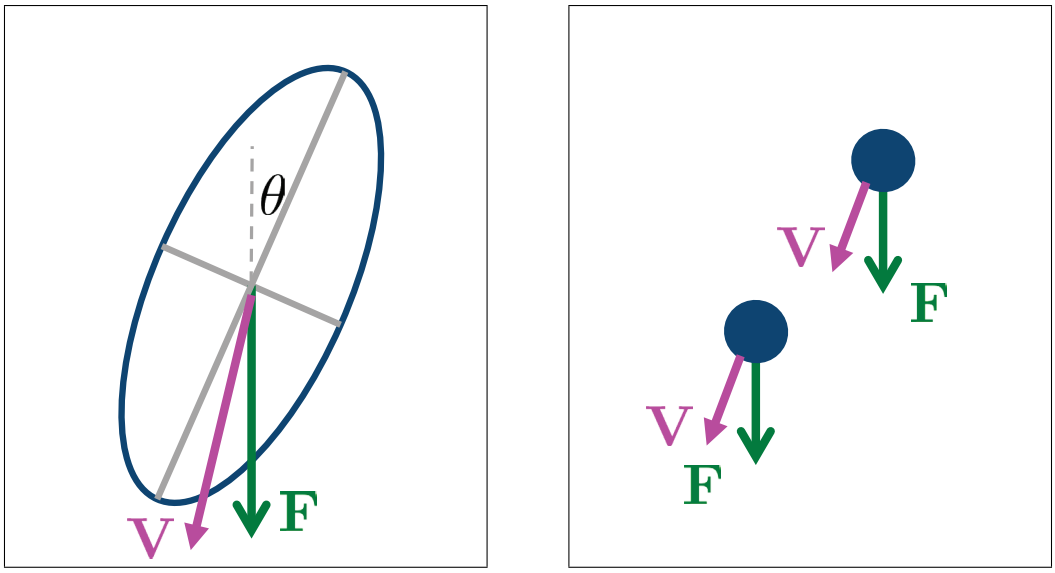

Figure 1.2: Left panel: Sedimentation of an isolated prolate spheroid. The spheroid maintains its orientation (ω=0) while it is gliding horizontally according to its tilted orientation. Right panel: sedimentation of two identical, isolated spheres. The hydrodynamic interaction between the spheres results in (a) translation perpendicular to the force direction, which is absent in the case of a single sphere, and (b) a change in the magnitude of the settling speed; Yet, the interaction does not bring about relative translation between the spheres.

1.4.1 Regular Objects

"Regular objects" will refer to objects with $\mathbb{T} = 0$. These objects do not rotate under external body force, regardless of their orientation in space. Spheres and spheroids are examples of such objects. The fact that an isolated sedimenting spheroid maintains its orientation can be understood by symmetry considerations. Consider a spheroid as depicted on the left panel of Fig. 1.2— it is subjected to a constant force at its center, and its major axis is oriented by an angle θ from the forcing direction. Assume by negation that the spheroid responds to the force with a rotation that decreases θ. On the one hand, time-reversibility of the inertia-less regime requires that inverting the force gives an opposite rotation, *viz*, increasing θ; On the other hand, reversing the force keeps the same physical picture, for which we assume that θ decreases. Hence, we reach a contradiction, and conclude that a spheroid cannot respond with a rotation to a force.

The translational response of regular objects can have a component perpendicular to the force direction. For example, a sedimenting prolate spheroid, whose major axis is tilted with respect to gravity, will glide sideways; see left panel of Fig. 1.2. This gliding effect stems from the fact the the drag along the spheroid's major axis is smaller than the drag along the semi-axis.

1.4.2 Classification of Irregular Objects

"Irregular objects"— defined as objects with non-vanishing $\mathbb{T}$ matrix— exhibit complex dynamics, as their motion possesses coupling between translation and rotation. The tensor $\mathbb{A}$ and the pseudo-tensor $\mathbb{T}$ rotate as the object rotates with angular velocity $\boldsymbol{\omega}$. Thus, Eq. (1.27) is a nonlinear equation for the object's orientation. The evolution of $\mathbb{A}$ and $\mathbb{T}$ in time can be resolved as follows [34, 42, 43]: the relation between the twist matrix at some time t and after a small time interval dt, is given by a small rotation,

$$\mathbb{T}(t+dt) = \left(\mathbb{I}_{3\times 3} - dt\boldsymbol{\omega}^{\times}\right)\cdot\mathbb{T}(t)\cdot\left(\mathbb{I}_{3\times 3} + dt\boldsymbol{\omega}^{\times}\right).$$

Keeping terms up to order dt reads

$$\mathbb{T}(t+dt) = \mathbb{T}(t) + dt\left(\mathbb{T}\cdot\boldsymbol{\omega}^{\times} - \boldsymbol{\omega}^{\times}\cdot\mathbb{T}\right).$$

Next, substituting $\boldsymbol{\omega}$ from Eq. (1.27) and taking the limit $dt \to 0$ we find

$$\dot{\mathbb{T}} = [\mathbb{T}, (\mathbb{T}\cdot\mathbf{F})^{\times}], \tag{1.28}$$

where the square brackets denote commutation. The nonlinear differential equation for $\mathbb{T}$ in Eq. (1.28) dictates the object's orientational dynamics. The translational motion varies in time as the object changes its orientation. This is captured by the dynamics of $\mathbb{A}$ according to

$$\dot{\mathbb{A}} = [\mathbb{A}, (\mathbb{T}\cdot\mathbf{F})^{\times}]. \tag{1.29}$$

The derivation of Eq. (1.29) is similar to the one which gives Eq. (1.28). Once the evolution of $\mathbb{A}$ and $\mathbb{T}$ is found, the motion of the object can be integrated from Eq. (1.26) and Eq. (1.27).

In many cases, it is convenient to work in the body frame ($\Sigma_{(b)}$) where $\mathbb{T}_{(b)}$ is *constant*. In this frame, the external force rotates with angular velocity $-\boldsymbol{\omega}$, and therefore its evolution is dictated by the nonlinear differential equation

$$\dot{\mathbf{F}}_{(b)} = -(\mathbb{T}_{(b)}\cdot\mathbf{F}_{(b)})\times\mathbf{F}_{(b)}, \tag{1.30}$$

(Here we consider a force which is constant in the laboratory frame. If the external force is time varying in Σ, then the term $\partial_t\mathbf{F}_{(b)}$ should be added to the right-hand-side of Eq. (1.30)). Since $|\mathbf{F}|$ is constant, Eq. (1.30) describes a dynamical system on a 2D surface of a sphere. Such a system can evolve into three different orbits— fixed point, closed orbit, or limit cycle [44]. We divide the objects whose $\mathbb{T}$ is nonzero into three classes (not directly related to the latter three kinds of orbits) [34, 42, 43, 45]:

1. "Symmetric-$\mathbb{T}$" objects— correspond to symmetric $\mathbb{T}_{(b)}$. The twist matrix has 3 real eigenvalues, and thus, the dynamical system for $\mathbf{F}_{(b)}$ has six fixed points, given by the

direction of the corresponding eigenvectors— four of them are neutrally stable and the two others are unstable. In addition, all the trajectories of $\mathbf{F}_{(b)}$ are closed orbits. This fact can be deduced from an analogy to free rotation from classical mechanics. There, a rigid object, with a symmetric tensor of inertia $\mathbb{I}$, rotates with a constant angular momentum $\mathbb{L}$. The motion is mandated by Euler's equation $\boldsymbol{\omega} = \mathbb{I}^{-1} \cdot \mathbb{L}$, in analogy to Eq. (1.27). The vector $\mathbb{L}$ is constrained to lie on a sphere of radius $|\mathbb{L}|$. In addition, the symmetry of $\mathbb{I}$ refers to a conservation of the energy $\mathbb{E} = \frac{1}{2}\mathbb{L}^T \cdot \mathbb{I} \cdot \mathbb{L}$, which in turn, constrains $\mathbb{L}$ to another closed surface. The two constraining surfaces enforce the trajectory of $\mathbb{L}_{(b)}$ to lie in a closed orbit. Therefore, the orientational motion of a driven symmetric-$\mathbb{T}$ colloid in the laboratory frame is equivalent to the motion achieved by flipping a rigid body to the air.

2. "Self-aligning" objects— correspond to objects with a twist matrix which is sufficiently asymmetric such that it has only one real eigenvalue, λ_3. This Thesis will mostly focus on this type of objects. These objects were shown to occupy a significant portion of the space of irregular objects [34]. The dynamical system in the body frame $\Sigma_{(b)}$ has one globally stable fixed point and an unstable one. The matching ultimate dynamics in the laboratory frame involves an alignment of the eigenvector corresponding to λ_3 with the force direction, and rotation about this direction with an angular velocity $\lambda_3|\mathbf{F}|$. Ref. [34] studied thoroughly the properties of self-aligning objects. The next Subsection is devoted to the dynamics of self-aligning objects and its applications.

3. "Non-aligning" objects— correspond to $\mathbb{T}_{(b)}$ which has three real eigenvalues but is not symmetric. The dynamics in this case is richer than in the self-aligning class. Basically, there are two stable fixed points and limit cycles may also appear.

1.4.3 Dynamics of a Self-Aligning Object

The dynamics of self-aligning objects contains two distinguished features: (1) alignment of a specific eigen-direction affixed to the object with the force, and (2) axial rotation about this ultimate aligned state. These two features are captured by the twist matrix $\mathbb{T}$, and thus, are geometrical properties of the object. In what follows, we analyze in more detail the aligning dynamics and review the interesting consequences arising from the ultimate rotation.

Let us consider the motion of $\mathbf{F}_{(b)}$ according to Eq. (1.30). This autonomous equation has two fixed points, in opposite directions, given by the eigenvectors $\pm\mathbf{v}_{3,(b)}$ that corresponds to λ_3. The stability of the fixed points can be determined by the time-derivative of the quantity $\mathbf{F}_{(b)} \cdot \mathbf{v}_{3,(b)}$— its sign tells whether $\mathbf{F}_{(b)}$ moves toward or away from the fixed point. One can show [34, 43] that $\partial_t \mathbf{F}_{(b)} \cdot \mathbf{v}_{3,(b)}$ keeps its sign for any $\mathbf{F}_{(b)} \neq \pm\mathbf{v}_{3,(b)}$; hence, one direction, $\mathbf{v}_{3,(b)}$ or $-\mathbf{v}_{3,(b)}$, is a globally stable fixed point whereas the other is unstable.

Another useful quantification of the fixed point is given by a linear stability analysis. With-

out loss of generality, assume that $\mathbf{v}_{3,(b)}$ is the stable fixed point. Substituting $\mathbf{F}_{(b)} = \mathbf{v}_{(3)} + \delta\mathbf{F}$ into Eq. (1.30), and keeping terms up to order $O(\delta\mathbf{F})$, we have

$$\dot{\delta\mathbf{F}} = (\mathbf{v}^{\times}_{3,(b)} \cdot \mathbb{T}_{(b)} - \lambda_3 \mathbf{v}^{\times}_{3,(b)}) \cdot \delta\mathbf{F}. \tag{1.31}$$

The stability matrix $(\mathbf{v}^{\times}_{3,(b)} \cdot \mathbb{T}_{(b)} - \lambda_3 \mathbf{v}^{\times}_{3,(b)})$ has a zero eigenvalue that corresponds to $\mathbf{v}_{3,(b)}$, and two nonzero ones. The real values of the latter two, denoted hereafter by α_1 and α_2, are negative, giving the rates at which an aligned state is restored from a slightly misaligned one. This quantity characterizes the alignability strength of self-aligning objects.

The real eigenvalue λ_3 characterizes the ultimate rotation of an externally driven self-aligning object. The choice of a rotation sense under a unidirectional force— given by the sign of λ_3— implies a chiral response. Such richer responses can be exploited to obtain "steerable colloids"— objects whose orientation and transport can be controlled in much more detail. One example is the application of external torque by a rotating uniform magnetic field to achieve efficient transport of chiral magnetic objects [2]. This is based on the dynamics according to $\mathbf{V} = \mathbb{T}^T \cdot \boldsymbol{\tau}$. Another example, which is relevant to this Thesis, is the ability to achieve orientational alignment of asymmetric objects by applying an external force.

Sedimentation of many identical, self-aligning, non-interacting objects, which are initially distributed in different orientations, results in partial orientational alignment. It is partial because each object has its own phase, depending on its own initial orientation. Refs. [46–48] provided two time-dependent forcing protocols to reach full alignment of non-interacting, self-aligning objects— (1) a force randomly alternating in time between two directions, and (2) a force uniformly rotating about an axis. The theory guarantees full alignment only in the limit of an infinitely dilute system, in which the interaction between the objects is neglected. The effect of hydrodynamic interactions on orientational alignment is one of the subjects studied in this Thesis.

1.4.4 Stokeslets Objects

In this Thesis we aim to study general properties of driven asymmetric objects, thus, we do not restrict ourselves to specific object shapes. A useful approach to demonstrate, or to numerically explore, generic trends is through randomly generated objects. Arguably the simplest form of an arbitrarily shaped object is the so-called *stokeslets object* — a discrete set of small spheres, separated by much larger, rigid distances, where each sphere is approximated as a point force. The usefulness of this simple type of objects was illustrated in Ref. [34] which studied general properties of the motion of a single self-aligning object. We now present in detail how the mobility matrix of stokeslets objects can be determined explicitly.

The mobility matrix of stokeslets objects can be derived self-consistently from linear rela-

tions describing the stokeslets' configuration [34, 49]. This method is based on the approach of Kirkwood and Riseman, as described by Ref. [50]. Consider an object consisting of N stokeslets, which moves with linear and angular velocities $\mathbf{V}$ and $\boldsymbol{\omega}$. The configuration and its kinematics are represented by the following sets of N 3-vectors (denoted by underlined letters, see Sec. 1.8): the stokeslets' strengths, $\underline{\mathbf{f}} = (\mathbf{f}_1, \ldots, \mathbf{f}_N)$; their positions measured from the object's origin, $\underline{\mathbf{r}} = (\mathbf{r}_1, \ldots, \mathbf{r}_N)$; and the velocities of the spheres representing the stokeslets, $\underline{\mathbf{v}} = (\mathbf{v}_1, \ldots, \mathbf{v}_N)$. Each sphere is of radius ϱ, where $\varrho < \min(r_1, \ldots, r_N)$. An illustration of a stokeslet object is given in Fig. 1.3 (see also Fig. 2.2). The boundary conditions at the sphere surface enter only through its self-mobility coefficient (i.e., through the use of the Stokes mobility). The velocity of the nth sphere is known from the object's linear and angular velocities, $\mathbf{v}_n = \mathbf{V} + \boldsymbol{\omega} \times \mathbf{r}_n$. In a matrix form we can write

$$\underline{\mathbf{v}} = \mathbb{U} \cdot \begin{pmatrix} \mathbf{V} \\ \boldsymbol{\omega} \end{pmatrix}, \qquad \text{with } \mathbb{U} = \begin{pmatrix} \mathbb{I}_{3\times 3}, -\mathbf{r}_1^{\times} \\ \vdots \\ \mathbb{I}_{3\times 3}, -\mathbf{r}_N^{\times} \end{pmatrix}. \tag{1.32}$$

Next, we derive the linear relation between the stokeslets and the spheres' velocities. Consider the stokeslet at position $\mathbf{r}_n$. The flow at that point is generated by the other stokeslets, $\mathbf{u}(\mathbf{r}^n) = \Sigma_{m\neq n}\mathbb{G}(\mathbf{r}_n - \mathbf{r}_m) \cdot \mathbf{f}_m$. The stokeslet at that point is proportional to the velocity of the sphere relative to the local flow, $\mathbf{f}_n = (6\pi\eta\varrho)^{-1}(\mathbf{v}_n - \mathbf{u}(\mathbf{r}_n))$. This gives a linear relation between the stokeslets and the velocities of the spheres,

$$\underline{\mathbf{v}} = \mathbb{L} \cdot \underline{\mathbf{f}}, \tag{1.33}$$

where the $3N \times 3N$ matrix $\mathbb{L}$ is composed of the following N^2 3×3 blocks:

$$(\mathbb{L}_{nm}) = \begin{cases} \mathbb{G}(\mathbf{r}_n - \mathbf{r}_m) & \text{if } n \neq m \\ (6\pi\eta\varrho)^{-1}\mathbb{I}_{3\times 3} & \text{if } n = m \end{cases}. \tag{1.34}$$

Let us now find the mobility matrix, in Eq. (1.23), which gives the object's linear and angular velocities as a response to the external force and torque acting on it. The latter two must be equal to the sum of the stokeslets and the corresponding total torque, respectively. In a matrix form we can write

$$\begin{pmatrix} \mathbf{F} \\ \boldsymbol{\tau} \end{pmatrix} = \mathbb{U}^T \cdot \underline{\mathbf{f}}, \tag{1.35}$$

where $\mathbb{U}$ is defined in Eq. (1.32). Using the linear relations of Eq. (1.32), Eq. (1.33), and Eq. (1.35) we have

$$\mathbb{U}^T \cdot \mathbb{L}^{-1} \cdot \mathbb{U} \cdot \begin{pmatrix} \mathbf{V} \\ \boldsymbol{\omega} \end{pmatrix} = \begin{pmatrix} \mathbf{F} \\ \boldsymbol{\tau} \end{pmatrix}$$

From this expression we identify the self-mobility matrix as

$$\mathbb{M} = \left[\mathbb{U}^T \cdot \mathbb{L}^{-1} \cdot \mathbb{U}\right]^{-1}. \tag{1.36}$$

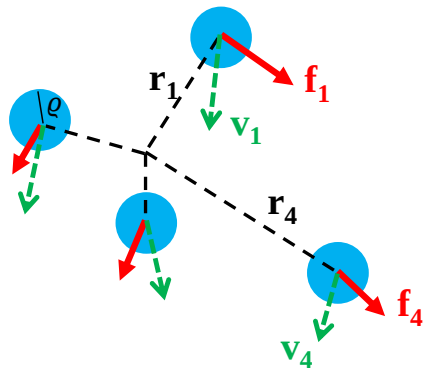

Figure 1.3: Illustration of a stokeslet object. The object comprises small spheres, with radius ϱ, separated by rigid, dragless distances. Each sphere represents a stokeslet (red solid arrows). The linear velocity of the i-th stokeslet is $\mathbf{v}_i$ (green dashed arrows), and its position relative to the object's origin is $\mathbf{r}_i$ (black dashed lines).

The expression in Eq. (1.36) allows to calculate the mobility matrix of stokeslets objects, based on the stokeslets' configuration, the radius of the spheres they represent, and the Oseen tensor alone. The method described here can be generalized to the case of a discrete set of spheres with different radii [34, 49], or to the case of non-sparse objects [49]. In the latter scenario one can use the Rotne-Prager-Yamakawa tensor [51, 52]— a finite-size correction to the Oseen tensor. In addition, stokeslets objects provide a framework for calculating mobilities of compact objects, as mentioned in Sec. 1.3.1.

1.5 A Pair of Objects

The motion of two objects involves long-ranged correlations, excited by the force on each object. The self-mobility of a single object (Eq. (1.23)) can be generalized to the case of two or more objects which are driven through a viscous fluid— the velocities of the suspended objects at a given moment are proportional to the external forces acting at that moment [53]. In Particular, the instantaneous response of two rigid objects, a and b, subject to external forces and torques $\mathbf{F}^a$, $\mathbf{F}^b$ and $\boldsymbol{\tau}^a$, $\boldsymbol{\tau}^b$ is captured by a 12×12 *pair-mobility matrix* [24, 32, 53]:

$$\begin{pmatrix} \mathbf{V}^a \\ \boldsymbol{\omega}^a \\ \mathbf{V}^b \\ \boldsymbol{\omega}^b \end{pmatrix} = \begin{pmatrix} \mathbb{A}^{aa} & (\mathbb{T}^{aa})^T & \mathbb{A}^{ab} & (\mathbb{T}^{ba})^T \\ \mathbb{T}^{aa} & \mathbb{S}^{aa} & \mathbb{T}^{ab} & \mathbb{S}^{ab} \\ (\mathbb{A}^{ab})^T & (\mathbb{T}^{ab})^T & \mathbb{A}^{bb} & (\mathbb{T}^{bb})^T \\ \mathbb{T}^{ba} & (\mathbb{S}^{ab})^T & \mathbb{T}^{bb} & \mathbb{S}^{bb} \end{pmatrix} \begin{pmatrix} \mathbf{F}^a \\ \boldsymbol{\tau}^a \\ \mathbf{F}^b \\ \boldsymbol{\tau}^b \end{pmatrix}. \tag{1.37}$$

As in the single-object case, the pair-mobility in Eq. (1.37) is a symmetric and positive definite matrix. It depends on the whole geometry of the system (i.e., the shapes of the objects, their mutual configuration, the shapes of the surrounding boundaries, and the choice of objects' ori-

gins), as well as the boundary conditions at all the surfaces. The diagonal 6×6 blocks (with the superscripts *aa* or *bb*) correspond to the self-response of the objects, which nevertheless depends on the configuration of both objects. The off-diagonal 6×6 blocks (with the superscripts *ab* or *ba*) describe the pair hydrodynamic interaction.

Previous studies on the mobility of object pairs and the resulting time-dependent trajectories focused on the case of symmetric objects, e.g., spheres [54–56], and spheroids [57–60]. In addition, several numerical techniques were developed to study pair-mobilities of arbitrarily shaped colloids [61, 62]. The hydrodynamic interaction between two identical sedimenting spheres, isolated in an unbounded fluid, affect the magnitude and the direction of the individual sphere's motion [54], see right panel of Fig. 1.2. Nevertheless, the interaction does not bring about any relative translation— the spheres neither reduce nor increase their mutual distance while settling through the fluid. This remarkable result can be related to the time-reversal symmetry of the Stokes equations [63]. Assume by negation that the spheres get further apart while forced along the $-z$ direction. Reversibility implies that if the forces are reversed, i.e., pointing along the z direction, then the spheres will get closer; however, reversing the forces does not change the physical picture, and we reach a contradiction. Thus, we deduce the fact that the spheres maintain their relative separation under the same force.

1.5.1 Hydrodynamic Pseudopotentials

Pair configurations which deviate from the geometry of two spheres in an unbounded fluid may lead to relative translation induced by hydrodynamic interaction. For instance, consider two point-like objects (stokeslets) placed in parallel to a solid wall and forced away from the wall. The flow generated by one stokeslet will advect the other object towards it (and vice versa); see flow lines of a stokeslet near a wall on the right panel of Fig. 1.1. Hence, two objects moving away from the wall develop relative velocity, making them approach one another. In the same manner, settling of two spheres towards the wall leads to separation between the spheres, as was demonstrated in numerical simulations by Tran-Cong and Phan-Thien [62]. Squires and Brenner [64] showed how such flow-mediated effects can explain the optical tweezers experiments in Ref. [65], which measured long-ranged attraction between two like-charged spheres in the presence of a similarly charged wall. Similar apparent interactions were observed in other pair configurations [66], as well as in more complex phenomena, such as collective phonon-like excitations in driven object arrays [67, 68]. Squires [69] referred to such effects as *"hydrodynamic pseudopotentials"* as the apparent interactions merely originate from the flow velocity fields generated by the driven objects rather than from any direct, e.g., electrostatic or van der Waals interaction.

Whereas previous studies of such hydrodynamic couplings treated specific experimental scenarios, this Thesis addresses the general geometrical principles underlying apparent hydrodynamic interactions.

1.6 Three to Many Objects

The vanishing relative velocity between two spheres is violated already at the level of three spheres. Moreover, it has been shown that the settling trajectories of three spheres in a vertical plane within a quiescent, unbounded 3D-fluid are sensitive to the initial configuration of the spheres [70]. This chaotic behavior arises purely from hydrodynamic interactions in the inertia-less regime. Although the Stokes equation governing the flow are linear, the dynamics of a driven suspension is dictated by a nonlinear equation, including, for example, the $1/R$ Oseen interaction between object pairs with mutual separation R; see Eq. (1.15). The effect of the nonlinear, long-ranged interactions is even more pronounced in the case of a many-body system. There, they lead to a stochastic-like behavior of the driven suspension. Examples for related ubiquitous physical processes are sedimentation— the settling of colloidal objects under gravity [71]; bed fluidization [72]— where an upward constant fluid flow is injected through a settling suspension; and externally sheared colloidal materials [73]. An example for clear evidence of stochasticity is the diffusion of a tracer object in the midst of the driven suspension, as was observed in numerical simulations [74] and experiments [75, 76] of sedimenting *non-Brownian* spheres.

1.6.1 Sedimentation

We focus on *steady sedimentation*, i.e, a bulk of settling objects with a constant, spatially uniform number density, and whose statistical state is stationary [77]. The many-body long-ranged interactions, and the non-equilibrium nature of this process, lead to various paradoxes where theory or simulations do not agree with experiments. Some of these paradoxes were eventually resolved, whereas others are still under debate; see recent Reviews in Refs. [63] and [78]. In this section we present the problem of sedimenting spheres, which has been extensively studied in experiments and previous theoretical works.

Consider a suspension consisting of spheres of radius ℓ. Each sphere is subjected to a constant external force— a combination of gravity and buoyancy— $\mathbf{F} = -\frac{4\pi\ell^3}{3}(\rho_o - \rho_f)g\hat{\mathbf{z}}$, where ρ_o is the object's mass density and g is the acceleration of gravity. We indicate the velocity of an isolated sphere by V_s, which according to Stokes' Formula reads $V_\mathrm{s} = F/(6\pi\eta\ell)$. In a sedimenting suspension, the many-body hydrodynamic interactions result in a distribution of objects' velocities, both in parallel and perpendicular to gravity. In the dilute limit, a naïve estimation of the mean settling velocity can be achieved by calculating the velocity of a test object, while all the other objects are assumed to be point-like,

$$\bar{V}_i = V_{\mathrm{s},i} + \int_{L^3} \mathbb{G}_{ij}(\mathbf{r}) F_j c_0 d\mathbf{r}, \tag{1.38}$$

where $\mathbb{G}$ is the Oseen tensor given in Eq. (1.15), c_0 is the mean number density of the suspen-

sion, and L^3 is the volume of the system. Since $\mathbb{G} \sim 1/r$ the integral in Eq. (1.38) diverges with the size of the system, $\bar{V} \sim V_s \varphi (L/\ell)^2$, where $\varphi = c_0 4\pi\ell^3/3$ is the volume fraction of the suspension. However, experiments clearly indicate a finite mean settling velocity, measuring $\bar{V} \approx V_s(1-5\varphi)$ for the dilute limit $\varphi \ll 1$. While two isolated sedimenting spheres settle faster than a single one, many spheres, on average, settle more slowly (this effect is sometimes termed hindered velocity). A quantitative theoretical treatment that explains the experimental results was first given by Batchelor [79]. He noted that in a finite container, having an impenetrable bottom, the mean velocity of the whole suspension must vanish; Thus, he concluded that there must be a steady fluid backflow from the bottom of the container, which on average cancels the flow generated by the settling spheres. The volume flux carried by the sedimenting objects, and therefore the backflow, is proportional to φ. An explicit calculation yields [79, 80]

$$\bar{V} = V_s(1 - 6.55\varphi). \tag{1.39}$$

(An alternative renormalization analysis was given by Hinch [81]. He modified the fluid equations by considering effective density and viscosity.)

Another key issue of steady sedimentation, which is still under debate, is the magnitude of the settling velocity variance. Caflisch and Luke [82] pointed out that the magnitude of velocity fluctuations of individual objects should diverge with the system's size. This prediction has been evident in numerical simulations [74, 83–86] as well; however, experimentally, the indefinite growth of velocity fluctuations with system size has not been observed [71, 75, 76]. Over the years, several theories [63, 87–89] have been developed to resolve this discrepancy between experiments and theory or simulations.

The extent of object's velocity fluctuation in steady sedimentation is directly related to the statistics of objects' number density. This can be shown by the following scaling argument of Ref. [80]. Consider a blob of radius R. The number of objects inside the blob has an average $\sim c_0 R^3$, and, assuming Poissonian fluctuations, a standard deviation $\sim \sqrt{c_0 R^3}$. The velocity fluctuation of the blob can be found by equating the force fluctuation within the blob and the total drag acting on it, $6\pi\eta R\delta V = \sqrt{c_0 R^3} F$. Thus, the velocity variance grows as the linear size of the blob, $\delta V^2 \sim R$. Since there is no limitation on the size of the blob, this scaling argument suggests that the variance of settling velocity should diverge with the system's size L. This is the famous Caflish-Luke result. Conversely, if we demand that the velocity fluctuation be independent of system size, then the variance of the number of objects in the blob should increase as R^2, i.e., as the surface rather than the volume. (See Sec. 1.6.2 below.)

The relation between concentration and velocity fluctuations can be quantified more explicitly [63, 89]. A local fluctuation in number density, $c(\mathbf{r})$, corresponds to a fluctuation in force density, $c(\mathbf{r})F$, which in turn generates a flow

$$u_i(\mathbf{r}) = \int \mathbb{G}_{ij}(\mathbf{r}-\mathbf{r}')c(\mathbf{r}')F_j(\mathbf{r}')d\mathbf{r}' = -F\int \mathbb{G}_{iz}(\mathbf{r}-\mathbf{r}')c(\mathbf{r}')d\mathbf{r}'. \tag{1.40}$$

The resulting velocity point-correlation reads

$$\langle u_i^2(0)\rangle = F^2 \int \mathbb{G}_{iz}(\mathbf{r}')\mathbb{G}_{iz}(\mathbf{r}''+\mathbf{r}')\langle c(\mathbf{r}')c(\mathbf{r}''+\mathbf{r}')\rangle d\mathbf{r}'d\mathbf{r}'' \sim \int \frac{1}{r^2}\langle c(0)c(\mathbf{r})\rangle d\mathbf{r}, \tag{1.41}$$

or in Fourier space

$$\langle u_i^2(0)\rangle = \frac{c_0 F^2}{(2\pi)^3}\int |\tilde{\mathbb{G}}_{iz}(\mathbf{q})|^2 S(\mathbf{q})d\mathbf{q} \sim \int \frac{1}{q^4}S(\mathbf{q})d\mathbf{q}, \tag{1.42}$$

where

$$S(\mathbf{q}) = c_0^{-1}\int \langle c(0)c(\mathbf{r})\rangle e^{i\mathbf{q}\cdot\mathbf{r}}d\mathbf{r} \tag{1.43}$$

is the *static structure factor* of the suspension. If there are no long-range correlations in concentration fluctuations, i.e., $S(\mathbf{q}) \sim$ Constant, then the integral in Eq. (1.42) diverges linearly with the size of the system, in accordance with the scaling result above. Therefore, in the inertia-less regime, finite velocity fluctuations must be accompanied with a mechanism which smooths inhomogeneities and results in density correlations characterized by $S(\mathbf{q}\to 0) = q^\alpha$ with $\alpha > 1$. Indeed, the latter property was observed in experiments [90] and numerical simulations [91] of settling spheres; see also Sec. 1.6.2.

The experiments in Refs. [71] and [92] observed large-scale velocity correlations in the form of swirls, having a finite range of $\xi \approx 20\ell\varphi^{-1/3}$. They measured for $0.01\% < \varphi < 5\%$ a finite velocity variance $\langle u^2\rangle \sim \xi$ whenever the size of the system (container) was larger than the typical length ξ. Following these observations of hydrodynamic screening, several screening mechanisms have been suggested, where a characteristic length emerges from correlations between concentration fluctuations [87], e.g., as a result of stratification [93, 94]; inertial effects [89]; side-wall effects [89]; and noise-induced concentration fluctuations [63, 88].

In this section we have focused on sedimentation of spherical objects, as this phenomenon demonstrates well the underling physics and the relevant questions referring to the dynamical process of sedimentation. We note that sedimentation of non-spherical suspensions, such as spheroids [95, 96], rod-like objects [97–103], and permeable spheres [104], were studied as well. Moreover, it is crucial to mention that these systems show qualitatively different behavior from the spherical case. For instance, dilute suspensions of rods exhibit clumping instability, alignment in the direction of gravity, and occasional flipping [99].

In the next Subsection we present a standard model for analyzing correlations in sedimentation of spheres. As was indicated above, this steady, dynamical process involves suppression of long-wavelength concentration correlations. Sec. 1.6.2 presents this property— known as *hyperuniformity*— in the more general context studied recently.

Fluctuating Hydrodynamics of Steady Sedimentation

Levine, Ramaswamy, Frey, and Bruinsma (LRFB) [88] studied a stochastic continuum model (fluctuating hydrodynamics) of steady sedimentation. They considered a coarse-grained model, ignoring microscopic details, that accounts for large length and time scales of the system. In such a description only the most slowly-varying fields are considered. For steady sedimentation, these are two conserved variables [105]— concentration of suspended objects and momentum density of the suspension. The aforementioned chaotic behavior of many-body dynamics in Stokes flow enters into the description of the long wavelength degrees of freedom as two stochastic terms— random fluxes of objects, which is a direct effect of the eliminated fast degrees of freedom, and an indirect, diffusive flux. The latter is characterized by a phenomenological matrix of diffusion coefficients $\mathbb{D}$, measurable in experiments [75]. The fluctuating object fluxes $\mathbf{f}(\mathbf{r},t)$, are assumed to follow a Gaussian white noise with variance $\langle \mathbf{f}^T(\mathbf{r},t)\mathbf{f}(\mathbf{r}',t')\rangle = 2c_0\mathbb{N}\delta(\mathbf{r}-\mathbf{r}')\delta(t-t')$ [63, 88], where the phenomenological parameters $\mathbb{N}$ can be determined from numerical simulations [91]. The two non-Brownian stochastic responses emerge from the complex many-body interactions excited by the external drive F at each object, therefore: (*i*) They are not bound to obey a fluctuation-dissipation relation, i.e., $\mathbb{D}$ is not necessarily equal to $\mathbb{N}$. (*ii*) Based on dimensional considerations, both phenomenological parameters, $\mathbb{D}$ and $\mathbb{N}$, should scale as $\ell V_s \sim F/\eta$. (*iii*) Following the axial symmetry of the system, $\mathbb{D}$ and $\mathbb{N}$ must be axisymmetric tensors, e.g., $D_{ij} = D_\perp\delta_{ij} + (D_z - D_\perp)\,\delta_{iz}\delta_{jz}$, where $\perp$ refers to the direction perpendicular to gravity.

Following the above principles, the objects' concentration and the velocity fields are coupled via a stochastic advection–diffusion equation

$$\partial_t c(\mathbf{r},t) + \nabla\cdot\left[\left(c_0 + c(\mathbf{r},t)\right)\mathbf{V} - \mathbb{D}\cdot\nabla c(\mathbf{r},t) - \mathbf{f}(\mathbf{r},t)\right] = 0, \tag{1.44}$$

where $c(\mathbf{r},t)$ is the fluctuation in concentration about the mean, and $\mathbf{V}(\mathbf{r},t)$ is the objects' velocity fluctuation field about the mean settling velocity $\bar{V}$.

While the applicability of fluctuating hydrodynamics for describing steady sedimentation has been criticized by some authors, e.g., in Ref. [78], it has been successfully applied to explain several notable properties of steady sedimentation, as described below.

First, the original work by LRFB [88] yields the characteristic length ξ (up to prefactor) that was measured in early experiments [71, 92]. In their model, the objects are point-like, and thus, are merely advected with the fluid velocity, $\mathbf{V} = \mathbf{u}$, where $\mathbf{u}$ is given in Eq. (1.40). Consequently, the objects' flow is divergenceless ($\partial_i V_i = 0$) and proportional to c through the long-ranged interaction ($\mathbb{G}(r) \sim 1/r$). This results in a nonlinear ($\sim c^2$) advective term in the stochastic equation for $c(\mathbf{r},t)$, Eq. (1.44). Substituting $\mathbf{V}$ from Eq. (1.40) into Eq. (1.44), and

Fourier transforming, gives

$$\partial_t \tilde{c}(\mathbf{q},t) + \mathbf{q}\cdot\mathbb{D}\cdot\mathbf{q} + i\int q_j \tilde{\mathbb{G}}_{jz}(\mathbf{k})\tilde{c}(\mathbf{k},t)\tilde{c}(\mathbf{q}-\mathbf{k},t) + i\mathbf{q}\cdot\tilde{\mathbf{f}} = 0. \tag{1.45}$$

LRFB utilized a self-consistent scheme, based on one loop expansion in mode-coupling theory [106, 107], and found that the nonlinear advection renormalizes the diffusive relaxation rate $\sim Dq^2$, adding a non-diffusive one $\sim \gamma_0(q_\perp/q)^2$. The constant γ_0 depends on the the mean concentration c_0, the Péclet number of the suspension $\mathrm{Pe} \equiv F/(\eta D_z)$, and the ratios between the phenomenological parameters $\mathbb{D}$ and $\mathbb{N}$. The resulting structure factor, Eq. (1.43), reads

$$S(\mathbf{q}) = \frac{N_z q_z^2 + N_\perp q_\perp^2}{D_z q_z^2 + D_\perp q_\perp^2 + \gamma_0(q_\perp/q)^2}. \tag{1.46}$$

The non-diffusive relaxation rate $\gamma_0(q_\perp/q)^2$ causes $S(\mathbf{q})$ to decay to zero as q^2, except for the line $\mathbf{q} = q\hat{\mathbf{z}}$ for which $S(q_z \to 0) = N_z/D_z$. The nonlinear mechanism by LRFB produces screening— that is, regulates velocity variance according to Eq. (1.42)— when the inhomogeneity is sufficiently anisotropic (as γ_0 is nonzero for certain ranges of $D_\perp/D_z$ and $N_\perp/N_z$; see Ref. [88]).

There are other non-equilibrium processes that can be described by fluctuating hydrodynamic models. In another example that explores sedimentation of spheres, it was shown that Eq. (1.44) captures the essential details of more recent experiments, once a vertical concentration gradient (stratification) is included in the statistical properties of sedimentation [94].

1.6.2 Hyperuniformity

"Hyperuniformity" [108] refers to a system of point pattern that does not possess infinite-wavelength fluctuations[7]. While a perfect crystal falls into this definition, recently, many studies indicated the hyperuniform structure of various disordered systems and highlighted the importance of such characterization [108, 110–112]. The structure of these systems lies between that of a crystal, which is ordered and has long-ranged density correlations, and that of a liquid— a disordered state, with no density correlations at large-scales. Below, following previous studies, we provide a mathematical definition of hyperuniformity and mention the interesting basic properties of hyperuniform systems, which are relevant to this Thesis.

Consider N points distributed in d-dimensional space. The point pattern's statistics can be characterized as follows: Let us mark by $N(R)$ the number of points in a d-dimensional sphere of radius R, whose center is positioned at some arbitrary point. The number variance of points within the spherical window is

$$\sigma_N^2 \equiv \left\langle N^2(R)\right\rangle - \left\langle N(R)\right\rangle^2, \tag{1.47}$$

[7] Such point patterns are also known as "superhomogeneous" [109].

where the angular brackets denote ensemble average over different realizations of the point distribution. In the case of a Poisson distribution, for increasing window size, the number variance scales as $\sigma_N^2(R) = \langle N(R) \rangle \sim R^d$, *viz*, grows as the sphere's volume. Systems in which the number variance grows more slowly than R^d are termed hyperuniform[8]. A crystal is thus hyperuniform since it has $\sigma_N^2(R) \sim R^{d-1}$ [108].

The suppression of long wavelength fluctuations in hyperuniform systems can be captured by the static structure factor defined in Eq. (1.43). One can show [108, 112] that for such systems $S(\mathbf{q}) \to 0$ as $q \to 0$. This important signature of hyperuniformity is relevant to scattering experiments.

Recent studies showed how hyperuniform structures are useful for designing materials with photonic gaps [113, 114]; play a role in self-organization processes [110, 111, 115]; underlie non-equilibrium transitions from "active" to static absorbing states (including universality with some resemblance to equilibrium phase transitions) [112]; and govern the structure of some jammed systems, such as maximally random jammed object packings [116]. In this Thesis we report a new type of dynamic hyperuniformity in the sedimentation of irregular objects (Chapter 4).

1.7 Orientational Dynamics of a Rigid Object

The mobilities of a single, or many, asymmetric objects depend on the orientations of the objects. Therefore, the treatment of a suspension of asymmetric objects must include an efficient representation of 3D object orientations. Below we provide such a convenient representation, which will be used in the Thesis (Chapter 2 and Chapter 3).

1.7.1 Quaternions

Studying the dynamics of arbitrarily shaped objects involves the complexity of rotations in 3D space. The orientation of a rigid object in the laboratory frame is defined by a 3D rotation of axes affixed to the object (the body frame)— there is a 3×3 rotation matrix $\mathbb{R}$ such that a vector $\mathbf{y}^{(b)}$ in the body frame is oriented along $\mathbf{y}_{(l)} = \mathbb{R} \cdot \mathbf{y}_{(b)}$ in the laboratory frame. The choice of the axes affixed to the object with respect to the laboratory frame is arbitrary. One way to represent a rotation in three dimensions is by an axis of rotation, $\hat{\mathbf{n}}$, and a rotation angle, θ. This representation consists of three independent variables since $|\hat{\mathbf{n}}| = 1$. The corresponding

[8] There are several subtleties concerning the windows' shape and the choice of its center. We ignore these issues for simplicity and clearer representation of the subject.

rotation matrix is given by the Rodrigues' rotation formula

$$\mathbb{R}_{ij}(\hat{\mathbf{n}},\theta) = (1-\cos\theta)\hat{n}_i\hat{n}_j + \cos\theta\delta_{ij} + \sin\theta\epsilon_{ikj}\hat{n}_k. \tag{1.48}$$

In this thesis we will use a more convenient representation of 3D rotations, which is given by four parameters $(\Gamma, \mathbf{\Omega})$ defined as

$$(\Gamma, \mathbf{\Omega}) \equiv \left(\cos\left(\frac{\theta}{2}\right), \hat{\mathbf{n}}\sin\left(\frac{\theta}{2}\right)\right). \tag{1.49}$$

These are the Euler-Rodrigues parameters[9] [117, 118] (also known as Euler parameters or unit quaternion of rotation). The 4-vector $\hat{\mathbf{Q}} = (\Gamma, \mathbf{\Omega})$ satisfies $|\hat{\mathbf{Q}}| = \Gamma^2 + \Omega^2 = 1$. In terms of computational simplicity, efficiency, and stability, this representation surpasses the alternative ones (e.g., Euler angles, or the axis-angle representation described above); Therefore it is ubiquitous in the fields of computer graphics and computer vision [119], as well as in numerical studies of physical phenomena, e.g., calculations of aircraft orbits [120], molecular dynamics simulations [121–123], and studies of colloidal motions [124, 125]. In addition, it can facilitate analytical description, as is evident in the elegant work by Favro [126] on the Brownian motion of arbitrarily shaped objects. Below we describe the properties of the Euler-Rodrigues representation.

1. The parameters $(\Gamma, \mathbf{\Omega})$ and $(-\Gamma, -\mathbf{\Omega})$ correspond to the same rotation. This comes from the fact that rotating with angle θ about $\hat{\mathbf{n}}$ is equivalent to rotating with angle $2\pi - \theta$ about $-\hat{\mathbf{n}}$.

2. The rotation matrix as a function of $(\Gamma, \mathbf{\Omega})$ is given by

$$\mathbb{R}(\Gamma, \mathbf{\Omega}) = \mathbb{I}_{3\times3} + 2\Gamma\mathbf{\Omega}^{\times} + 2(\mathbf{\Omega}^{\times})^2, \tag{1.50}$$

   where $\mathbb{I}_{3\times3}$ is the identity matrix, and as defined above $\mathbf{\Omega}^{\times}$ indicates the matrix $(\mathbf{\Omega}^{\times})_{ij} = \epsilon_{ikj}\Omega_k$, with ϵ being the Levi-Civita tensor.

3. Composition of two rotations: rotating by $(\Gamma_0, \mathbf{\Omega}_0) = (\cos(\theta_0/2), \hat{\mathbf{n}}_0\sin(\theta_0/2))$ and then by $(\Gamma', \mathbf{\Omega}') = (\cos(\theta'/2), \hat{\mathbf{n}}'\sin(\theta'/2))$, where $\hat{\mathbf{n}}'$ is measured in the body frame, results in the parameters

$$(\Gamma'_0, \mathbf{\Omega}'_0) = (\Gamma'\Gamma_0 - \mathbf{\Omega}'\cdot\mathbf{\Omega}_0, \Gamma'\mathbf{\Omega}_0 + \Gamma_0\mathbf{\Omega}' - \mathbf{\Omega}'\times\mathbf{\Omega}_0). \tag{1.51}$$

4. Connection between the object angular velocity and the time derivative of $(\Gamma, \mathbf{\Omega})$: Consider an object whose orientation at time t results from the rotation $(\Gamma(t), \mathbf{\Omega}(t))$. A subsequent rotation in an infinitesimal time interval dt can be represented by a small angle

[9] This representation is related to Pauli matrices: Any 3-vector $\mathbf{y}$ can be identified with a 2-dimensional matrix $\mathbb{Y} = \mathbf{y}\cdot\sigma = \sum_{i=1}^{3} y_i\sigma_i$, where σ_i is the i-th Pauli matrix. A rotation in 3D by $(\Gamma, \mathbf{\Omega})$ corresponds to a 2-dimensional rotation matrix $\mathbb{W}(\Gamma, \mathbf{\Omega}) = \Gamma + i\mathbf{\Omega}\cdot\sigma$, meaning $\mathbf{y}' = \mathbb{R}(\Gamma, \mathbf{\Omega})\mathbf{y} \iff \mathbb{Y}' = \mathbb{W}(\Gamma, \mathbf{\Omega})\cdot\mathbb{Y}\cdot\mathbb{W}^T(\Gamma, \mathbf{\Omega})$.

$\omega_{(b)}dt \ll 1$ around some axis $\hat{\mathbf{n}}$, where $\boldsymbol{\omega}_{(b)} = \omega_{(b)}\hat{\mathbf{n}}$ is the instantaneous angular velocity of the object measured in the body frame. The orientation of the object at time $t+dt$ is given by combining, according to Eq. (1.51), the small orientation $(1, \hat{\mathbf{n}}\omega_{(b)}dt/2)$ successively to the given orientation $(\Gamma(t), \boldsymbol{\Omega}(t))$:

$$(\Gamma(t+dt), \boldsymbol{\Omega}(t+dt)) = \left(\Gamma(t) + \frac{\boldsymbol{\omega}(t)dt}{2}\cdot\boldsymbol{\Omega}, \boldsymbol{\Omega}(t) + \Gamma\frac{\boldsymbol{\omega}(t)dt}{2} - \frac{\boldsymbol{\omega}(t)dt}{2}\times\boldsymbol{\Omega}\right).$$

In a matrix form we can write

$$\begin{pmatrix}\dot{\Gamma}\\ \dot{\boldsymbol{\Omega}}\end{pmatrix} = \frac{1}{2}\begin{pmatrix}0 & -\boldsymbol{\omega}_{(b)}^T\\ \boldsymbol{\omega}_{(b)} & -\boldsymbol{\omega}_{(b)}^\times\end{pmatrix}\begin{pmatrix}\Gamma\\ \boldsymbol{\Omega}\end{pmatrix}, \text{or} \quad \begin{pmatrix}\dot{\Gamma}\\ \dot{\boldsymbol{\Omega}}\end{pmatrix} = \frac{1}{2}\begin{pmatrix}0 & -\boldsymbol{\omega}_{(l)}^T\\ \boldsymbol{\omega}_{(l)} & \boldsymbol{\omega}_{(l)}^\times\end{pmatrix}\begin{pmatrix}\Gamma\\ \boldsymbol{\Omega}\end{pmatrix}, \tag{1.52}$$

where $\boldsymbol{\omega}_{(l)} = \mathbb{R}(\Gamma, \boldsymbol{\Omega})\cdot\boldsymbol{\omega}_{(b)}$ is the angular velocity measured in the laboratory frame. Given the angular velocity evolution $\boldsymbol{\omega}_{(l)}$, the object's orientational dynamics can be found by numerical integration[10] according to Eq. (1.52).

5. Changing the laboratory frame from Σ to $\bar{\Sigma}$ by rotation $(\Gamma_0, \boldsymbol{\Omega}_0)$ corresponds to

$$\begin{pmatrix}\bar{\Gamma}\\ \bar{\boldsymbol{\Omega}}\end{pmatrix} = \begin{pmatrix}\Gamma_0 & \boldsymbol{\Omega}_0^T\\ -\boldsymbol{\Omega}_0 & \Gamma_0\mathbb{I}_{3\times3} - \boldsymbol{\Omega}_0^\times\end{pmatrix}\begin{pmatrix}\Gamma\\ \boldsymbol{\Omega}\end{pmatrix}. \tag{1.53}$$

Since all the 4-vector considered here are of norm 1, the above transformation is unitary.

6. The dot product of two orientation 4-vectors is given as usual by

$$(\Gamma^a, \boldsymbol{\Omega}^a)\cdot(\Gamma^b, \boldsymbol{\Omega}^b) = \Gamma^a\Gamma^b + \boldsymbol{\Omega}^a\cdot\boldsymbol{\Omega}^b = \cos\left(\frac{\theta^a}{2}\right)\cos\left(\frac{\theta^b}{2}\right) + (\hat{\mathbf{n}}^a\cdot\hat{\mathbf{n}}^b)\sin\left(\frac{\theta^a}{2}\right)\sin\left(\frac{\theta^b}{2}\right).$$

The unitary transformation in Eq. (1.53) guarantees that the dot-product is conserved under rotations of the laboratory frame.

1.8 Glossary of Main Notations and Symbols

The dynamics of arbitrarily shaped objects is complex and requires an elaborate notation. We use the following notation regarding vectors, tensors, and matrices throughout the Thesis:

1. 3-vectors are denoted by a bold letter, $\mathbf{v}$, and unit 3-vectors by a hat, $\hat{\mathbf{v}}$.
2. A set of 3-vectors are denoted by underscore, $\underline{\mathbf{F}}$.
3. Matrices are marked by a blackboard-bold letter, e.g., $\mathbb{M}$, where the dimension of the matrix is understood from the context.

[10] While using the numerical scheme it is important to preserve the relation $\Gamma^2 + \Omega^2 = 1$ [121].

4. Tensors of rank 3 are denoted by a capital Greek letter, e.g., Φ.
5. Subscripts with parentheses, e.g., $\mathbb{M}_{(2)}$, represent a term in a multipole expansion.
6. $\mathbb{I}_{n\times n}$ is the $n \times n$ identity matrix.
7. The matrix $\mathbf{y}^{\times}$ obtained from the vector $\mathbf{y}$ is defined as $(\mathbf{y}^{\times})_{ij} = \epsilon_{ikj}y_k$, such that, for any vector $\mathbf{x}$, $\mathbf{y}^{\times} \cdot \mathbf{x} = \mathbf{y} \times \mathbf{x}$.

Next, we provide the main symbols and definitions which are used in the current Chapter and in the work to follow:

1. $\mathbf{u}$: fluid velocity.
2. η: the fluid's viscosity.
3. $\mathbb{G}(\mathbf{r})$: The Oseen tensor.
4. ℓ: the typical linear size of an object, e.g., the radius of a sphere, or one of the axes of a spheroid. For objects of irregular shape, the linear length which is relevant to mobility problems (known as the "hydrodynamic radius") is proportional to the object radius of gyration [34].
5. $\mathbf{V}$: the linear velocity of an object.
6. $\boldsymbol{\omega}$: the angular velocity of an object.
7. $\mathbf{F}$: the external force acting on an object.
8. $\boldsymbol{\tau}$: the external torque acting on an object.
9. $\mathbb{M}$: Full mobility matrix.
10. $\mathbb{A}$: Alacrity matrix, which gives the linear velocity of an object as a response to an external force.
11. $\mathbb{T}$: Twist matrix, which gives the angular velocity of an object as a response to an external force.
12. object's origin: the point about which the external torque on an object and its linear velocity are measured.
13. λ_3: the real eigenvalue of the $\mathbb{T}$ matrix of a self-aligning object.
14. t_{align}^{-1}: the slowest rate at which a self-aligning object, once misaligned, returns to its aligned state under constant force. This rate is given by $t_{\text{align}}^{-1} = \alpha F/(\eta\ell^2)$, where α is a dimensionless parameter related to the component of $\mathbb{T}$ via $\max\{\alpha_1\eta\ell^2, \alpha_2\eta\ell^2\}$; see Eq. (1.31) and the text below it.
15. φ: volume fraction of a suspension.
16. $(\Gamma, \boldsymbol{\Omega})$: Euler-Rodrigues 4-parameters which represent the object's orientations.

1.9 Outline of the Thesis

In this Introduction we have presented the crucial role of hydrodynamic interactions in the dynamics of externally driven colloidal dispersions. The theories established in previous studies mostly focused on suspensions of symmetrically shaped objects. On the collective level, the long-ranged interactions may create large-scale structures and strong fluctuations, as in the sedimentation of spherical colloids. At the level of a forced pair of symmetric objects, several works addressed the apparent hydrodynamic interactions (pseudopotentials) which were observed in experiments involving confined geometries. The dynamics of arbitrarily shaped objects has been examined more recently, at the level of a single object. The combination of driving and hydrodynamics generally leads to rotation-translation coupling (i.e., in the case of irregular objects). In turn, such coupling can be exploited to achieve rotational coherence between non-interacting colloids.

The rich behavior of an isolated, irregular object under external drive raises two questions: (1) What is the effect of hydrodynamic interactions on the orientational alignment of self-aligning colloids? (2) More generally, in a system of two or many colloids, do irregular objects exhibit new phenomena which is absent in the case of symmetric colloids?

In this Thesis we address these fundamental questions. We consider the limits of zero Reynolds number and high Péclet number, *viz*, we neglect inertia and thermal fluctuations. We aim to explore general properties of the hydrodynamic interaction which are independent of the nature of specific objects. We thus do not restrict ourselves to specific shape, but rather analyze arbitrarily shaped objects. The following Chapters are organized as follows:

- The feasibility of actually achieving rotational coherence of self-aligning colloids awaits experimental investigations. Until then, we further strengthen the theoretical basis of this phenomenon by studying in Chapter 2 the effect of hydrodynamic interactions on orientational alignment schemes. We study the properties and symmetries governing the hydrodynamic interaction between two identical, arbitrarily shaped objects. We treat analytically the leading (dipolar) terms of the pair-mobility matrix, affecting the instantaneous relative linear and angular velocities of the two objects at large separation. The time-dependent effects of the hydrodynamic interactions are explicitly demonstrated through numerically calculated trajectories of model self-aligning objects composed of four stokeslets. The two key results of Chapter 2 are: (1) The instantaneous hydrodynamic interaction gives rise to relative translation and rotation between the objects. The latter linearly degrades the orientational alignment by an external time-dependent drive. (2) The separation between pairs of self-aligning objects typically increases with time.
- Motivated by these results, in Chapter 3 we continue to explore the hydrodynamic pair-interaction, focusing on its effect on relative translation rather than relative rotation. We expand the theoretical treatment along two separate lines. First, we study the symme-

tries of the instantaneous interaction in relation to the issue of hydrodynamic pseudopotentials. Secondly, we determine the mechanism which results in the typical repulsion between two self-aligning objects presented in Chapter 2. We compare this repulsion with the dynamics of a more symmetric case of uniform spheroids.

- The results of Chapter 2 and Chapter 3 lead us to Chapter 4 in which we study the sedimentation of irregular objects. First, based on the effects studied in the previous Chapters, we provide a qualitative scaling argument for how self-aligning objects can either smooth, or enhance, inhomogeneities in a sedimenting suspension. We then use fluctuating hydrodynamic to study the steady sedimentation of self-aligning objects. We provide quantitative predictions for the behavior of this system, focusing on its hyperuniform structure and screened velocities.
- Finally, in Chapter 5 we propose future theoretical directions motivated by the results and indicate the experimental significance of their implications.

Several appendices at the end of the Thesis provide technical details, which may be useful in future studies.

Chapter 2

Hydrodynamic Interactions between Two Forced Objects of Arbitrary Shape: Effect on Alignment[1]

As discussed in Sec. 1.4.3 above, an irregular, self-aligning object will align itself with an external driving force. Many such non-interacting objects can be brought to full orientational alignment by a time-dependent drive [46–48]. The motivation of the current Chapter is to explore the effect of hydrodynamic interaction (HI) between two irregular objects on their correlated dynamics, in particular, their mutual alignment. However, the results introduced below have a broader impact on understanding the role of HI in the motion of asymmetric driven colloids in general.

The theoretical groundwork for treating the HI between arbitrary objects in Stokes flow was laid by Brenner and O'Neill [53, 128]. The theory was subsequently applied to a pair of objects of various regular shapes [54–60]. There are key differences between regular objects, such as uniform spheroids, and the irregular objects studied here. The symmetries of a uniform spheroid lead to: (a) the absence of a translation-rotation coupling for a single object, and therefore lack of alignability by an external force; (b) the absence of a $1/R^2$ contribution to the relative velocity developed between two such objects at mutual distance R (see below). In this Chapter we focus on simple, general properties of the pair HI between two arbitrarily shaped objects at zero Reynolds number, and the resulting effect on their alignment. The study of translational effects will be presented in the subsequent Chapter 3.

The current Chapter is made of two distinct parts. The first part, Sec. 2.1 together with Sec. 2.2, treats rigorously the instantaneous HI, i.e., the pair-mobility matrix. We use Brenner's

[1] The material presented in this Chapter was published in T. Goldfriend, H. Diamant, and T. A. Witten, Phys. Fluids **27**, 123303 (2015) [127].

analytical framework [14, 129], specializing to the leading order of the HI in the distance between the objects (multipole expansion, also known as the method of reflections [32]). The second part addresses the time-dependent trajectories of forced objects. This is a multi-variable, highly non-linear dynamical system exhibiting complex and diverse dynamics. In this second part we are limited to numerical integration of the objects' trajectories. First, in Sec. 2.3 we derive the resulting properties of model self-aligning objects composed of four stokeslets. Then, in Sec. 2.4 we use them to perform numerical time integration for the evolution of randomly generated object pairs and their alignment.

2.1 Pair-Mobility Matrix: General Considerations

We begin by discussing the general properties and symmetries of the pair-mobility matrix for two arbitrarily shaped objects.

2.1.1 Structure of the Pair-Mobility Matrix

Consider two arbitrarily shaped rigid objects, a and b, with typical size ℓ, subject to external forces and torques $\mathbf{F}^a$, $\mathbf{F}^b$ and $\boldsymbol{\tau}^a$, $\boldsymbol{\tau}^b$ in an unbounded, otherwise quiescent fluid of viscosity η. In the inertia-less regime, the objects respond with linear and angular velocities to the external forces and torques through a 12×12 pair-mobility matrix (see Sec. 1.5),

$$\begin{pmatrix} \underline{\mathbf{V}}^a \\ \underline{\mathbf{V}}^b \end{pmatrix} = \frac{1}{\eta\ell} \begin{pmatrix} \mathbb{M}^{aa} & \mathbb{M}^{ab} \\ \mathbb{M}^{ba} & \mathbb{M}^{bb} \end{pmatrix} \begin{pmatrix} \underline{\mathbf{F}}^a \\ \underline{\mathbf{F}}^b \end{pmatrix}, \tag{2.1}$$

where we define *generalized velocity* and *generalized force* 6-vectors, $\underline{\mathbf{V}}^x = (\mathbf{V}^x, \ell\boldsymbol{\omega}^x)^T$ and $\underline{\mathbf{F}}^x = (\mathbf{F}^x, \boldsymbol{\tau}^x/\ell)^T$ for $x = a, b$. We hereafter omit the factor $(\eta\ell)^{-1}$ (i.e., set $\eta\ell = 1$). This, together with the representation of the generalized forces and velocities, make the pair-mobility $\mathbb{M}$ dimensionless and dependent on the geometry alone. Since $\mathbf{V}$ and $\boldsymbol{\tau}$ depend on the choice of object origins, so does the pair-mobility matrix. The transformation between pair-mobility matrices corresponding to different origins is given in Appendix A.1.

The pair-mobility matrix is a function of the objects' geometries, their orientations, and the vector connecting their origins, indicated hereafter by $\mathbf{R}$. (We define the direction of $\mathbf{R}$ from the origin of object b to the origin of object a.) The geometry of object x is denoted by $\underline{\mathbf{r}}^x$. For example, if the object consists of a discrete set of N_x stokeslets (see Sec. 1.4.4), then $\underline{\mathbf{r}}^x$ is a $3N_x$-vector specifying the positions of the stokeslets; otherwise, it represents the surface of the object.

The pair-mobility matrix is positive-definite and symmetric [31–33]. Hence, $\mathbb{M}^{ab} = (\mathbb{M}^{ba})^T$,

and the self-blocks can be written as

$$\mathbb{M}^{xx} = \begin{pmatrix} \mathbb{A}^{xx} & (\mathbb{T}^{xx})^T \\ \mathbb{T}^{xx} & \mathbb{S}^{xx} \end{pmatrix}.$$

As in the analysis of Ref. [34] for isolated objects, the self-mobility matrix contains the following 3×3 blocks: the alacrity matrix $\mathbb{A}$ (translational response to force); the screw matrix $\mathbb{S}$ (rotational response to torque); and the twist matrix $\mathbb{T}$ (translation–rotation coupling). The twist matrix characterizes the alignability and chiral response of the object (the sense of rotation under a force). In the present Chapter we deal with self-aligning objects, whose individual $\mathbb{T}$ is necessarily non-vanishing; see Sec. 1.4.2. Furthermore, in the case of a pair of objects, the presence of the other object makes the self-twist matrix, $\mathbb{T}^{xx}$, differ from the single-object one. As to the off-diagonal blocks of the pair-mobility matrix, the symmetry of $\mathbb{M}$ (see Sec. 1.5) implies the following structure:

$$\mathbb{M}^{ab} = \begin{pmatrix} \mathbb{A}^{ab} & (\mathbb{T}^{ba})^T \\ \mathbb{T}^{ab} & \mathbb{S}^{ab} \end{pmatrix}, \quad \mathbb{M}^{ba} = \begin{pmatrix} (\mathbb{A}^{ab})^T & (\mathbb{T}^{ab})^T \\ \mathbb{T}^{ba} & (\mathbb{S}^{ab})^T \end{pmatrix}.$$

2.1.2 Further Symmetries of the Pair-Mobility Matrix

The discussion in the preceding subsection has been for a general pair of objects, which are not necessarily identical. In the present subsection, we focus on the case in which the two objects are *identical in shape and orientation*, i.e., $\underline{\mathbf{r}}^a = \underline{\mathbf{r}}^b \equiv \underline{\mathbf{r}}$. Our goal is to understand what the instantaneous relative velocities (linear and angular) between the two objects are, when the objects are subjected to the same external forcing. The restriction to identical objects makes $\mathbb{M}$ invariant under exchange of objects. This additional symmetry is made of two operations: interchanging the blocks $\mathbb{M}^{aa} \leftrightarrow \mathbb{M}^{bb}$ and $\mathbb{M}^{ab} \leftrightarrow \mathbb{M}^{ba}$; and inversion of $\mathbf{R}$. That is,

$$\mathbb{M}(\underline{\mathbf{r}}, \mathbf{R}) = \mathbb{E}\mathbb{M}(\underline{\mathbf{r}}, -\mathbf{R})\mathbb{E}^{-1}, \tag{2.2}$$

where $\mathbb{E}$ is a 12×12 matrix which interchanges the objects,

$$\mathbb{E} = \begin{pmatrix} 0 & \mathbb{I}_{6\times 6} \\ \mathbb{I}_{6\times 6} & 0 \end{pmatrix}, \tag{2.3}$$

with $\mathbb{I}_{6\times 6}$ denoting the 6×6 identity matrix.

The symmetry to object exchange, when combined with the parity of $\mathbb{M}$ (i.e., whether it remains the same or changes sign) under $\mathbf{R}$-inversion[2] has important consequences for the effect of HI on alignment. If $\mathbb{M}$ has a definite parity one can determine what the relative response of the objects to forcing is — i.e., whether they attain the same or the opposite linear

[2] Parity does not mean here symmetry under full spatial inversion, as such an operation would turn the chiral objects into their enantiomers; rather, we mean here symmetry under the inversion of $\mathbf{R}$.

and angular velocities. If the term is symmetric to inversion, the velocities would be identical, and if it is antisymmetric, they would be opposite. This is because

$$\begin{pmatrix} \mathbb{M}^{aa}(\mathbf{R}) & \mathbb{M}^{ab}(\mathbf{R}) \\ \mathbb{M}^{ba}(\mathbf{R}) & \mathbb{M}^{bb}(\mathbf{R}) \end{pmatrix} = \pm \begin{pmatrix} \mathbb{M}^{aa}(-\mathbf{R}) & \mathbb{M}^{ab}(-\mathbf{R}) \\ \mathbb{M}^{ba}(-\mathbf{R}) & \mathbb{M}^{bb}(-\mathbf{R}) \end{pmatrix} = \pm \begin{pmatrix} \mathbb{M}^{bb}(\mathbf{R}) & \mathbb{M}^{ba}(\mathbf{R}) \\ \mathbb{M}^{ab}(\mathbf{R}) & \mathbb{M}^{aa}(\mathbf{R}) \end{pmatrix}, \tag{2.4}$$

where the second equality comes from the response to exchange of objects, Eq. (2.2). Consequently, under identical forcing of the two objects one finds,

$$\underline{\mathbf{V}}^a = \left(\mathbb{M}^{aa} + \mathbb{M}^{ab}\right) \underline{\mathbf{F}} = \pm \left(\mathbb{M}^{bb} + \mathbb{M}^{ba}\right) \underline{\mathbf{F}} = \pm \underline{\mathbf{V}}^b. \tag{2.5}$$

Thus, since any $\mathbb{M}$ can be decomposed into even and odd terms, we find that only the odd ones cause relative motions of the two objects.

The pair-mobility as a whole, however, never has a definite parity under $\mathbf{R}$-inversion, i.e., it is made of both even and odd terms. This becomes clear when $\mathbb{M}(\underline{\mathbf{r}}, \mathbf{R})$ is expanded in small ℓ/R, i.e., in multipoles. A general discussion of the parity of each multipole term is given in the next section. For now, let us consider those two leading multipoles which are independent of the objects' shape, and therefore always exist. The monopole–monopole interaction (Oseen tensor in Eq. (1.15)), which is the leading term in $\mathbb{A}^{ab}$ making object a translate due to the force on object b, is symmetric under $\mathbf{R}$-inversion. The part of the monopole–dipole interaction causing the second object to rotate due to the force on the first, i.e., the leading term in $\mathbb{T}^{ab}$, is antisymmetric. For example, even the most symmetric pair of objects — two spheres — has an $\mathbf{R}$-symmetric $\mathbb{A}^{ab}$, leading to zero relative velocity, and an $\mathbf{R}$-antisymmetric $\mathbb{T}^{ab}$, causing them to rotate with opposite senses under an identical force [32]. Thus, for a general object, the highest order which maintains $\mathbb{M}$ of definite parity is the monopole $1/R$ Oseen one, which is even. (The self-blocks are constant up to order $1/R^4$; see below.)

From this discussion we can immediately conclude that, to leading order in the separation of two identical, fully aligned objects, *their instantaneous hydrodynamic interaction must linearly degrade the alignment*. The leading degrading term comes from $\mathbb{T}^{ab}$, their rotational response to force, and is of order $1/R^2$. It is worthwhile to note again that such a rotational response is present as well for a pair of uniform spheres or spheroids; yet, such regular objects are not self-aligning to begin with.

The relation between object-exchange symmetry and the symmetry of the linear-velocity response is intimately related to the issue of hydrodynamic pseudopotentials (Sec. 1.5.1), which will be discussed in detail in Chapter 3.

2.2 Far-Field Interaction: Multipole Expansion

There are two characteristic length scales in our problem: the typical size of the objects, ℓ, and the distance between them, $R = |\mathbf{R}|$. If $\ell \ll R$, we can write the pair-mobility matrix as a power series in (ℓ/R),

$$\mathbb{M} = \mathbb{M}_{(0)} + \mathbb{M}_{(1)} + \mathbb{M}_{(2)} + \dots,$$

where $\mathbb{M}_{(n)} \sim (\ell/R)^n$. The analysis of this expansion as given below holds for any pair of objects, whether identical or not. The zeroth order, $\mathbb{M}_{(0)}$, is a block diagonal matrix which is made of the self-mobilities of the two non-interacting objects. (These should be distinguished from $\mathbb{M}^{aa}$ and $\mathbb{M}^{bb}$, the self-mobilities of the interacting objects.)

The hydrodynamic multipole expansion (also known as the method of reflections) is based on the Green's function of Stokes flow, the Oseen tensor in Eq. (1.15). Using the simplified units of this Chapter ($\eta\ell = 1$), it is given by

$$\mathbb{G}_{ij}(\mathbf{r}) = \frac{1}{8\pi}\frac{\ell}{r}\left(\delta_{ij} + \frac{r_i r_j}{r^2}\right). \tag{2.6}$$

This is a symmetric 3×3 tensor, invariant under $\mathbf{r}$-inversion. A point force at $\mathbf{r}_0$, $\delta(\mathbf{r} - \mathbf{r}_0)\mathbf{f}$, generates a velocity field $\mathbf{u}(\mathbf{r}) = \mathbb{G}(\mathbf{r} - \mathbf{r}_0) \cdot \mathbf{f}$.

We obtain two general results concerning the multipoles of the HI between two arbitrary objects. The two objects need not be identical[3]. The proofs are given in Appendix A.2.

1. *The leading interaction multipole in the self-blocks of the pair-mobility matrix is $n = 4$. That is, any response of one object to forces on itself, owing to the other object, must fall off with distance R between the objects at least as fast as R^{-4}.*

2. *The nth multipole has self-blocks of $(-1)^n$ parity, and coupling blocks of the opposite, $(-1)^{n+1}$ parity. Thus, e.g., the leading term in $\mathbb{M}^{aa}$, proportional to R^{-4}, is invariant under $\mathbf{R}$-inversion, and the R^{-4} part of $\mathbb{M}^{ab}$ changes sign under $\mathbf{R}$-inversion. Likewise for the multipole varying as $\mathbf{R}^{-5}$, the $\mathbb{M}^{aa}$ changes sign under $\mathbf{R}$-inversion while $\mathbb{M}^{ab}$ remains invariant.*

These statements pertain to the mobility matrix. As to the propulsion matrix (the inverse of the mobility matrix), the leading correction to the self-block becomes $\sim 1/R^2$, and the second statement concerning parity remains intact.

We now consider for a moment two identical objects and specialize to the first and second multipoles, i.e., the HI up to order $1/R^2$. The discussion in the preceding and current sections

[3] In fact, these results are not special to the HI but can be similarly proven for any multipole expansion. As such, they were most probably derived before.

implies the following form of the two leading terms in the pair-mobility matrix:

$$\mathbb{M}_{(1)} = \begin{pmatrix} 0 & \mathbb{M}^{ab}_{(1)} \\ \mathbb{M}^{ab}_{(1)} & 0 \end{pmatrix}, \qquad \mathbb{M}_{(2)} = \begin{pmatrix} 0 & \mathbb{M}^{ab}_{(2)} \\ -\mathbb{M}^{ab}_{(2)} & 0 \end{pmatrix}. \tag{2.7}$$

In more detail: there are no first- and second-order corrections to the objects' self-mobility. Hence, these two multipoles have definite parities — the first is even, and the second is odd. Consequently, the first multipole does not cause any relative motion of the two objects, whereas the second mutipole makes them translate and rotate in opposite linear and angular velocities.

The essential characteristics of the first two multipoles are schematically illustrated in Fig. 2.1. The first multipole arises directly from the Green's function,

$$\mathbb{M}^{ab}_{(1)} = \begin{pmatrix} \mathbb{G}(\mathbf{R}) & 0 \\ 0 & 0 \end{pmatrix}, \tag{2.8}$$

where $\mathbb{G}(\mathbf{R})$ is the Oseen tensor, given in Eq. (2.6).

In the interaction described by the second multipole one object sees the other as a point, see Fig. 2.1. Accordingly, this term contains two types of interaction: (1) the response of object a to the non-uniformity of the flow due to the force monopole at object b (regarded as a point); (2) the advection of object a (regarded as a point) by the flow due to the force dipole acting at object b. These two effects are both proportional to $\boldsymbol{\nabla}\mathbb{G}(\mathbf{R}) \sim 1/R^2$. Each can be written as a product of a tensor which arises from the medium alone, through derivatives of the Oseen tensor $\boldsymbol{\nabla}\mathbb{G}(\mathbf{R})$, and another tensor which depends on the objects' geometry. The second-order correction to the velocity of object a is given by the sum of these two effects, each expressed in terms of a coupling tensor Θ and an object tensor Φ

$$\begin{aligned} \underline{\mathbf{V}}^a_{(2)} &= \mathbb{M}^{ab}_{(2)} \cdot \underline{\mathbf{F}}^b \\ \mathbb{M}^{ab}_{(2)} &= \Phi^a : \Theta(\mathbf{R}) - \Theta^T(\mathbf{R}) : \tilde{\Phi}^b, \end{aligned} \tag{2.9}$$

where the double dot notation denotes a contraction over two indices. Eq. (2.9) contains three tensors of rank 3, denoted by capital Greek letters. The first, Φ, with dimensions $6 \times 3 \times 3$, gives the generalized velocity of the object in linear response to the velocity gradient of the flow in which it is embedded. The second, $\tilde{\Phi}$, having dimensions $3 \times 3 \times 6$, gives the force dipole acting on the fluid around the object's origin in linear response to the generalized force acting on it. Both Φ and $\tilde{\Phi}$ depend on the objects' geometry alone[4]. The third tensor, Θ, with dimensions $3 \times 3 \times 6$, describes the coupling of these object responses through the fluid. It is given by

$$\Theta_{skj}(\mathbf{R}) \equiv \begin{cases} \partial_s \mathrm{G}_{kj}(\mathbf{r})|_{\mathbf{R}} & j = 1,2,3 \\ 0 & j = 4,5,6. \end{cases} \tag{2.10}$$

[4]These tensors are related to the two introduced by Brenner [129]. Brenner's tensors give the force and torque exerted on an object in linear response to a flow gradient in which it is embedded. Our Φ is related to these two via the individual self-mobility matrix.

Repeating the same procedure for $\underline{\mathbf{V}}^b$ in response to $\underline{\mathbf{F}}^a$ while using the odd parity of Θ, we get

$$\mathbb{M}^{ba}_{(2)} = \Theta^T(\mathbf{R}) : \tilde{\Phi}^a - \Phi^b : \Theta(\mathbf{R}). \tag{2.11}$$

The tensors Φ and $\tilde{\Phi}$ are not independent [24]. We now show that $\Phi = \tilde{\Phi}^T$. The symmetry of $\mathbb{M}$ implies that each multipole is also a symmetric matrix. Using Eq. (2.9) and Eq. (2.11), and equating $(\mathbb{M}^{ba}_{(2)})^T = \mathbb{M}^{ab}_{(2)}$, we get $\tilde{\Phi}^a = (\Phi^a)^T$ and $\tilde{\Phi}^b = (\Phi^b)^T$.

To summarize, the matrix $\mathbb{M}_{(2)}$ is given by

$$\mathbb{M}_{(2)} = \begin{pmatrix} 0 & \Phi^a : \Theta(\mathbf{R}) - [\Phi^b : \Theta(\mathbf{R})]^T \\ -\Phi^b : \Theta(\mathbf{R}) + [\Phi^a : \Theta(\mathbf{R})]^T & 0 \end{pmatrix}. \tag{2.12}$$

This results is valid for a general pair of objects. If the two objects are identical, the off-diagonal blocks have the same form with opposite signs. The additional condition that the entire $\mathbb{M}$ must be symmetrical implies then that each block by itself is antisymmetric.

By separating the tensors Φ and Θ into their symmetric and antisymmetric parts, the second-order term of the pair-mobility matrix can be simplified further. It should be mentioned, in addition, that the Φ tensor depends on the origin selected for the object. These two technical issues are addressed in Appendix A.3 and Appendix B, respectively. Finally, we note that the terms in these tensors corresponding to the translational response vanish for spheres and spheroids. Consequently, two such regular objects develop relative velocity only to orders $1/R^3$ and above (if at all; see Chapter 3).

2.3 Numerical Analysis for Stokeslet Objects

In the preceding sections we have derived the general properties of the instantaneous HI between two arbitrarily shaped objects. We now move on to the second part of this Section, addressing the time evolution of the two objects. This complicated problem is not tractable analytically, and we resort to numerical integration of specific examples. Because of the complexity of the problem, and since we are interested in generic properties, we allow ourselves to restrict the analysis to the simplest, even if unrealistic, objects— stokeslets objects (see Sec. 1.4.4). The sparseness of these objects makes them free-draining, which may be valid for macromolecules but not for compact objects.

We treat pairs of identical objects, each made of four stokeslets. To obtain representative sampling of numerical examples we do not design these objects but create them randomly. Four points are placed at random distances ranging between 0 and 1 from an arbitrary origin. The origin is then shifted to the points' center of mass. The radius ϱ of the stokeslets is taken

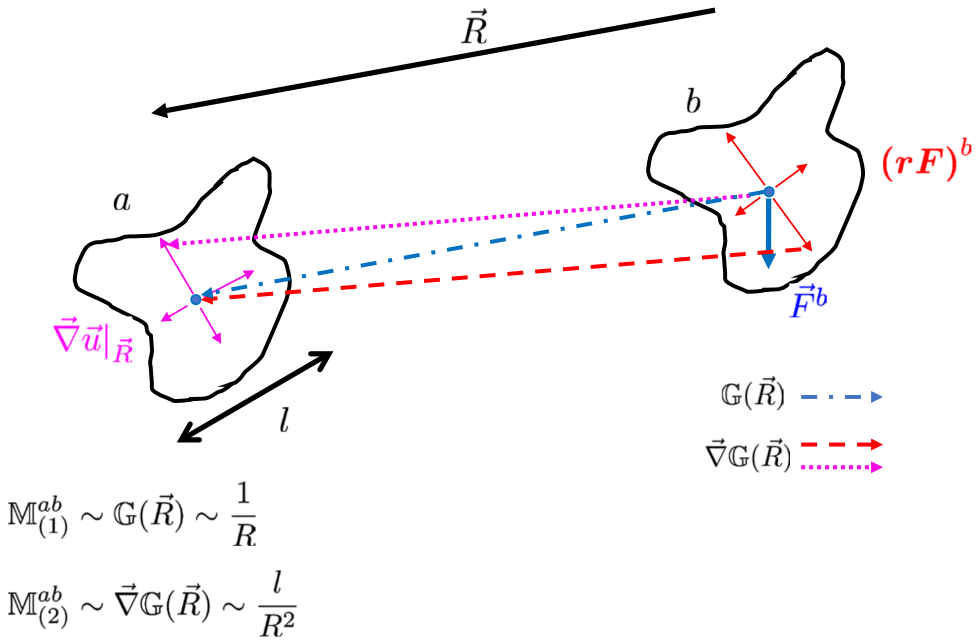

Figure 2.1: Illustration of the two leading orders of the hydrodynamic interaction between two forced objects. The leading term in the pair-mobility matrix (light blue/dash-dotted arrow between the objects' origins), decaying as $1/R$, comes from the point-like response of object a to the local flow caused by the force monopole on object b (blue/thick arrow). The next-order term, decaying as ℓ/R^2, has two contributions: (i) The point-like response of object a to the local flow caused by the force dipole on object b (red/dashed arrow from the red/thin arrows at object b to the origin of a). (ii) The response of object a to the local flow gradient caused by the force monopole on object b (magenta/dotted arrow from the origin of b to the magenta/thin arrows at object a).

as 0.01. The resulting configuration is checked to be "sufficiently chiral", in the sense that the $\mathbb{T}$-matrix of the individual object is strongly asymmetric, having a single real eigenvalue of absolute value $|\lambda_3| > 0.005$, which makes the object self-aligning (see Sec. 1.4.3). Examples of the stokeslets objects we use are provided in Fig. 2.2.

The way to calculate the mobility of a single stokeslet object has been presented in Sec. 1.4.4. First, we briefly present in Sec. 2.3.1 the simple extension of this method to pair-mobilities. We calculate both the pair-mobility and the tensor Φ introduced in Sec. 2.1 and Sec. 2.2. The latter allows us to more efficiently calculate pair mobilities up to second order in the multipole expansion. Sec. 2.3.2 describes how we use the pair-mobility to numerically calculate the time evolution of the pair configuration.

2.3.1 Pair-Mobility and Φ Tensor

As demonstrated in Sec. 1.4.4 the properties of a stokeslets object can be derived self-consistently from the linear relations which describe the stokeslets' configuration. This is done without finding the stokeslets' strengths explicitly. Below we find the pair-mobility matrix, and the Φ tensor associated with a single object, given the stokeslet configuration and the size of the spheres that they represent.

Each of the two objects, $x = a, b$, consists of N_x stokeslets, $\underline{\mathbf{f}}^x = (\mathbf{f}_1^x, \ldots, \mathbf{f}_{N_x}^x)$, in a known configuration, $\underline{\mathbf{r}}^x = \left(\mathbf{r}_1^x, \ldots, \mathbf{r}_{N_x}^x\right)$. (We recall the notation, introduced in Sec. 1.8, where an underlined letter denotes a set of N 3-vectors.) Here $\mathbf{r}_n^x$ indicates the position 3-vector of the nth stokeslet in object x with respect to the object's origin. Each stokeslet is a sphere of radius ϱ, where $\varrho < \min(r_1^x, \ldots, r_{N_x}^x)$. The velocities of the spheres, $\underline{\mathbf{v}}_n^x$, are known from the object's linear and angular velocities,

$$\begin{pmatrix} \underline{\mathbf{v}}^a \\ \underline{\mathbf{v}}^b \end{pmatrix} = \begin{pmatrix} \mathbb{U}^a & 0 \\ 0 & \mathbb{U}^b \end{pmatrix} \begin{pmatrix} \underline{\mathbf{V}}^a \\ \underline{\mathbf{V}}^b \end{pmatrix}, \qquad \text{with } \mathbb{U}^x = \begin{pmatrix} \mathbb{I}_{3\times 3}, -\mathbf{r}_1^{x\,\times}/\ell \\ \vdots \\ \mathbb{I}_{3\times 3}, -\mathbf{r}_{N_x}^{x\,\times}/\ell \end{pmatrix}, \quad \text{for } x = a, b, \tag{2.13}$$

where the matrix $\mathbf{y}^\times$ obtained from the vector $\mathbf{y}$ is as defined in the Sec. 1.8, $(\mathbf{y}^\times)_{ij} = \epsilon_{ikj} y_k$. Each stokeslet force is proportional to the relative velocity of the sphere that it represents with respect to the flow around it as created by the other stokeslets. This gives a linear relation between the stokeslets and the velocities of the spheres[5],

$$\begin{pmatrix} \underline{\mathbf{v}}^a \\ \underline{\mathbf{v}}^b \end{pmatrix} = \begin{pmatrix} \mathbb{L}^{aa} & \mathbb{L}^{ab} \\ \mathbb{L}^{ab\,T} & \mathbb{L}^{bb} \end{pmatrix} \begin{pmatrix} \underline{\mathbf{f}}^a \\ \underline{\mathbf{f}}^b \end{pmatrix}, \quad \text{where} \tag{2.14}$$

[5] An explicit derivation of this relation is given in Sec. 1.4.4.

$$
\begin{aligned}
(\mathbb{L}^{xx}_{nm})_{ij} &= \begin{cases} \mathbb{G}_{ij}(\mathbf{r}^x_n - \mathbf{r}^x_m) & \text{if } n \neq m \\ (6\pi\varrho/\ell)^{-1}\delta_{ij} & \text{if } n = m \end{cases} \\
(\mathbb{L}^{ab}_{nm})_{ij} &= \mathbb{G}_{ij}(\mathbf{R} + \mathbf{r}^a_n - \mathbf{r}^b_m).
\end{aligned} \tag{2.15}
$$

First we find the pair-mobility matrix as a generalization of the analysis presented in Sec. 1.4.4. The sum of the stokeslets and the corresponding total torque must be equal to the external generalized forces applied on the objects. In a matrix form we can write

$$
\begin{pmatrix} \underline{\mathbf{F}}^a \\ \underline{\mathbf{F}}^b \end{pmatrix} = \begin{pmatrix} (\mathbb{U}^a)^T & 0 \\ 0 & (\mathbb{U}^b)^T \end{pmatrix} \begin{pmatrix} \underline{\mathbf{f}}^a \\ \underline{\mathbf{f}}^b \end{pmatrix}. \tag{2.16}
$$

Using Eq. (2.13) and Eq. (2.14), we have

$$
\begin{pmatrix} \mathbb{U}^a & 0 \\ 0 & \mathbb{U}^b \end{pmatrix}^T \cdot \begin{pmatrix} \mathbb{L}^{aa} & \mathbb{L}^{ab} \\ \mathbb{L}^{ab\,T} & \mathbb{L}^{bb} \end{pmatrix}^{-1} \cdot \begin{pmatrix} \mathbb{U}^a & 0 \\ 0 & \mathbb{U}^b \end{pmatrix} \cdot \begin{pmatrix} \underline{\mathbf{V}}^a \\ \underline{\mathbf{V}}^b \end{pmatrix} = \begin{pmatrix} \underline{\mathbf{F}}^a \\ \underline{\mathbf{F}}^b. \end{pmatrix}
$$

From this expression we identify the pair-mobility matrix as

$$
\mathbb{M} = \left[\begin{pmatrix} \mathbb{U}^a & 0 \\ 0 & \mathbb{U}^b \end{pmatrix}^T \cdot \begin{pmatrix} \mathbb{L}^{aa} & \mathbb{L}^{ab} \\ \mathbb{L}^{ab\,T} & \mathbb{L}^{bb} \end{pmatrix}^{-1} \cdot \begin{pmatrix} \mathbb{U}^a & 0 \\ 0 & \mathbb{U}^b \end{pmatrix} \right]^{-1}. \tag{2.17}
$$

This expression allows to calculate the pair-mobility matrix, with the help of Eq. (2.13) and Eq. (2.15), based on the stokeslets' configuration and the Oseen tensor alone.

Next, we derive the Φ^x tensor of a stokeslets object x. From this tensor we may readily obtain the second multipole of the pair interaction (cf. Sec. 2.2). The force dipole around the origin of a forced object is given by Eq. (2.9), $(\underline{\mathbf{rf}})^x \equiv (\Phi^x)^T \cdot \underline{\mathbf{F}}^x$. Similar to the $\mathbb{U}^x$ matrix relating the stokeslets to the total generalized force, $\underline{\mathbf{F}}^x = (\mathbb{U}^x)^T \cdot \underline{\mathbf{f}}^x$, we define a tensor of rank 3, Y^x, which relates the stokeslet forces to the total force dipole on the object by $(\underline{\mathbf{rf}})^x = (\mathrm{Y}^x)^T \cdot \mathbf{F}^x$. (Note that no force dipole is applied on the individual stokeslets; being arbitrarily small they possess only a force monopole.) Specifically, it is made of N blocks of $3 \times 3 \times 3$, given by $(\mathrm{Y}_n)_{ijs} = r_{n,s}\delta_{ij}$, $n = 1 \ldots N$, $i, j, s = 1, 2, 3$ (i.e., $r_{n,s}$ is the s Cartesian coordinate of the stokeslet n). Using Eq. (2.13) and Eq. (2.14), we have $(\underline{\mathbf{rf}})^a = (\mathrm{Y}^a)^T \cdot (\mathbb{L}^{aa})^{-1} \cdot \mathbb{U}^a \cdot \underline{\mathbf{V}}^a$. This implies $(\Phi^x)^T = (\mathrm{Y}^x)^T \cdot (\mathbb{L}^{xx})^{-1} \cdot \mathbb{U}^x \cdot \mathbb{M}^x_{\mathrm{self}}$. Recalling that the matrices $\mathbb{M}_{\mathrm{self}}$ and $\mathbb{L}$ are symmetric, we finally get

$$
\Phi^x = \mathbb{M}^x_{\mathrm{self}} \cdot (\mathbb{U}^x)^T \cdot (\mathbb{L}^{xx})^{-1} \cdot \mathrm{Y}^x. \tag{2.18}
$$

It is important to note that in the above derivation we compute $\mathbb{M}$ and Φ under the assumption that, for each object, the stokeslet sizes are arbitrarily small compared to the distances between them, $\varrho \ll \ell$ (where ℓ is the object's radius of gyration). However, in a more general case one can use the Rotne-Prager-Yamakawa tensor [51, 52], which corrects the Oseen tensor for force distributions with finite size [49].

2.3.2 Numerical Time Integration

We present a numerical integration scheme for the dynamics of two stokeslet objects. We should first define the reference frames used in the scheme. Each rigid object is characterized by axes which are affixed and rotate with it. We define the body frame such that its z axis coincides with the object's alignment axis (the corresponding eigenvector of the $\mathbb{T}$-matrix). The other two axes are selected arbitrarily. The z axis of the laboratory frame is defined along the forcing direction. During the evolution we follow the translation and rotation of the body frame in the laboratory frame.

We represent the orientation of an object by the Euler-Rodrigues 4-parameters [126], $(\Gamma, \mathbf{\Omega}) \equiv (\cos\frac{\theta}{2}, \hat{\mathbf{n}}\sin\frac{\theta}{2})$, where $\hat{\mathbf{n}}$ and θ are the axis and angle of rotation. The properties of this representation are given in Sec. 1.7.

Since we choose the body frame such that the z-axis is the axis of alignment, the terminal orientation of a self-aligning object under a constant force along the z-axis is $(\Gamma, \mathbf{\Omega}) = (\cos(\frac{\omega t+\zeta}{2}), \hat{\mathbf{z}}\sin(\frac{\omega t+\zeta}{2}))$, where ζ is a constant phase which depends on the object's initial orientation at time $t = 0$.

The state of a pair of objects at time t is described by the position of the origins of the objects, $\mathbf{R}^a(t)$ and $\mathbf{R}^b(t)$, and their orientation parameters, $(\Gamma^a(t), \mathbf{\Omega}^a(t))$ and $(\Gamma^b(t), \mathbf{\Omega}^b(t))$. We time-integrate from the initial state, $\mathbf{R}^a_0 = (0,0,0)$, $\mathbf{R}^a_0 - \mathbf{R}^b_0 = \mathbf{R}_0$, $(\Gamma^a_0, \mathbf{\Omega}^a_0)$ and $(\Gamma^b_0, \mathbf{\Omega}^b_0)$, as follows. Given the positions of the stokeslets at time t, the pair-mobility matrix, $\mathbb{M}(t)$, is calculated as explained in Sec. 2.3.1, *either exactly or using the multipole approximation*. Then, the linear and angular velocities of the objects are given by $(\underline{\mathbf{V}}^a(t), \underline{\mathbf{V}}^b(t))^T = \mathbb{M}(t)\cdot(\underline{\mathbf{F}}^a(t), \underline{\mathbf{F}}^b(t))^T$. From them the origins and orientations of the objects at time $t + dt$ are derived according to

$$\mathbf{R}^x(t+dt) = \mathbf{R}^x(t) + \mathbf{V}^x(t)dt \tag{2.19}$$

$$\begin{pmatrix}\Gamma^x(t+dt)\\ \mathbf{\Omega}^x(t+dt)\end{pmatrix} = \exp\left[\frac{dt}{2}\begin{pmatrix}0 & -\boldsymbol{\omega}^{xT}\\ \boldsymbol{\omega}^x & \boldsymbol{\omega}^{x\times}\end{pmatrix}\right]\begin{pmatrix}\Gamma^x(t)\\ \mathbf{\Omega}^x(t)\end{pmatrix} \tag{2.20}$$

for $x = a, b$. During the evolution we make sure that the small stokeslet spheres do not overlap, and that the pair-mobility matrix remains positive-definite. In practice we never encountered such problems when using the exact pair-mobility matrices; when it did happen in the case of the multipole approximation we stopped the integration.

We define a scalar order parameter which characterizes the degree of mutual alignment of the two objects,

$$m \equiv \left[(\Gamma^a, \mathbf{\Omega}^a)\cdot(\Gamma^b, \mathbf{\Omega}^b)\right]^2 = \left(\Gamma^a\Gamma^b + \mathbf{\Omega}^a\cdot\mathbf{\Omega}^b\right)^2. \tag{2.21}$$

As required, the order parameter is invariant under 3-rotation (see property 6 in Sec. 1.7). When the objects are aligned, $(\Gamma^a, \mathbf{\Omega}^a) = \pm(\Gamma^b, \mathbf{\Omega}^b)$, and $m = 1$; otherwise $0 \le m < 1$. In the

case of partial alignment, $m = \cos^2(\frac{\Delta\zeta}{2})$, where $\Delta\zeta$ is the mutual phase difference[6].

Another scalar property of the two-object system is the energy dissipation rate. At time t, the latter is given by

$$\dot{E}_{\text{dissipation}} = \underline{\mathbf{V}}^a(t) \cdot \underline{\mathbf{F}}^a(t) + \underline{\mathbf{V}}^b(t) \cdot \underline{\mathbf{F}}^b(t). \tag{2.22}$$

Since the pair-mobility matrix is positive definite the energy dissipation of the driven pair is positive at all times (as demanded by the second law of thermodynamics).

2.4 Numerical Results: Effect on Alignment

We present in Fig. 2.3–Fig. 2.8 several examples for the numerically integrated evolution of object pairs under various conditions. One can immediately appreciate the diversity of possible trajectories. To make your way through this richness it is important to make two distinctions between types of trajectories. The first distinction is between constant forcing (as in sedimentation), which can make the objects only partially aligned without synchronizing their phases of rotation [34, 43], and a time-dependent forcing protocol, which is known to lock the phase of an individual object onto that of the force [46, 47]. The main issue examined below is how the presence of HI affects these two behaviors. The second distinction, therefore, is whether HIs are included (dashed, dotted and dash-dotted/colored curves) or turned off (solid gray curves). In the absence of HIs (or when they get weak as the objects move far apart), the time-dependent aligning force will make the objects fully synchronized, whereas under constant forcing the objects will generally become unaligned.

The results are presented in a dimensionless form, using units such that $\eta = |\omega_0| = 1$ and $\varrho = 0.01$. The distances between the stokeslets of each object are taken randomly between 0 and 1; hence, $\varrho \ll \ell \sim 1$. The time-dependent forcing protocol is defined according to Ref. [47]:

$$\mathbf{F} = F_0 \left(-\sin(\omega_0 t)\sin(\theta), \cos(\omega_0 t)\sin(\theta), -\cos(\theta) \right),$$

where $\theta = 0.1\pi$, $F_0 = -|\lambda_3|^{-1}$, $\omega_0 = \text{sign}(\lambda_3)$ and λ_3 is the real eigenvalue of the single-object twist matrix. We examine both the trajectories of the separation vector connecting the origins of the two objects, and the corresponding evolution of the alignment order parameter.

We begin with the case of a time-dependent forcing, Fig. 2.3 and Fig. 2.4. The first observation, most clearly demonstrated in Fig. 2.4(b), is that HI degrades the alignment of the two objects, as has been rigorously inferred based on symmetry considerations in Sec. 2.1.2. Another conclusion, supported by additional examples not shown here, is that most objects, which start sufficiently far apart, especially if they start fully aligned, tend to repel each other

[6] If the symmetry of the objects is such that their phase difference is unobservable (e.g., two spheroids rotating around their major axis), then we set it to zero.

(Fig. 2.3). Even if they are not fully aligned, the growing distance and weakening interaction make them individually more aligned with the forcing, and therefore also mutually synchronized. Thus, the repulsion helps restore the alignment at long times. The increasing separation occurs in the xy plane, while along the z axis the separation decreases and saturates to a finite distance, dependent on initial conditions, see Fig. 2.3. The nature of this effective repulsion will be addressed in Chapter 3, where we discuss in detail the effect of HI on the relative translation of object pairs.

The repulsion is accompanied by a decrease in dissipation rate (up to small oscillations), as demonstrated in Fig. 2.7. When the HI is turned off, the dissipation rate reaches a constant value as the two independent objects set into their ultimate aligned state (solid curves in Fig. 2.7).

The repulsive effect is observed for most examples of our randomly generated pairs of objects but is not a general law. For instance, when the objects start at a sufficiently small separation, some pairs remain "bound" in a limit cycle, oscillating about a certain mean separation and mean orientational alignment, as demonstrated by the green/dashed curves in Fig. 2.3 and Fig. 2.4.

In Fig. 2.5 and Fig. 2.6 we examine the same properties under constant forcing. The two effects— degradation in the alignment of a pair which is initially fully aligned, and mutual repulsion— are observed here as well. Yet, in the absence of a time-dependent aligning force, as the two objects move apart, alignment is not restored. At long times, and for the common case of repulsion, we distinguish between two observed behaviors: a) The order parameter continues to change without saturating to a constant value (e.g., red/dash-dotted curve and cyan/dotted curve in Fig. 2.6(a) and Fig. 2.6(b), respectively). This non-intuitive result can be explained as follows. The fact that the interaction becomes weak does not necessarily imply that the accumulation of phase difference stops. If the two distant objects are partially aligned we have $m \simeq \cos^2(\delta\omega_z t/2)$, where $\delta\omega_z$ is the difference between the objects' angular velocity along the alignment axis. Hence, if the decay of $\delta\omega_z$ with time is slower then t^{-1} then phase difference will continue to accumulate. This depends on the detailed dynamics of repulsion which will be addressed in Chapter 3. b) The other option is that m converges to some value dependent on the initial state, with no particular chosen m (green/dash-dotted curve in Fig. 2.6(b) and cyan/dash-dotted curve in Fig. 2.6(c)), i.e., the two objects continue to rotate with a fixed relative orientation. In the examples that we checked there seems to be a tendency toward ultimate anti-alignment ($m = 0$). Therefore, we also checked the stability of anti-alignment in pairs which start from such a state. Fig. 2.6(d) examines the stability of this configuration for objects initially confined to the xy plane (perpendicular to the force). Whereas the aligned pair (blue/dotted curve) is unstable, the anti-aligned one (red/dashed curve) remains stable for the duration of integration. It may well be that this stability survives for a long but finite time, see e.g., dark red/dotted curve in Fig. 2.6(c). In addition, a separation of the pair along the z-axis destabilizes an anti-aligned pair as well (examples not shown). Fi-

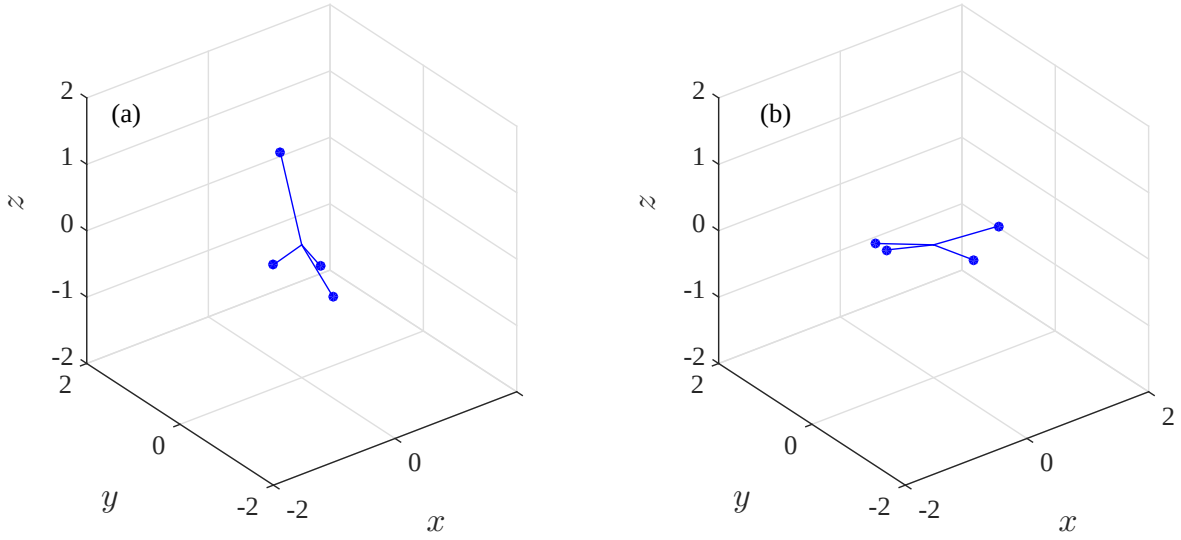

Figure 2.2: Two examples of randomly generated self-aligning stokeslet objects, which were used in the simulations. The objects comprise four stokeslets connected by dragless rods. The origin of the objects is at point (0,0,0) and the aligning direction is $-\hat{\mathbf{z}}$. The object on the left corresponds to the dark red/dotted trajectories in the left panels of Fig. 2.5 and Fig. 2.6, and the one on the right corresponds to the purple/dashed trajectories in the right panels of Fig. 2.3 and Fig. 2.4.

nally, we note that even if the final phase difference were arbitrary and uniformly distributed, the value of m would be evenly distributed around $1/2$ but non-uniformly, with larger weights on $m = 0, 1$. (This follows from the definition of m, see Eq. (2.21).)

Fig. 2.8 compares results obtained using the full pair-mobility matrix of the stokeslet objects with those obtained from the multipole (dipole) approximation. As expected, the two calculations agree for objects whose mutual distance increases with time, and disagree for objects whose trajectories reach close proximity.

2.5 Discussion

Irregular objects display rich dynamics already at the level of a pair of objects, as has been demonstrated above. In the present Chapter we have focused on the effect of the HI on the orientational alignment of such object pairs.

The HI, in general, degrades the alignment. We have rigorously proven the instantaneous linear degradation for fully aligned objects at large mutual distances. In other circumstances, such as nearby or unaligned objects, the HI may have an opposite effect. The leading degradation effect in distance is dipolar rather than monopolar; yet, it is significant — a large mutual distance (compared to the object size) is required to make the degradation negligible. More quantitatively, the degradation will be significant when the perturbation to the angular veloc-

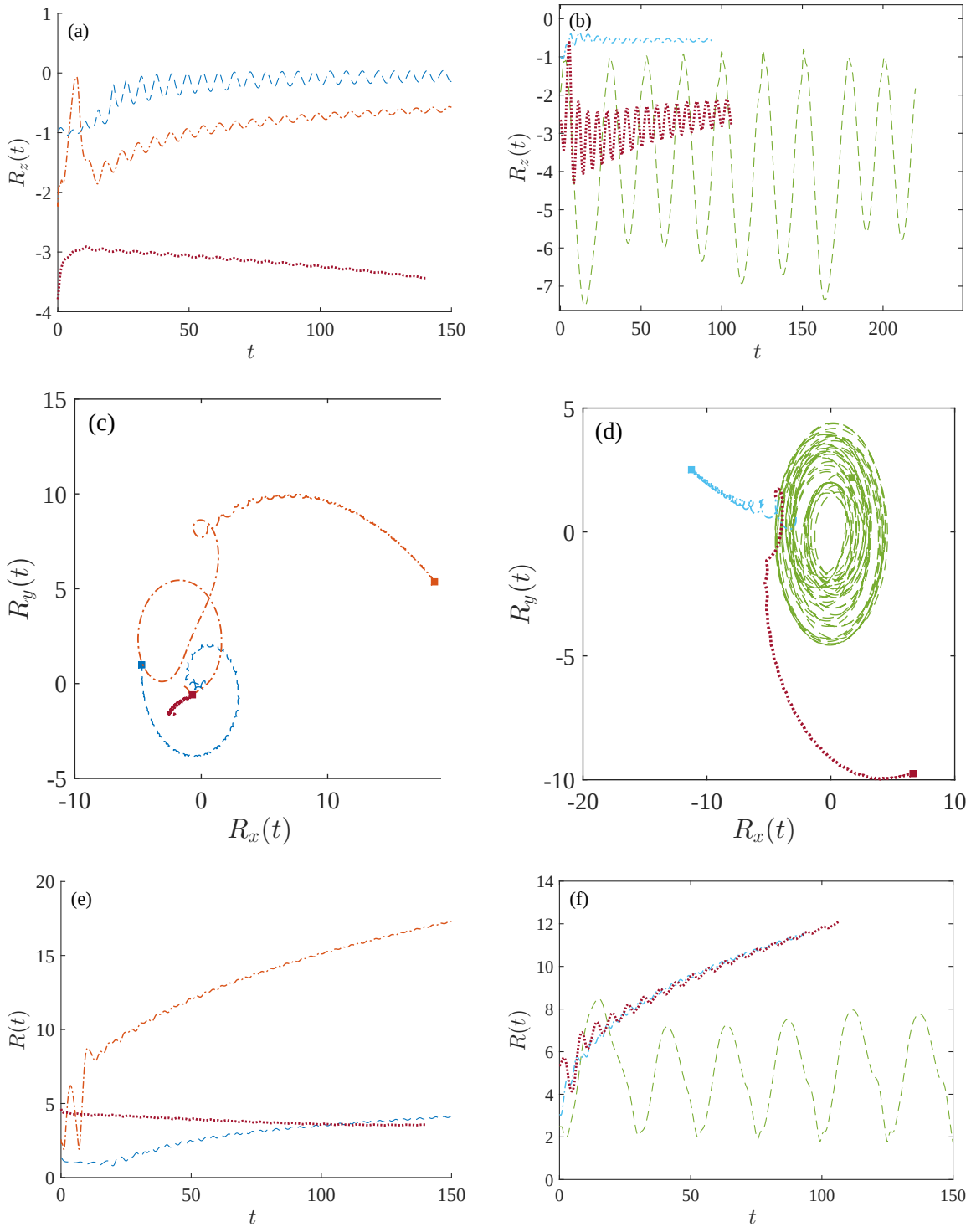

Figure 2.3: Trajectories of the separation vector between the object's origins, $\mathbf{R}(t)$, under time-dependent forcing. The three rows, from top to bottom, correspond, respectively, to the separation along the z direction, its projection onto the xy plane, and its total magnitude. The squares in the middle row indicate the state at the end of the simulation. The panels show results for three different objects indicated by different line styles and colors. The pairs of objects start from either a random mutual orientation (left column) or their fully aligned state (right column). The green/dashed trajectory on the right panels was integrated longer than 150 time units to verify that it continues in a limit cycle.

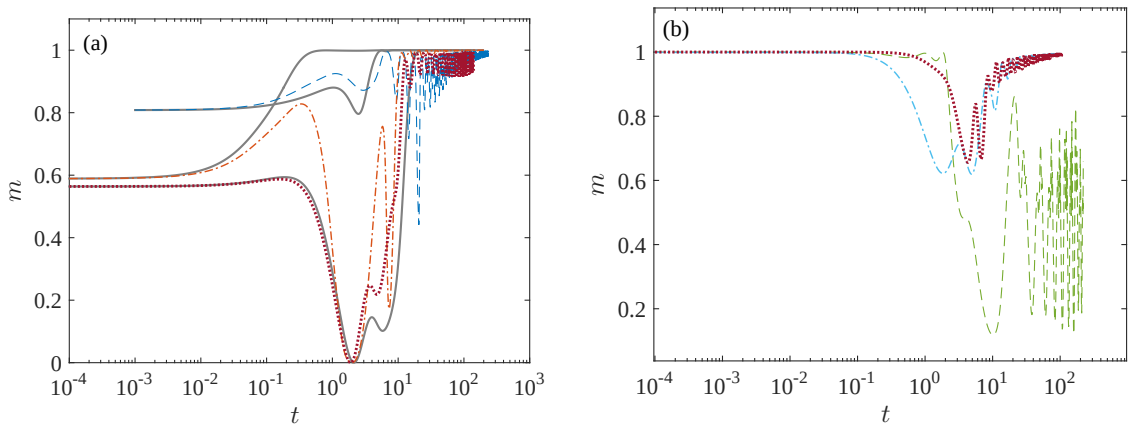

Figure 2.4: Alignment order parameter, $m(t)$ (defined in Eq. (2.21)), as a function of time, under time-dependent forcing, for the examples of Fig. 2.3. (a) Results for random initial orientations, $0 < m(t = 0) < 1$ (examples on the left column of Fig. 2.3); the additional solid gray curves correspond to non-interacting objects. (b) Results for initially fully aligned object pairs, $m(t = 0) = 1$ (right column in Fig. 2.3).

ity due to HI, $\delta\omega$, becomes comparable to the inverse of the time required to align a single object. The unperturbed angular velocity is given by $\omega_0 = \lambda_3 F$. The dimensionless eigenvalue of the self-twist matrix is generally found to be about an order of magnitude smaller than the dimensionless self-mobility coefficient [2, 46, 47], i.e., $\omega_0 \sim 0.1F/(8\pi\ell^2)$. As presented in Sec. 2.1.2, $\delta\omega \sim \mathbb{T}^{ab}F \sim F/(8\pi\ell^2)(\ell/R)^2$. The alignment time is typically $t_{\text{align}} \sim 10/\omega_0$ (see Fig. 2.4). Hence, the degree of degradation is $t_{\text{align}}\delta\omega \sim 10^2(\ell/R)^2$. The conclusion is that the separation between the objects should be larger than ten times their size to maintain alignment. In the case of many objects this implies a maximum volume fraction $(\ell/R)^3 \sim 10^{-3}$.

At the same time, as shown in Sec. 2.4, for most of our randomly generated pairs of objects, the HI makes the rotating objects repel each other. As a result, at long times the HI usually becomes negligible and each of the objects gets aligned again with the time-dependent force. As will be explained in Chapter 3, this repulsion is related to the mutual rotation of the two objects which causes them to glide away from each other. In fact, the objects need not be irregular to exhibit this gliding effect; two forced spheroids which start parallel to one another will experience the same repulsion [60, 124, 130]. (However, as will be shown in the next Chapter, the dynamics resulting from the gliding effect is different for self-aligning objects compared to spheroids.) For the case of a finite number of objects the repulsion will help restore the alignment as the objects drift apart. It should be kept in mind, however, that the repulsion is not a general law. We observed it for a few dozens pairs of stokeslet objects. Yet, a few counter-examples have been also provided in Sec. 2.4.

An interesting counterpart of the effects discussed here is found in the interaction between a forced object and a nearby wall [32, 131]. The wall can be represented by an image (though not identical) object forced in the *opposite* direction [28]. As a result, the object will rotate and, if it is non-spherical, also glide *toward* or away from the wall, as was indeed shown for a rod

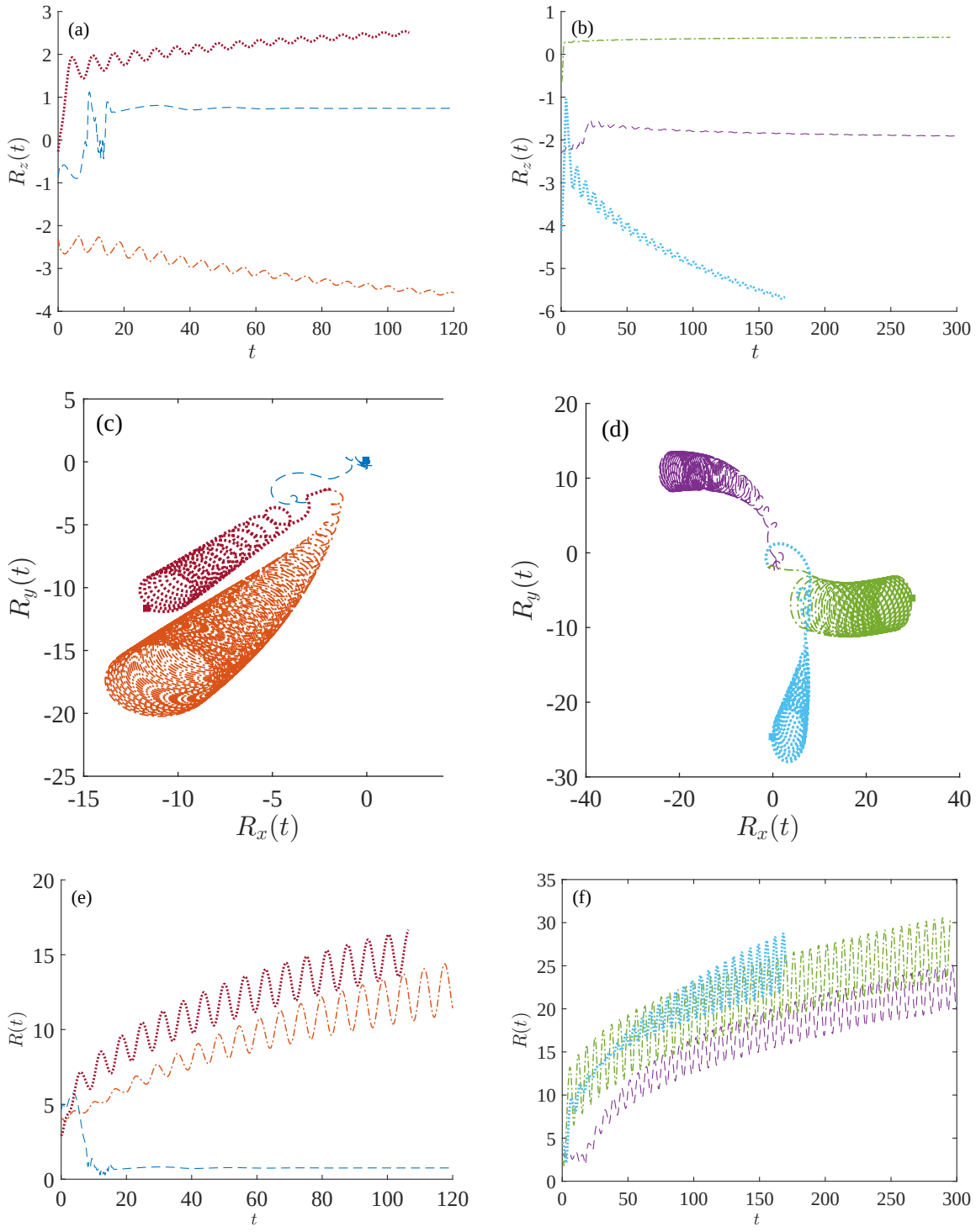

Figure 2.5: Trajectories of the separation vector between the objects' origins, $\mathbf{R}(t)$, under constant forcing. The meaning of the various panels are the same as in Fig. 2.3. In all the examples shown here, the two objects repel each other except for the example which corresponds to the blue/dashed curve in the left panels. (The repulsive trajectories were actually integrated to times longer than presented here.)

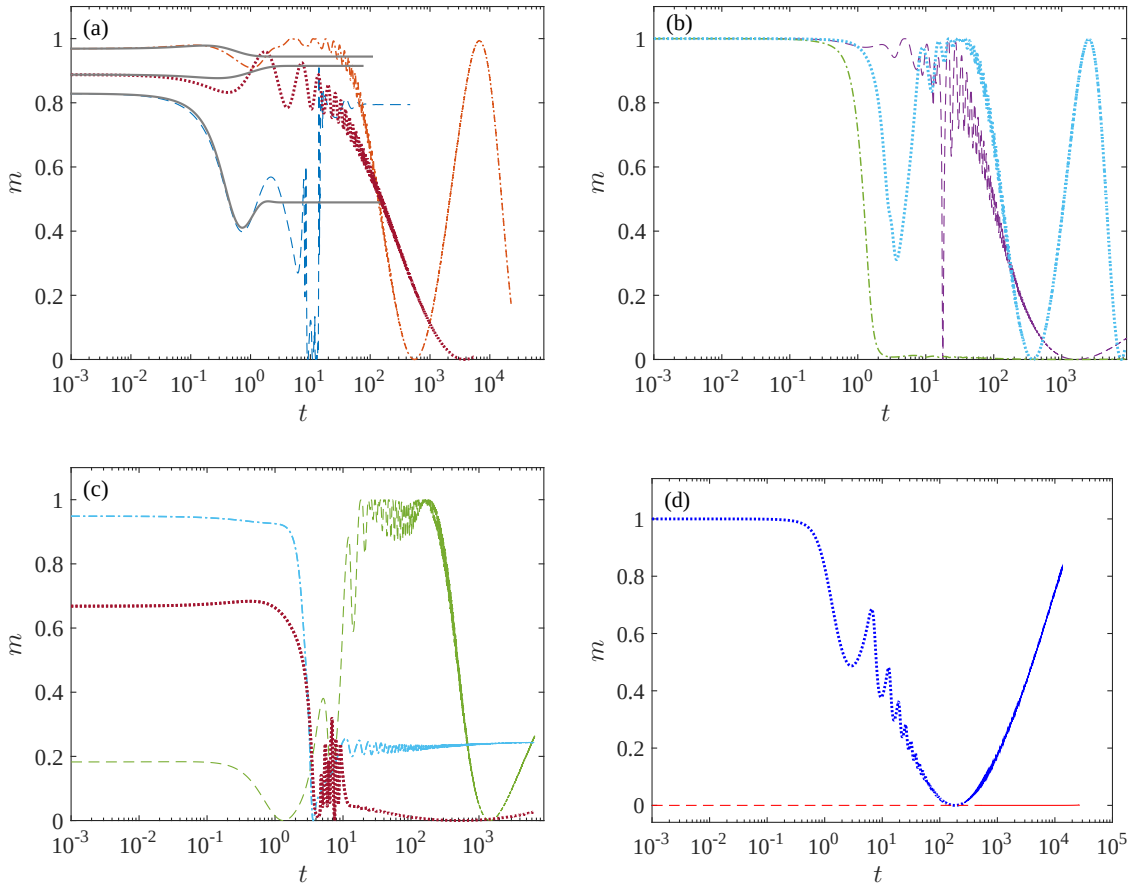

Figure 2.6: Orientation order parameter, $m(t)$ (defined in Eq. (2.21)), as a function of time, under constant forcing, for the examples of Fig. 2.5. (a) Results for random initial orientations, $0 < m(t=0) < 1$ (examples on the left column of Fig. 2.5); the solid gray curves correspond to non-interacting objects. (b) Results for initially fully aligned object pairs, $m(t=0) = 1$ (right column in Fig. 2.3). (c) Results for objects with initial partial alignment, $m(t=0) = \cos^2(\Delta\zeta/2)$, (rotating around the same axis with random initial phases $\Delta\zeta$). (d) The stability of anti-alignment; shown are trajectories of two identical pairs, which start on the xy plane from the same separation and axes of rotation but with different relative phases. Blue/dotted and red/dashed curves represent, respectively, a pair which starts aligned (zero relative phase, $m(t=0) = 1$) and one which starts anti-aligned (relative phase of π, $m(t=0) = 0$).

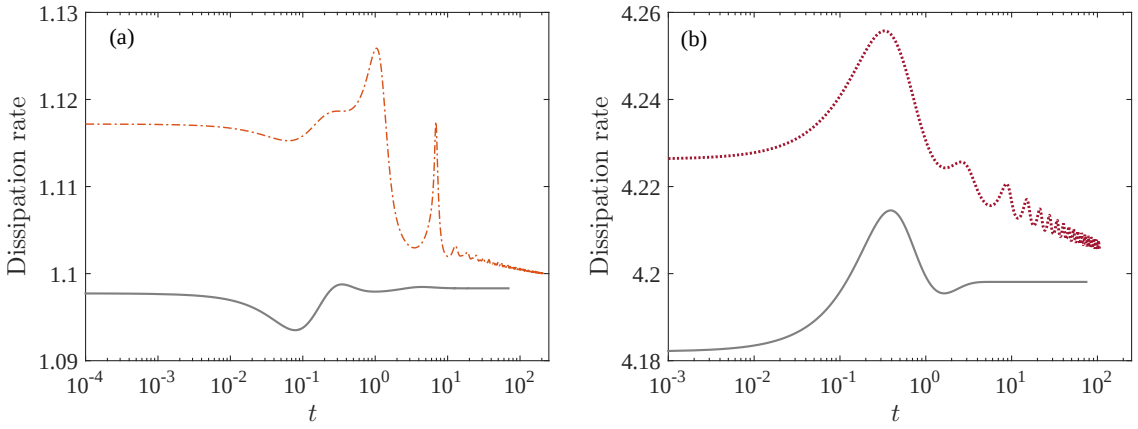

Figure 2.7: Dissipation rate (defined in Eq. (2.22)) as a function of time for object pairs starting from arbitrary orientations, under time-dependent forcing (a) and constant forcing (b). Dash-dotted and dotted colored curves correspond to the examples of the same styles/colors in the preceding figures. Solid curves show the results in the absence of hydrodynamic interactions.

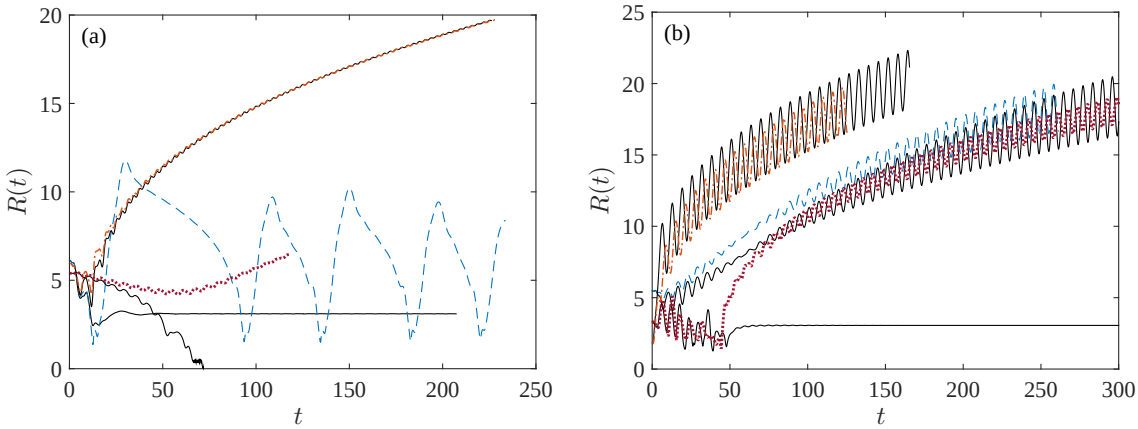

Figure 2.8: Comparison between the evolution of pair separations, $R(t)$, obtained using the full pair-mobility matrix (dashed, dotted and dash-dotted colored curves) and its multipole approximation (solid curves). Each panel presents three examples of pairs under time-dependent (a) and constant (b) forcing. All pairs start from a fully aligned state. The multipole approximation includes the monopolar and dipolar terms.

falling near a wall [131]. Obviously, the interaction of a self-aligning object with a wall will also degrade the alignment.

This Chapter shows that asymmetry in sedimenting objects leads to a wealth of hydrodynamic interaction effects not seen for spheres. This study was undertaken to assess how interactions disrupt the rotational synchronization of such objects. However, it proves to have striking effects independent of this alignment. The prevalent repulsion, the occasional entrapment and the intricate quasiperiodic motions shown above are examples. These effects could have significant impacts on real colloidal dispersions, e.g., in fluidized beds of catalyst objects, as will be demonstrated in Chapter 4.

The two key results of this Chapter— instantaneous relative motion and typical repulsion at long-times— lead us to the next Chapter where we show, by further general treatment of the pair HI, that many of the effects we have found above apply more generally.

Chapter 3

Hydrodynamic Interactions between Two Forced Objects of Arbitrary Shape: Relative Translation[1]

In Chapter 2, we have studied general properties of the hydrodynamic interaction and considered its effect on orientational dynamics. In the present Chapter we extend this study, focusing on translational motion of object pairs.

It is well known that in the case of two identical sedimenting spheres, isolated in an unbounded fluid, the hydrodynamic interaction at zero Reynolds number does not produce relative translation (see Sec. 1.5). This rule is readily violated by changing the system's geometry. Previous studies of apparent interactions (pseudopotentials) originating in hydrodynamic coupling treated specific experimental scenarios [64, 66, 69]. In this Chapter we address two additional general questions: (*i*) At zero Reynolds number, what are the geometrical configurations for which relative translation between two objects necessarily vanishes? (*ii*) In cases where it does not vanish, what are the consequences for the long-time trajectories of the two objects? Looking for properties of general applicability, we consider arbitrarily shaped objects and do not restrict ourselves to a specific geometry.

Here we extend the analysis of Chapter 2 along two separate directions: (a) In Sec. 3.1 we continue to study the instantaneous response of object pairs, i.e., the rigorous properties of the pair-mobility matrix. We provide examples for configurations with spatial inversion symmetry, where the relative translation vanishes, as well as simple geometries, for which this symmetry is broken. (b) In Sec. 3.2 we return to examine in more detail the repulsive trend in the far-field time evolution of self-aligning object pairs, providing an intuitive explanation

[1] The material presented in this Chapter was published in T. Goldfriend, H. Diamant, and T. A. Witten, Phys. Rev. E. **93**, 042609 (2016) [132].

of the phenomenon. We further compare it to the time evolution of two non-alignable objects (uniform prolate spheroids), and point out the qualitative difference between the two cases.

3.1 Instantaneous Response: Symmetrical Pair Configurations

In this Chapter we focus on the translational dynamics of two forced objects (without external torques), which is captured by a 6×6 sub-matrix of the pair-mobility in Eq. (2.1), indicated hereafter by $\mathbb{A}$,

$$\begin{pmatrix} \mathbf{V}^a \\ \mathbf{V}^b \end{pmatrix} = \begin{pmatrix} \mathbb{A}^{aa} & \mathbb{A}^{ab} \\ \mathbb{A}^{ba} & \mathbb{A}^{bb} \end{pmatrix} \begin{pmatrix} \mathbf{F}^a \\ \mathbf{F}^b \end{pmatrix}. \tag{3.1}$$

The properties of the full pair-mobility matrix in Eq. (2.1) imply that $\mathbb{A}$ is positive definite and symmetric [31–33]. Next, we discuss additional symmetries of the matrix $\mathbb{A}$.

As a first step, we consider the transformation of the pair-mobility matrix under various operations— spatial proper and improper rotations (rotations combined with reflections), and exchange of objects. We note that the positions of the objects' origins, i.e., the external forcing points, are an essential part of the system geometry. In this section we will restrict our treatment to cases where the forcing point is at the geometric centroid of the object, that is, the center of mass if the object has a uniform mass density. Consider the transformation between two pair-mobility matrices which differ by a rigid rotation. Given the rotation matrix $\mathbb{R}$ between a given configuration and the rotated one, the blocks in $\mathbb{A}$, being all tensors, transform accordingly: $\mathbb{A}^{aa} \to \mathbb{R}\mathbb{A}^{aa}\mathbb{R}^T$, $\mathbb{A}^{ab} \to \mathbb{R}\mathbb{A}^{ab}\mathbb{R}^T$ and $\mathbb{A}^{bb} \to \mathbb{R}\mathbb{A}^{bb}\mathbb{R}^T$. The same law applies to the transformation between systems which differ by a rigid improper rotation with improper rotation matrix $\bar{\mathbb{R}}$. We note here that the twist matrices $\mathbb{T}$, the blocks in Eq. (2.1) which relate forces to angular velocities, are pseudo-tensors; thus, their transformation under improper rotation includes a change of sign, $\mathbb{T}^{aa} \to -\bar{\mathbb{R}}\mathbb{T}^{aa}\bar{\mathbb{R}}^T$. Since the pair-mobility matrix inherently refers to two distinguishable objects, a and b, we should also consider its transformation under interchanging the objects' labeling, $a \leftrightarrow b$. This transformation corresponds to interchanging the blocks $\mathbb{A}^{aa} \leftrightarrow \mathbb{A}^{bb}$ and $\mathbb{A}^{ab} \leftrightarrow \mathbb{A}^{ba}$; or, in matrix form,

$$\mathbb{A} \to \mathbb{E}\mathbb{A}\mathbb{E}^{-1}, \tag{3.2}$$

where $\mathbb{E}$ is the 6×6 matrix

$$\mathbb{E} = \begin{pmatrix} 0 & \mathbb{I}_{3\times 3} \\ \mathbb{I}_{3\times 3} & 0 \end{pmatrix}. \tag{3.3}$$

(in analogy to Eq. (2.3).)

As mentioned above, at zero Reynolds number, sedimentation of two identical rigid spheres in an unbounded fluid does not induce relative motion of the two spheres. In contrast, we showed in Chapter 2 that two identical, arbitrarily shaped objects in an unbounded fluid, un-

der the same forcing, may attract or repel each other. In addition, using the symmetry of such a system under exchange of objects, we found the leading (dipolar) order of this effective interaction at large mutual separation. We now examine the HI for several symmetric configurations. In this part of the Chapter we focus on what symmetry has to tell us, and do not yet anticipate when its consequences are useful. To demonstrate the resulting principles, therefore, we allow ourselves to examine specially designed configurations. Examples for the usefulness of these principles will be given later on.

3.1.1 Two Enantiomers in an Unbounded Fluid

As the first example, we examine a system possessing inversion symmetry. The spatial inversion of the Stokes equations under reversing time has been shown to imply fundamental consequences concerning the dynamics of rigid objects. For example, it was used previously to deduce generic properties of shear flow response, in the cases of a single spheroid [133] and an enantiomeric non-interacting pair [17]. The fact that the instantaneous response, under the same forcing, of pair-configurations with spatial inversion symmetry does not induce relative translation may have already been given elsewhere; yet, we are not aware of works which give a rigorous derivation of it. Accordingly, we review this basic result below from matrix transformations and time-reversibility points of view.

Consider a system of two enantiomers in an unbounded fluid as depicted in the left panel of Fig. 3.1. We choose the mutual orientation of the objects such that one object is the mirror image of the other; hence, the system's geometry is invariant under spatial inversion, $\mathbf{r} \to -\mathbf{r}$. This symmetry implies that the pair-mobility matrix is invariant under two consecutive operations (see Fig. 3.1): spatial inversion followed by exchange of objects' labels, or, in matrix form, $\mathbb{A} = \mathbb{E}(-\mathbb{I}_{6\times 6})\mathbb{A}(-\mathbb{I}_{6\times 6})\mathbb{E}^{-1}$, where $\mathbb{E}$ has been defined in Eq. (3.3). This last equality yields $\mathbb{A}^{aa} = \mathbb{A}^{bb} = \mathbb{A}^{\text{self}}$ and $\mathbb{A}^{ab} = \mathbb{A}^{ba} = \mathbb{A}^{\text{coupling}}$, i.e.,

$$\text{Enantiomeric pair:}\quad \mathbb{A} = \begin{pmatrix} \mathbb{A}^{\text{self}} & \mathbb{A}^{\text{coupling}} \\ \mathbb{A}^{\text{coupling}} & \mathbb{A}^{\text{self}} \end{pmatrix}, \tag{3.4}$$

which applies in fact for any inversion-symmetric situation. This form of the pair-mobility matrix implies that, under the same force $\mathbf{F}$, the two objects will develop identical velocities, $\mathbf{V}^a = \mathbf{V}^b = (\mathbb{A}^{\text{self}} + \mathbb{A}^{\text{coupling}}) \cdot \mathbf{F}$. Thus: the *instantaneous* response under the *same forcing* of a pair, whose configuration possesses an inversion symmetry, does not include relative translation. As noted above, a system of two sedimenting spheres is a particular example of this general result.

The vanishing relative motion in a system which is invariant under spatial inversion can be understood alternatively by the following argument. Assume by negation that two enantiomers in an unbounded fluid develop a relative velocity under the same forcing. Without loss of generality, let us take the case when the two objects get closer together; see configuration

(a) in the right panel of Fig. 3.1. The mirror configuration of the system ($\mathbf{r} \to -\mathbf{r}$), depicted in configuration (b), implies that the two also get closer when reversing the forces. On the other hand, Stokes equations are invariant under inversion of time and forces; hence, reversing the forces in configuration (a) should make the objects get further apart, as depicted in configuration (c). Since (b) and (c) represent the same system, we reach a contradiction, and deduce that the relative velocity between the two enantiomers must vanish.

To summarize, it is inversion symmetry that governs the vanishing relative velocity between two forced objects at zero Reynolds number; hence, whenever this symmetry is broken one should expect relative translation.

An important remark bears mentioning here. The instantaneous rotational response of the enantiomeric pair corresponds to two *opposite rotations*, i.e., non-vanishing relative angular velocity. (See Chapter 2.) With time, the opposite rotations will break the inversion symmetry, unless there are additional symmetries, for example, when the objects' shapes are isotropic, as in the case of two spheres. While the example of two enantiomers whose mutual symmetry is only instantaneous may seem artificial, the principle that it demonstrates is useful. Driving forces will sometimes bring bodies close to a symmetric situation, and then one will find especially simple motions that call for explanation. In particular, two irregular objects can be aligned by the driving [34, 46, 47] (e.g., the self-aligning objects) and then we should be interested in the question of whether they keep their distance or drift apart. Moreover, not only a pair of spheres will preserve inversion symmetry over time. Another example is two spheroids, or indeed a pair of any bodies of revolution with fore-aft symmetry, whose axes are aligned on a plane perpendicular to the force; see Fig. 3.2(a). Without any calculation, we can assert that such two objects will maintain their relative position over time. The additional symmetry of the system imposes relative rotation only about the axes of symmetry (y-axis in Fig. 3.2(a)), which does not break the inversion symmetry. Another example will be given in the Discussion of this Chapter.

3.1.2 Configurations with One Reflection Plane and Exchange Symmetry

We now turn to examples where the symmetry is broken by the confining boundaries. The first system consists of two spheres, placed on a plane parallel to a wall; see Fig. 3.2(b). This system was used in Ref. [64] to interpret the attraction between two like-charged spheres near a similarly charged wall, as was observed in optical-tweezers experiments [65]. The geometry of the system is invariant under two successive operations: reflection about the symmetry plane of the two spheres and interchanging the objects. We denote by $\parallel$ and $\perp$ the directions parallel and perpendicular, respectively, to the mirror plane, i.e., perpendicular and parallel, respectively, to the wall itself. The reflection leaves vectors parallel to the mirror plane unchanged but reverses vectors normal to that plane. Using the transformation laws introduced above, we find that the blocks of $\mathbb{A}$, which relate forces perpendicular to the wall and objects' velocities

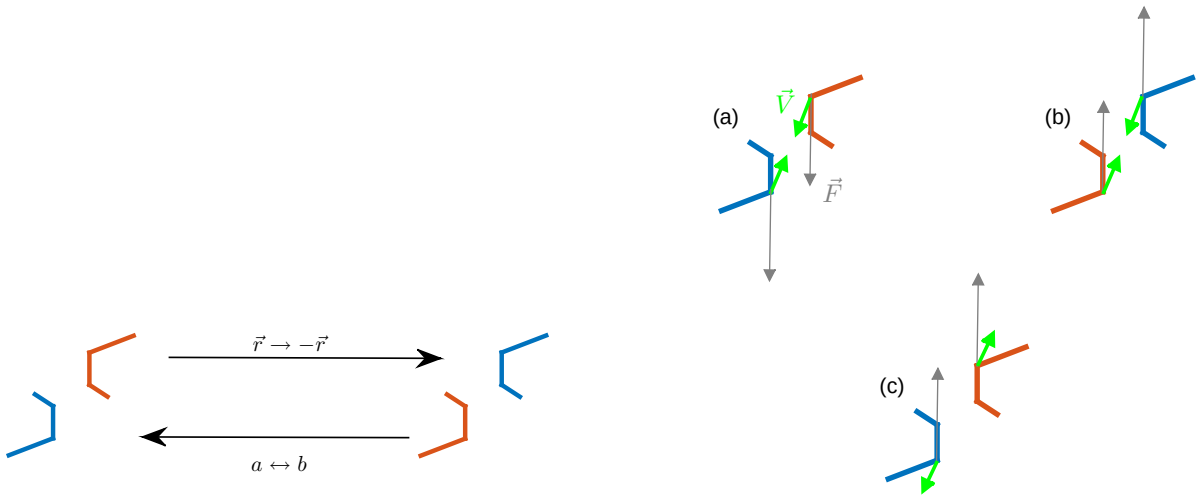

Figure 3.1: Schematic description of the arguments presented in Sec. 3.1.1 for the vanishing instantaneous relative motion between two forced enantiomers. The left panel describes how the mirror symmetry of the system is expressed in terms of spatial inversion combined with interchanging the objects. The right panel demonstrates the arguments based on the symmetry of the Stokes equations under inversion of time and forces, where gray (thin) and green (thick) arrows indicate forces and velocities respectively. Configuration (b) is the spatial inversion of configuration (a) whereas configuration (c) is the response of configuration (a) under the opposite forcing.

parallel to the wall, must satisfy $\mathbb{A}^{aa}_{\perp\parallel} = -\mathbb{A}^{bb}_{\perp\parallel}$ and $\mathbb{A}^{ab}_{\perp\parallel} = -\mathbb{A}^{ba}_{\perp\parallel}$. These restrictions imply that, under forcing toward or away from the wall (e.g., as the spheres are electrostatically repelled from the wall [65]), the objects respond in opposite directions in the plane parallel to the wall, $\mathbf{V}^a_\perp = (\mathbb{A}^{aa}_{\perp\parallel} + \mathbb{A}^{ab}_{\perp\parallel})F_\parallel = -\mathbf{V}^b_\perp$. Note that the symmetry of the system alone does not tell us whether the objects repel or attract under a given forcing direction. The analysis in Ref. [64] showed that forcing away from the wall results in an apparent attraction between the pair, in agreement with the experiment. This can also be deduced from the right panel of Fig. 1.1 that shows the flow lines generated by a stokeslet near a wall. It should be stressed that, unlike specific calculations as in Ref. [64], our symmetry principle is neither restricted to spheres, nor to the limit of small objects, nor to the limit of large separations.

The complete form of the pair-mobility matrix as a result of the geometrical restrictions in this system is given in Appendix A.4, Eq. (A.4), along with the explicit expressions for point objects. Another interesting conclusion, arising solely from the system's symmetry, is that, since $\mathbb{A}^{aa}_{\perp\parallel} = -\mathbb{A}^{bb}_{\perp\parallel}$ and $\mathbb{A}^{ab}_{\perp\parallel} = -\mathbb{A}^{ba}_{\perp\parallel}$, forcing the spheres *parallel* to the wall will result in one sphere approaching the wall and the other moving away from it.

As a second example, let us consider the system addressed in Ref. [66] — two spheres forced to move along a ring; see Fig. 3.2(c). The corresponding pair-mobility matrix can be written in polar coordinates (ρ, θ). The system is invariant under two successive operations: inversion of the θ coordinate, $\theta \to -\theta$, and interchanging the objects. Hence, this system is similar to the previous one in the sense that it is symmetric under objects exchange by inversion of one coordinate. This leads to $\mathbb{A}^{aa}_{\rho\theta} = -\mathbb{A}^{bb}_{\rho\theta}$ and $\mathbb{A}^{ab}_{\rho\theta} = -\mathbb{A}^{ba}_{\rho\theta}$. Consequently, under the same

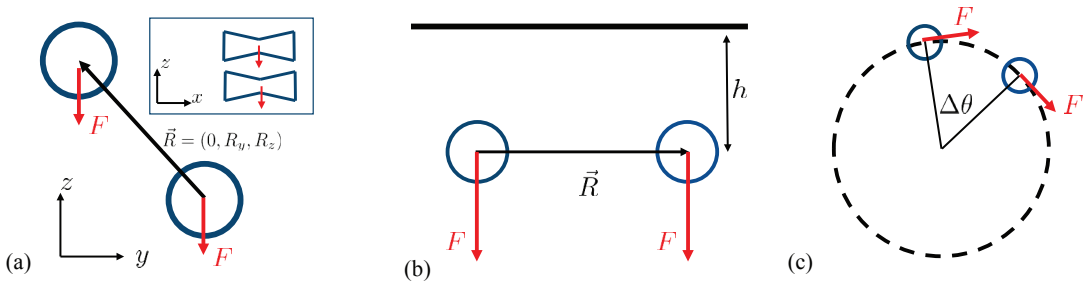

Figure 3.2: The three systems discussed in Sec. 3.1.1 and Sec. 3.1.2: (a) Two identical axisymmetric objects, with fore-aft symmetry, where the vector connecting their origins is perpendicular to their symmetry axes. (b) A pair of spheres near a wall. The spatial separation between the spheres is represented by the vector **R** which connects their origins. (c) A pair of spheres driven along a ring. The angular separation is indicated by $\Delta\theta$.

forcing along the tangential direction, the spheres respond with opposite velocities along the radial direction. Sokolov et al. used a holographic optical vortex trap to study this system and observed the radial symmetry breaking experimentally [66]. In addition, they found that this effect, combined with a confining radial potential, results in overall attraction along the ring as the system evolves in time. Once again, the symmetry argument derived here is far more general than the specific limit studied theoretically in Ref. [66].

We note that the results obtained above, regarding configurations with one reflection plane of symmetry, should also be derivable using time-reversal arguments, as was done in the case of an enantiomeric pair.

3.2 Far-Field Dynamics of two Forced Objects in Unbounded Fluid

In the preceding section we considered the instantaneous response of a pair of objects given the symmetries of their configuration. The analysis of this linear problem, derived from symmetry arguments, is useful to determine the stability of a given state of the system. However, it might be inapplicable to the time-dependent trajectories, since a configuration symmetry at a given time can be broken by subsequent motion. A well known example is the sedimentation in an unbounded fluid of two prolate spheroids, which start with their major axes parallel to the force [57, 59, 124]. The initial inversion symmetry about the plane perpendicular to the force, which, according to the discussion in Sec. 3.1, precludes any relative translation, soon breaks due to the rotation of each spheroid, and relative velocity appears (see a more detailed analysis below). In general, since the instantaneous response depends on configuration, the time-dependent trajectories of a driven pair is a non-linear, multi-variable problem. We are compelled, therefore, to implement numerical integration for specific examples, and try to identify general trends. In this section we consider the time evolution of two objects under the same constant driving. In particular, we provide further insight into the results reported in Chapter 2 concerning the combined effects of rotational and translational interactions.

3.2.1 Dynamics of an Isolated Object

Before describing the time evolution of object pairs, it is essential to introduce the different types of objects that we consider hereafter and mention their dynamics, under a unidirectional force, at the single-object level, following the discussion in Sec. 1.4. In the absence of external torque, the linear and angular velocities of an object are given, respectively, by $\mathbb{A}_{(0)} \cdot \mathbf{F}$ and $\mathbb{T}_{(0)} \cdot \mathbf{F}$, where $\mathbb{A}_{(0)}$ and $\mathbb{T}_{(0)}$ are 3×3 blocks of the object's self-mobility matrix. These blocks depend on the shape of the object, its orientation, and the position of the forcing point.

We consider three types of objects: (a) *Uniform prolate spheroid* — a spheroid whose forcing point is located at its geometric centroid, as in the case of spheroids with a uniform mass density; see left panel of Fig. 1.2. This is a regular object (i.e., whose $\mathbb{T}_{(0)} = 0$) which does not rotate under force, regardless of its orientation. The translation direction of a uniform spheroid is in the plane spanned by its major axis and the forcing direction [32]. (b) *Self-aligning prolate spheroid* — a prolate spheroid whose forcing point is displaced from the centroid along its major principal axis, e.g., spheroids with a non-uniform mass density. These objects have an antisymmetric $\mathbb{T}_{(0)}$ matrix, that is, the only real eigenvalue of the self-twist matrix, λ_3, is zero. For any initial orientation, a self-aligning spheroid rotates toward a state where its major axis, and therefore its translation direction, is aligned with the external force. We use type (b) as a simple example, which can be treated analytically, for self-aligning objects. (c) *Self-aligning object of irregular shape* — an object whose $\mathbb{T}_{(0)}$ matrix has only one real, non-zero eigenvalue. These objects reach an ultimate alignment with the force direction, together with a uniform right- or left-handed rotation about it [34, 46, 47]. As in Chapter 2 we use the particularly simple construction of stokeslet objects that are constructed randomly, and thus we avoid objects of pre-designed shapes.

3.2.2 Far-Field Equations

As in the preceding parts, let us assume that there are no external torques on the objects, such that we can choose their origins as their forcing points. We consider the case in which the objects are subjected to the same forcing $\mathbf{F}$. The mutual separation between the objects a and b is designated with the vector $\mathbf{R}$, whose direction is defined from the origin of a to the origin of b. While time-integrating the equations it is essential to take into account the coupling between translation and rotation. Thus, we must work with the complete pair-mobility matrix, Eq. (2.1), which gives

$$\dot{\mathbf{R}} = \mathbf{V}^a - \mathbf{V}^b = \left(\mathbb{A}^{aa} + \mathbb{A}^{ab} - \mathbb{A}^{bb} - \mathbb{A}^{ba}\right) \cdot \mathbf{F} \tag{3.5}$$

$$\boldsymbol{\omega}^a = \left(\mathbb{T}^{aa} + \mathbb{T}^{ab}\right) \cdot \mathbf{F} \tag{3.6}$$

$$\boldsymbol{\omega}^b = \left(\mathbb{T}^{bb} + \mathbb{T}^{ba}\right) \cdot \mathbf{F}. \tag{3.7}$$

A major simplification, from both the analytical and the numerical points of view, is to consider pairs with separation much larger than the typical size of the individual object ℓ, and study the corresponding far-field interaction. In this case we can utilize the general form of the pair-mobility matrix up to second order in ℓ/R, which has been derived in Chapter 2. Following Eq. (2.12), the equations governing the objects' mutual separation and their rotations read

$$\dot{\mathbf{R}} = \left[(\mathbb{A}^a_{(0)} - \mathbb{A}^b_{(0)}) + (\Pi^a + \Pi^b) : \boldsymbol{\nabla}\mathbb{G}(\mathbf{R}) - \boldsymbol{\nabla}\mathbb{G}(\mathbf{R})^T : (\Pi^a + \Pi^b)^T\right] \cdot \mathbf{F} \tag{3.8}$$

$$\boldsymbol{\omega}^a = \left[\mathbb{T}^a_{(0)} + (\Psi^a - \frac{1}{2}\epsilon) : \boldsymbol{\nabla}\mathbb{G}(\mathbf{R})\right] \cdot \mathbf{F} \tag{3.9}$$

$$\boldsymbol{\omega}^b = \left[\mathbb{T}^b_{(0)} - (\Psi^b - \frac{1}{2}\epsilon) : \boldsymbol{\nabla}\mathbb{G}(\mathbf{R})\right] \cdot \mathbf{F}, \tag{3.10}$$

where $\mathbb{A}_{(0)}$, $\mathbb{T}_{(0)}$ and Π, Ψ are single-object-dependent tensors of rank 2 and 3, respectively, which depend on the individual object's shape and orientation, ϵ is the Levi-Civita tensor, and the : sign denotes contraction over two indices. Here we separate the tensor Φ introduced in Chapter 2 into its translational part, Π, and rotational part, $\Psi - \frac{1}{2}\epsilon$, each with dimensions $3 \times 3 \times 3$. Such separation can be inferred by the analysis in Appendix B. The tensors $\mathbb{A}_{(0)}$ and $\mathbb{T}_{(0)}$ are the zeroth order blocks, which give the linear and angular velocities of a single object when it is subjected to external force. The tensors Π and Ψ correspond to the linear- and angular-velocity responses to a flow gradient at the object's origin. When these tensors are coupled with $\boldsymbol{\nabla}\mathbb{G}$ they construct second-order terms of the pair-mobility matrix, describing the direct HI between the objects. The term which is proportional to ϵ is also a part of the second-order term, giving the rotation of one object with the vorticity generated by forcing the other.

3.2.3 Transversal Repulsion under Constant Forcing

In Chapter 2 we examined the effect of HIs on the orientational evolution of two identical, self-aligning objects. Using numerical integration we followed the time-dependent trajectories of pairs of stokeslet objects under two types of driving— a constant force and a rotating one. We noticed that in most (though not all) of the studied examples the two identical, self-aligning objects effectively repelled each other when subjected to the same driving (see Fig. 2.5 and solid red curve in Fig. 3.4(a)). (Counter-examples, such as limit-cycle trajectories, were observed as well.) The increasing separation is transversal— taking place within the plane perpendicular to the average force direction. Below we explain the nature of this repulsion, focusing on the simpler case of constant forcing.

Two Self-Aligning objects

Let us consider the time evolution of the following system, depicted in Fig. 3.3: two identical self-aligning spheroids, positioned initially along the x-axis, and subjected to a constant force along the $(-\hat{\mathbf{z}})$ direction. Self-aligning spheroids are achieved by separating the center of forcing from their centroids, e.g., through a nonuniform mass density under gravity. The configuration has an inversion symmetry about the yz-plane. It does not have an inversion symmetry about the xy-plane unless the spheroids are aligned along $\hat{\mathbf{z}}$. Thus, according to Sec. 3.1, unless aligned, they are expected to have an instantaneous relative velocity. We denote by θ the angle between the force and the major axis of each spheroid; ℓ indicates the length of the major axis, and h is the displacement of the forcing point from the centroid. See Fig. 3.3 (left panel).

For given h and θ, the individual-object's tensors which appear in Eq. (3.8)–Eq. (3.10) can be found from the known tensors for $h = 0$ and $\theta = 0$ (e.g. Ref. [32]) by a change of origin and rotation transformation. An explicit derivation of these tensors is given in Appendix D.1. According to Sec. 3.2.1, *in the absence* of interactions and $\theta \neq 0$, two uniform prolate spheroids will maintain their relative tilt and glide away from or toward each other with a constant velocity, whereas two self-aligning ones will do the same but with velocity decreasing in time as they get aligned with the force.

In order to examine the effect of HIs we take the initial condition $\theta(t = 0) = 0$, for which relative translation vanishes in their absence. Using the calculated individual-object's tensors for self-aligning spheroids, the equations of motion for the pair in the far-field regime $R \gg \ell$ and $\theta \ll 1$, Eq. (3.8)–Eq. (3.10), are then reduced to the following simple form (recall that we set $\eta\ell = 1$):

$$\dot{R} = \left[\beta\theta + \zeta\left(\frac{\ell}{R}\right)^2\right]\frac{F}{8\pi} \tag{3.11}$$

$$\ell\dot{\theta} = \left[-\alpha\theta + \left(\frac{\ell}{R}\right)^2\right]\frac{F}{8\pi}, \tag{3.12}$$

where the dimensionless parameters β, ζ and α (derivable from the single-object tensors) depend on the spheroid's aspect ratio and h/ℓ. More details on the derivation of the above equations are given in Appendix D.2. Using the conventions of Fig. 3.3, $\beta > 0$ and $\alpha \geq 0$; hence, positive θ implies increasing separation and decreasing tilt. Differentiating Eq. (3.11), and substituting $\dot{\theta}$ from Eq. (3.12), we obtain the equation for the separation alone,

$$\ddot{x} = -(\alpha + 2\zeta x^{-3})\frac{F}{8\pi\ell}\dot{x} + (\beta + \alpha\zeta)x^{-2}\left(\frac{F}{8\pi\ell}\right)^2, \tag{3.13}$$

where we have set $x \equiv R/\ell$.

Let us go back for a moment to Eq. (3.11) and Eq. (3.12). The translational dynamics is dictated by (*i*) opposite mutual glide of one object away from the other (first term on the right hand side of Eq. (3.11)), and (*ii*) direct HI which decays as R^{-2} (second term). (We neglect the higher-order correction of the interaction $\sim \theta R^{-2}$.) The evolution of the tilt angle θ is governed by two competitive effects— the vorticity which increases it (second term on the right-hand side of Eq. (3.12)) and the tendency of the individual spheroid to align with the force (first term). Note that the second term in Eq. (3.12) has the object-independent coefficient of 1. The fact that the effect of direct HI on the angular velocities is independent of the object's shape is specific to configurations in which $\mathbf{R} \perp \mathbf{F}$, regardless the object's geometry[2]. The effect of additional separation along the force direction is discussed at the end of this section.

The dotted blue curves in Fig. 3.4 show an example of a numerical solution of Eq. (3.11)–Eq. (3.12). Initially θ increases linearly due to the vorticity term in Eq. (3.12). After a typical time of $\sim (\alpha F/8\pi\ell)^{-1}$ this increase is suppressed by the alignability of each object, and at $t \to \infty$, the separation increases as $t^{1/3}$ while θ decreases to 0 according to a $t^{-2/3}$ law. These asymptotic laws can easily be inferred analytically from Eq. (3.13). The growth in mutual separation is a combination of a gliding term (β) and an interaction term ($\zeta > 0$). We note, however, that the $t^{1/3}$ law arises from the alignability alone, whereas the direct interaction can only quantitatively affect the dynamics. As seen from Eq. (3.13) in the limit of large x, the equivalent system in classical mechanics is the damped equation $\ddot{x} = -B\dot{x} + Ax^{-2}$. At long times, $t \gg B^{-1}$, acceleration is negligible and we are left with the equation $\dot{x} = (A/B)x^{-2}$ for the velocity. This equation yields the terminal $x \sim t^{1/3}$ law of the dotted blue curve in Fig. 3.4(a).

Next, we consider the repulsive time-dependent trajectories in the more general case of two self-aligning objects of irregular shape. We emphasize that this general case is expected to show a richer behavior; this has been illustrated in Sec. 2.4 of Chapter 2 for stokeslets objects, where, for example, attractive-like behavior was observed as well. The repulsive trend occurs in the majority ($\sim 80\%$) of our several dozens examples comprising randomly constructed 4-stokeslets objects. In addition, in the far-field limit, it is independent of the initial separation along the force direction, as well as the initial mutual orientation. Here, we illustrate how the theoretical result derived for self-aligning spheroids is evident also in the effective repulsion between two self-aligning objects of arbitrary shape.

As already emphasized in Chapter 1 and Chapter 2, self-aligning objects of irregular shape exhibit complex dynamics already on the single-object level, as they acquire ultimate rotation about their eigen-direction. For example, their terminal translation direction is not necessarily constant and might rotate about the forcing direction. Here we consider two identical arbitrarily shaped objects, in which the pair configuration has no spatial symmetry. We fol-

[2]The object-dependent tensor Ψ, which appears in Eq. (3.9) and Eq. (3.10), characterizes the response to a spatially symmetric flow gradient only (see Appendix B). When $\mathbf{R} \perp \mathbf{F}$, the flow gradients created by the force monopole on each object, $\pm\boldsymbol{\nabla}\mathbb{G}(\mathbf{R}) \cdot \mathbf{F}$, are antisymmetric. Thus, the object-dependent terms vanish, and the angular velocities are solely affected by the vorticity $\sim \hat{\mathbf{R}} \times \mathbf{F}/R^2$.

low a slightly different numerical approach than the one utilized in Chapter 2 (see Sec. 2.3.2). The coordinate space describing the pair includes the mutual separation $\mathbf{R}$ and the orientation variables of each object, where we represent the latter with Euler-Rodriguez 4-parameters (Sec. 1.7). The resulting equation of motion for this coordinate space is a set of coupled nonlinear, first-order ODEs, which can be solved with conventional techniques; see Appendix D.2 for details of the integration scheme. The objects are initially separated along the x-axis and aligned with the force (which, as before, is along the negative z-axis). These specific initial conditions are used to emphasize the comparison with the pair of spheroids. As opposed to the spheroid pair, where the eigen-directions rotate only about the y-axis and the separation unit-vector $\hat{\mathbf{R}}$ is fixed to its initial direction $\hat{\mathbf{x}}$, here the former and the latter undergo a complex, 3D rotational motion.

We follow the dynamics of each object's eigen-direction, which is affixed to the body frame and denoted by $-\hat{\mathbf{Z}}$. For each object we define a tilt angle $\cos\theta(t) \equiv \hat{\mathbf{Z}}(t)\cdot\hat{\mathbf{z}}$, and an azimuthal correlation with the separation vector $\cos\phi(t) \equiv -\hat{\mathbf{Z}}_{\perp}(t)\cdot\hat{\mathbf{R}}_{\perp}(t)$. A scheme of the configuration with the relevant variables is depicted in Fig. 3.3 (right panel). The two objects can effectively glide away from each other, in resemblance to the case of two self-aligning spheroids, if the eigen-directions are tilted away from the separation direction, that is, $\cos\phi^a(t) = 1$ and $\cos\phi^b(t) = -1$; see inset in the right panel of Fig. 3.3. The solid red curves in Fig. 3.4, which correspond to a representative example, consisting of two identical randomly generated objects, demonstrate that such resemblance between the two cases does exist. In particular, the solid red curve in Fig. 3.4(b) shows that $\theta(t)$ of object a follows the same trend as the dotted blue curve which represents the simple example of self-aligning spheroids. The tilt angle of object b, which is not shown, has a similar behavior. The inset in Fig. 3.4(a) shows the opposite correlations between $\hat{\mathbf{Z}}^a$, $\hat{\mathbf{Z}}^b$ and $\mathbf{R}$. The gliding effect results in an effective repulsion[3], $R(t) \propto t^{1/3}$, as can be seen in Fig. 3.4a.

The example of an arbitrarily shaped, self-aligning pair, presented in Fig. 3.4, is a representative of a half-dozen other examples not shown here. More examples are given in Fig. 2.5—all the repulsive trajectories in that figure follow the $R(t) \sim t^{1/3}$ law. These randomly generated examples correspond to initial conditions, which involve also longitudinal separation and different mutual orientations. The variance in the measured exponents is within a small numerical error, of order 5%. The analytically predicted power law was found to hold for *all* pairs of objects which drifted far apart in the simulations (80% of the examples). This implies that the $1/3$ exponent for the asymptotic repulsion is most probably general for the class of self-aligning objects.

[3]The direct interaction term in Eq. (3.8)— proportional to Π and decaying as R^{-2}— can also contribute to the $t^{1/3}$ trend.

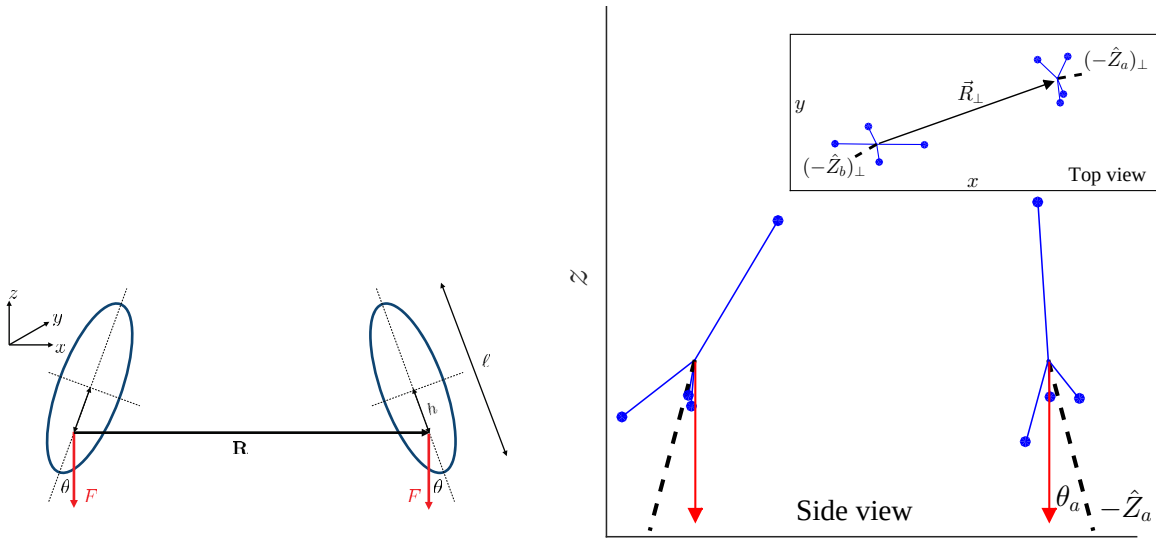

Figure 3.3: Left panel: system of two self-aligning, prolate spheroids. The tilt angle θ is between the force and the major axis of the object, and h indicates the shifted position of the forcing point. Right panel: system of two identical self-aligning objects made of 4 stokeslets. In the absence of interaction the eigen-direction of each object $(-\hat{\mathbf{Z}})$ would eventually align with the force which is along the $(-\hat{\mathbf{z}})$ axis (not drawn), and rotate about it with constant angular velocity. The HI tilts the objects by angles θ_a and θ_b, while keeping a correlation between the transversal direction of the eigen-directions and the separation vector. This effect results in repulsion between the objects while they continuously rotate in the $xy-$plane. Here we show a snapshot of this terminal evolution. The main figure shows the projection of the system (the objects and their eigen-directions) onto the xz-plane, whereas the inset shows the $xy-$plane projection, together with the separation vector $\mathbf{R}$.

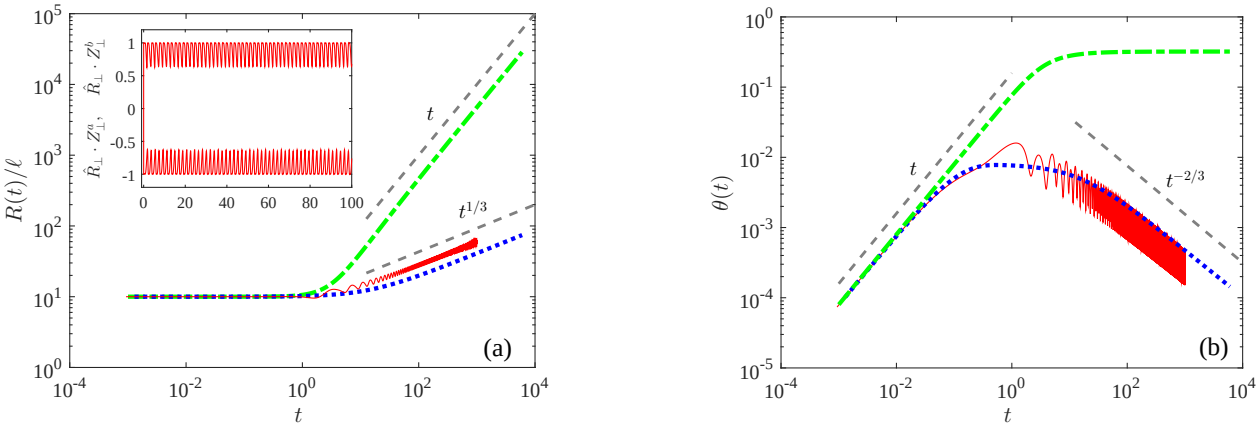

Figure 3.4: Representative trajectories for systems of two uniform spheroids (dash-dotted green curves), a pair of self-aligning spheroids (dotted blue curves), and two self-aligning stokeslets objects (solid red curves), together with the asymptotic behaviors at short and long times (gray dashed lines). The results are presented in dimensionless units by setting the parameters of length and time to $\ell = 1$ and $(\alpha F/8\pi\ell)^{-1} = 0.1$, and the additional parameters to the values detailed in Appendix D.2. The distance between the objects, $\mathbf{R}(t)$, as a function of time is shown in panel (a), exhibiting the effective repulsion between the two objects. The inset demonstrates the correlation between the eigen-directions $\hat{\mathbf{Z}}^a$, $\hat{\mathbf{Z}}^b$, and the separation vector in the case of self-aligning irregular objects. Panel (b) shows the evolution of the tilt angle θ, defined in Fig. 3.3 (the solid red curve corresponds to only one of the objects).

Two Uniform Prolate Spheroids

A pair of uniform spheroids exhibits quite different behavior from that of two self-aligning objects. An individual uniform spheroid ($h = 0$) does not rotate under forcing, and does not translate in response to a flow gradient, i.e., the $\mathbb{T}_{(0)}$ matrices and Π tensors in Eq. (3.8)–Eq. (3.10) vanish[4]. Hence, in the far field dynamics of two uniform spheroids the alignability and direct interaction are absent, i.e., $\alpha = \zeta = 0$ in Eq. (3.11) and Eq. (3.12). The resulting picture, arising from Eq. (3.11) and Eq. (3.12), is that θ increases linearly with time until saturating to a constant value, which depends on $R(t = 0)$, and the objects move away from each other with a constant terminal velocity[5]; see also dash-dotted green curves in Fig. 3.4. Hence, the role of HIs in this case is solely the generation of opposite tilts between the objects, which, as a result, move in opposite directions. In this case, Eq. (3.13) becomes equivalent to the one-dimensional problem from classical mechanics of two particles with a central repulsive potential, $\ddot{x} = Ax^{-2}$, and the initial conditions $x(0) = x_0$ and $\dot{x}(0) = 0$. The qualitative behavior is apparent from the corresponding velocity equation $\dot{x} = \sqrt{2A(x_0^{-1} - x^{-1})}$. The positive velocity increases x, which in turn increases $\dot{x}$ toward a constant value, whereby x continues to grow linearly with time.

The two power laws — $R(t) \sim t^{1/3}$, derived theoretically for self-aligning spheroids and demonstrated numerically for irregular objects, and $R(t) \sim t$, derived in the symmetric case of two uniform spheroids — are universal. Thus, the repulsive dynamics of pairs of symmetric objects and self-aligning objects are superficially similar, in that both arise from opposite tilts of the two objects. However, the mechanisms of the two repulsions differ qualitatively. The additional tendency of the latter objects to align with the force leads to a decrease in the relative velocity, as reflected by a weaker power law for the increase of separation with time. In addition, the terminal relative velocity in the case of two uniform spheroids is sensitive to the initial separation, as well as to the initial tilts. By contrast,the self-aligning pair has a stable asymptotic velocity independent of the initial state of alignment (assuming that $R(t = 0) \gg \ell$ such that the far-field equations, Eq. (3.8)–Eq. (3.10), are valid).

Effect of Longitudinal Separation

Up until now we have examined the simple case of constant force with initial separation perpendicular to its direction. As explained below, a small additional separation along the direction of the force should not alter qualitatively the transversal repulsion.

[4]In Appendix B we have shown that Π^T gives the force-dipole at the object's origin, induced by external forcing. The geometry of a uniform spheroid is invariant under inversion symmetry, thus, the corresponding Π tensor must vanish.

[5]This behavior occurs in the limit of far-field dynamics. When the initial separation is small, the assumption $\theta \ll 1$ is not valid, or a periodic motion might appear; see Refs. [59, 60, 124].

The evolution of the longitudinal separation differs from the transversal one. The two components governing the far-field transversal dynamics — mutual relative orientation between the objects (the opposite tilt) and the direct interaction which decays as R^{-2} — are weaker, or even absent, in the longitudinal dynamics. First, the direct interaction, originating from the off-diagonal blocks of the pair-mobility $\mathbb{A}$, vanishes due to the constraint that $\mathbb{A}$ is a symmetric matrix [31–33]. The components relating one object's linear velocity along the $\hat{\mathbf{z}}$ direction with forcing on the other, satisfy $\mathbb{A}^{ab}_{zz} = \mathbb{A}^{ba}_{zz}$, which implies $\dot{R}_z = (\mathbb{A}^{ab}_{zz} - \mathbb{A}^{ba}_{zz})(-F) = 0$. Hence, relative longitudinal dynamics is solely dictated by relative orientation between the objects, which in the far-field regime corresponds to the difference between the (unperturbed) self-responses of each object.

When $R_z \ll R_\perp$ we can approximate the objects' orientations by two opposite tilts of their eigen-directions. If the object's shape is invariant under rotations about the eigen-direction, e.g., self-aligning spheroid, such relative orientation cannot yield relative velocity along the z-axis. In the case of arbitrarily shaped, self-aligning objects, we expect that any asymmetry about the eigen-direction approximately averages out by the rotation of each object. Thus, the effect of opposite tilts on the relative translation along the direction of the force is weaker than that on the transversal one. Indeed, the examples in Fig. 2.5 have shown that the longitudinal separation evolves slowly in time and seems to saturate at long times.

3.3 Discussion

This Chapter has been devoted to the relative motion between two equally forced objects. The first part (Sec. 3.1) has established the basic geometry dependence of the effective interaction. We have proven that invariance under spatial inversion precludes any instantaneous relative translation. In the second part (Sec. 3.2), we have treated the effect of hydrodynamic interactions on time-dependent trajectories. We have demonstrated how the characteristic $R_\perp(t) \sim t^{1/3}$ repulsion between two self-aligning objects differs qualitatively from the counterpart, asymptotic $R_\perp(t) \sim t$ behavior, which corresponds to two uniform spheroids. The preferred alignment of the individual objects reduces the relative tilt as they get further apart, thus decreasing their relative translation compared to the constantly tilted spheroids. This case highlights the sharp contrast between motion conditioned by current configuration and time-integrated motion. Two initially aligned spheroids do not have instantaneous relative velocity, while two self-aligning objects do (due to the direct interaction, $\sim R^{-2}$, term). Yet, the orientational interaction between the spheroids makes them oppositely tilt and achieve with time an asymptotic translational velocity which exceeds that of the self-aligning objects.

We have applied our general symmetry criterion to systems with confining boundaries, which break inversion symmetry. This geometrical consideration, without any further detail, accounts for the apparent interactions originated in hydrodynamic coupling, which were ob-

served in optical-tweezers experiments involving two confined configurations [65, 66]. Previous works [64, 66] examined these apparent interactions for two point-like objects. Our treatment shows that the existence of the effect can be inferred by symmetry. It is present, therefore, in more general situations, such as non-spherical objects (e.g., Fig. 3.2(a)) and arbitrary separations, including objects in close proximity.

The symmetry arguments, which we have applied in the first part of this Chapter, can be found useful in the examination of orientational dynamics. In a system with spatial inversion symmetry, object a has the same translational response as object b, and an opposite rotational response. Hence, when the objects are subjected to *opposite* forces, e.g., in the presence of a central force of interaction between them, they must rotate in the *same* sense, and spatial inversion symmetry will be maintained at all times. This means that, in the dynamics of an enantiomorphic pair under opposite drive, relative orientations, possessing a spatial inversion symmetry, are fixed points in the orientational space, preserving a constant phase difference.

Finally, the distinction between irregular objects and regular ones, on the level of a pair of objects, should be significant, in particular, in driven suspensions with many-body interactions. For example, sedimentation of spheres involves only three-body effective interactions, whereas a suspension of sedimenting irregular objects will include effective *pair*-interactions. In the next Chapter we show how the effects demonstrated in this Chapter— the interplay between alignability and gliding— control concentration and velocity correlations in a driven suspension of self-aligning objects.

Chapter 4

Screening, Hyperuniformity, and Instability in the Sedimentation of Irregular Objects[1]

The details of the fundamental dynamical process of sedimentation are still under debate (see Sec. 1.6.1). The long-range hydrodynamic correlations among settling objects lead to chaotic many-body dynamics, exhibiting strong fluctuations and large-scale dynamic structures even for athermal (non-Brownian) objects with negligible inertia [71, 75, 76, 135]. The non-equilibrium nature originating in the external (gravitational) drive, together with the long-ranged, many-body hydrodynamic interactions, make the analysis of this ubiquitous phenomenon challenging.

Earlier theories of steady collective sedimentation have considered symmetric objects, such as spheres (see Refs. [63, 78] and references therein), spheroids [95, 96], rod-like objects [97–103], and permeable spheres [104]. In various scenarios, including applications involving fluidized beds, the suspensions contain objects of asymmetric shapes. In this Chapter we address the sedimentation of a large class of irregular objects which are self-aligning (see Sec. 1.4.3).

4.1 Scaling Argument

We begin with a qualitative description of the effects studied here. Consider a suspension of objects sedimenting in a viscous fluid of viscosity η under force F in the $-z$ direction. The mean concentration is c_0. Let us imagine a sinusoidal variation about c_0, $c(x)$, in the transverse

[1] The material presented in this Chapter was published in T. Goldfriend, H. Diamant, and T. A. Witten, Phys. Rev. Lett. **118**, 158005 (2017) [134].

x direction, creating vertical slabs of heavier and lighter weights. This creates a fluid velocity variation, $u(x)$. To find the amplitude of this variation we balance the change in gravitational force with the change in viscous drag (per unit area of the slab), $c\lambda F \sim \eta u/\lambda$, resulting in $u \sim c\lambda^2 F/\eta$. This indefinite increase of u with λ is a manifestation of the Caflisch-Luke problem mentioned in Sec. 1.6.1 — the seeming divergence of velocity fluctuations with system size. The relative velocity of the slabs creates a vorticity ω_{flow} of order $u/\lambda \sim c\lambda F/\eta$. For spheres, this vorticity merely rotates the objects. Self-aligning objects, by contrast, are tilted away from their aligned state. Their misalignment, proportional to ω_{flow}, makes them glide in the x direction with velocity $V_\perp \sim \gamma \ell c \lambda F/\eta$, where ℓ is the size of the object and γ a proportionality coefficient. (The tilt-and-glide effect was discussed in detail in Chapter 3.) The time derivative of concentration, arising from the gradient of flux, reads $\dot{c} \sim -c_0 V_\perp/\lambda = -(\gamma \ell c_0 F/\eta)c$. Now, if the coefficient γ is positive, the response suppresses the inhomogeneity, whereas if it is negative the inhomogeneity is enhanced. This is a mechanism of either screening or instability. In addition, the independence of the last relation on λ implies (for $\gamma > 0$) a non-diffusive fast relaxation over large length scales. As shown below, this leads to a hyperuniform dynamic structure. By equating the diffusive and non-diffusive relaxation rates of a slab, $D\lambda^{-2} = \gamma \ell c_0 F/\eta$, where D is the hydrodynamic diffusion coefficient, we find a typical wavelength above which hyperuniformity sets in, $\xi = [\gamma \ell c_0 F/(\eta D)]^{-1/2}$. Note that the mechanism just described does not work for concentration variations in the z direction[2].

4.2 Quantitative Model

To study these effects in more detail we use the framework of fluctuating hydrodynamics—Eq. (1.44) presented in Sec. 1.6.1. Similar continuum approaches were used for spheres by Levine et al. (referred to hereafter as LRFB) [88], and by Mucha et al. [94]. We consider an athermal inertia-less suspension. The system depends on the following parameters: the gravitational force on a single object, F; solvent viscosity η; characteristic size of the objects ℓ; and mean concentration of objects c_0. In addition, a self-aligning object has an alignability parameter α, giving the slowest relaxation rate of a mis-aligned orientation toward alignment[3], $t_{\text{align}}^{-1} = \alpha F/(\eta \ell^2)$. This parameter is derivable from the object's shape and mass distribution alone.

The stochastic response of the suspension is characterized by a phenomenological diffusion coefficient D, measurable experimentally [75], and fluctuating object fluxes with variance $2c_0 N$. The parameters D and N, which originate in the complex many-body interactions excited by the force F at each object, are in general anisotropic [75, 88, 136]. Yet, unlike LRFB, the effects discussed below do not depend crucially on this anisotropy; we therefore neglect it for the sake of simplicity.

[2] The situation for symmetric, non-aligning objects, such as spheroids, is more complicated since the unperturbed object does not have a well-defined orientation with the force [95].

[3] $\alpha = \max\{\alpha_1, \alpha_2\}$, where $\alpha_{1,2}$ were introduced in Sec. 1.4.3.

In addition, we employ the following three assumptions: (1) the suspension is dilute, having volume fraction $\varphi \ll 1$, such that direct interactions between the objects are negligible, and the hydrodynamic interaction is well described by its two leading multipoles. (2) The suspension is non-Brownian, i.e., the thermal Péclet number $F\ell/(k_BT) \gg 1$, where k_BT is the thermal energy. However, there is no restriction on the *sedimentation* Péclet number, defined as $\mathrm{Pe} \equiv F/(\eta D)$. (3) We assume strong alignability, i.e., that the rate of alignment t_{align}^{-1} is much faster than the interaction-induced vorticity, $\omega_{\mathrm{flow}} \sim 1/(\eta l^2)$, where $l \sim \ell\varphi^{-1/3}$ is the typical distance between objects. The resulting criterion, $\alpha \gg \varphi^{2/3}$, improves with dilution.

The advection-diffusion equation for the fluctuations of object concentration about c_0, $c(\mathbf{r},t)$, reads

$$\partial_t c + \nabla\cdot((c+c_0)\mathbf{V}) = D\nabla^2 c + \nabla\cdot\mathbf{f}, \tag{4.1}$$

where $\mathbf{V}$ is the objects' velocity fluctuation field about the mean settling velocity. The velocity fluctuation of the fluid surrounding the objects, $\mathbf{u}(\mathbf{r},t)$, is described by an incompressible, overdamped Stokes flow, with force monopoles originating from concentration fluctuations[4],

$$u_i(\mathbf{r},t) = \int d^3r' \mathbb{G}_{ij}(\mathbf{r}-\mathbf{r}')c(\mathbf{r}',t)F_j(\mathbf{r}') + O(\ell) = -F\int d^3r' \mathbb{G}_{iz}(\mathbf{r}-\mathbf{r}')c(\mathbf{r}',t) + O(\ell). \tag{4.2}$$

A point-like object ($\ell \to 0$) is merely advected by the flow, i.e., $\mathbf{V} = \mathbf{u}$. However, for nonzero ℓ the two velocities do not coincide. To leading order in ℓ they are bound to satisfy a relation of the form,

$$V_i = u_i + \ell\Phi_{ikj}\partial_j u_k + O(\ell^2). \tag{4.3}$$

The constant tensor Φ depends on the objects' orientations and shapes, and is assumed to be independent of c[5]. It is not exactly the Φ tensor appearing in Chapter 2, but rather an effective response which also accounts for the tilt-and-glide effect introduced in Chapter 3 and mentioned in the scaling argument above. The difference between $\mathbf{V}$ and $\mathbf{u}$, and the fact that the effective response Φ is anisotropic, lead to a new advective term in Eq. (4.1), which corresponds to an object flux with non-zero divergence, $\partial_i V_i = \ell\Phi_{ikj}\partial_i\partial_j u_k + O(\ell^2) \neq 0$. The second term in Eq. (4.3) is at the core of the present theory; the existence of asymmetry in Φ_{ikj}, demanded phenomenologically for self-aligning objects, entails the effects described below. (For spheres the second term in Eq. (4.3) vanishes, and the higher-order terms are divergence-less.) The anisotropic response has two contributions: one from a direct translational response to shear flow, and the other due to the object's gliding response; see more details in Appendix E.

We proceed by substituting Eq. (4.2) and Eq. (4.3) into Eq. (4.1) and Fourier-transforming

[4] Although a dipolar term (see Sec. 2.2) of order ℓ should be included in Eq. (4.2) to have a consistent expansion to first order in ℓ, this divergenceless term has no effect on the results.

[5] The mean-field assumption of constant Φ is valid provided that the motion of the isolated self-aligning object under external force and flow gradient can be characterized by axisymmetric hydrodynamic tensors.

the resulting equation ($(\mathbf{r},t) \to (\mathbf{q},\nu)$). This leads to

$$-i\nu\tilde{c}(\mathbf{q},\nu) + \frac{c_0\ell F}{\eta}\left(\gamma\frac{q_\perp^2}{q^2} + \bar{\gamma}\frac{q_\perp^4}{q^4}\right)\tilde{c}(\mathbf{q},\nu) + iF\int q_i\tilde{\mathrm{G}}_{i3}(\mathbf{q}')\tilde{c}(\mathbf{q}-\mathbf{q}',\nu-\nu')\tilde{c}(\mathbf{q}',\nu')d^3q'd\nu' \\ = -Dq^2\tilde{c}(\mathbf{q},\nu) - i\mathbf{q}\cdot\tilde{\mathbf{f}}(\mathbf{q},\nu), \quad (4.4)$$

where we used the fact that $q_i'\tilde{\mathrm{G}}_{ij}(\mathbf{q}') = 0$ (incompressibility of Stokes flow). We denote by $\perp$ the horizontal components (x,y) of a vector. The coefficients γ and $\bar{\gamma}$ are effective response parameters resulting from the response tensor Φ (specifically, $\gamma = \Phi_{zzz} - \Phi_{z\perp\perp} - \Phi_{\perp\perp z}$, $\bar{\gamma} = \Phi_{\perp\perp z} + \Phi_{\perp z\perp} + \Phi_{z\perp\perp} - \Phi_{zzz}$). The second term in Eq. (4.4) corresponds to linear screening, which is nonzero for any wavevector $\mathbf{q} \nparallel \hat{\mathbf{z}}$. This term makes a simple perturbation theory in small concentration fluctuations valid, allowing us to neglect the third, nonlinear term that underlies the LRFB model (see discussion in Sec. 1.6.1). In addition, to facilitate the analysis, we omit the term proportional to $\bar{\gamma}$, which does not affect the following calculations. We thus have

$$-i\nu\tilde{c}(\mathbf{q},\nu) + \gamma\frac{c_0\ell F}{\eta}\frac{q_\perp^2}{q^2}\tilde{c}(\mathbf{q},\nu) = -Dq^2\tilde{c}(\mathbf{q},\nu) - i\mathbf{q}\cdot\tilde{\mathbf{f}}(\mathbf{q},\nu). \quad (4.5)$$

By equating the diffusive and screening terms in Eq. (4.5), we obtain the characteristic length that we qualitatively inferred in Sec. 4.1,

$$\xi = \left(\frac{\gamma c_0\ell F}{\eta D}\right)^{-1/2} = \ell\gamma^{-1/2}\varphi^{-1/2}\mathrm{Pe}^{-1/2}. \quad (4.6)$$

4.2.1 Results

We now summarize the main results, which are readily obtained from Eq. (4.2)–Eq. (4.5) (see Appendix F for detailed analysis).

We begin with the expressions for the concentration and velocity correlation functions at steady state ($\nu \to 0$):

$$S(\mathbf{q}) = \langle\tilde{c}(\mathbf{q},0)\tilde{c}(-\mathbf{q},0)\rangle = \frac{N}{D}\frac{q^2}{q^2 + \xi^{-2}(q_\perp/q)^2}, \quad (4.7)$$

$$\langle\tilde{V}_i(\mathbf{q},0)\tilde{V}_j(-\mathbf{q},0)\rangle = \frac{NF^2}{D}\frac{\tilde{\mathrm{G}}_{iz}(\mathbf{q})\tilde{\mathrm{G}}_{jz}(-\mathbf{q})q^2}{q^2 + \xi^{-2}(q_\perp/q)^2}, \quad (4.8)$$

where $S(\mathbf{q})$ is the static structure factor of the suspension. Fig. 4.1(a) shows $S(\mathbf{q})$ along different directions of $\mathbf{q}$. The structure factor decays to zero at small q, as q^2, in all directions except $\hat{\mathbf{z}}$, where it is a constant at small q.

Next, the velocity point-correlation functions are obtained by inverting back to real space

and taking the limit $r \to 0$,

$$\langle V_z^2(0)\rangle = 6\langle V_\perp^2(0)\rangle = \frac{3}{64}\varphi\frac{N}{D}\frac{\xi}{\ell}\left(\frac{F}{\eta\ell}\right)^2 = \frac{3}{64}\frac{N}{D}\left(\frac{D}{\ell}\right)^2\gamma^{-1/2}\varphi^{1/2}\mathrm{Pe}^{3/2}. \tag{4.9}$$

Finally, we give the asymptotic expressions at large distances ($r \gg \xi$) for the two-point correlations in real space. For the concentration correlations we get

$$\frac{D\xi^3}{c_0 N}\langle c(0)c(r\hat{\mathbf{z}})\rangle = \frac{12}{\pi}\frac{\xi^5}{r^5}, \qquad \frac{D\xi^3}{c_0 N}\langle c(0)c(r\hat{\mathbf{r}}_\perp)\rangle = \frac{\Gamma^2(5/4)}{2\sqrt{2}\pi^2}\frac{\xi^{5/2}}{r^{5/2}}, \tag{4.10}$$

where Γ is the Gamma function. The weaker decay $\sim r^{-5/2}$ applies strictly within the (x, y) plane. For the velocity correlations we get

$$C_{\perp\perp}(r\hat{\mathbf{z}}) = \frac{8\xi^3}{\pi r^3}, \qquad C_{\perp\perp}(r\hat{\mathbf{r}}_\perp) = \frac{\xi}{\pi r}, \tag{4.11}$$

$$C_{zz}(r\hat{\mathbf{z}}) = \frac{4\xi}{\pi r}, \qquad C_{zz}(r\hat{\mathbf{r}}_\perp) = \frac{2\xi}{\pi r}, \tag{4.12}$$

where $C_{ij}(\mathbf{r}) \equiv \langle V_i(0)V_j(\mathbf{r})\rangle/\langle V^2(0)\rangle$. Despite the emergence of the characteristic length ξ, the concentration and velocity correlations remain long-ranged, decaying algebraically with distance. In Fig. 4.1(b) we present the spatial velocity correlations at steady state along with their asymptotic power laws.

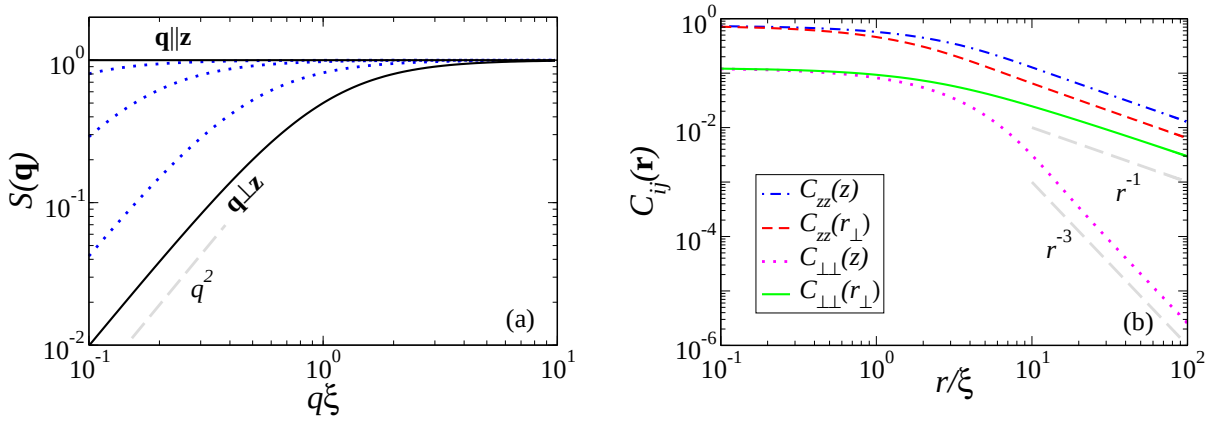

Figure 4.1: (a) Static structure factor of the suspension $S(\mathbf{q})$ (Eq. (4.7) with $N = D$) for different directions of the wavevector $\mathbf{q}$, as a function of the wavevector magnitude normalized with the characteristic length ξ. The blue dotted curves and the lower black solid curve, which correspond, respectively, to several directions of $\mathbf{q} \nparallel \hat{\mathbf{z}}$ and to $\mathbf{q} \perp \hat{\mathbf{z}}$, decay to zero at small q as $\sim q^2$. In the case of $\mathbf{q} \parallel \hat{\mathbf{z}}$ (upper black soild line) the structure factor is constant. (b) The decay with distance r of the normalized two-point velocity correlations, $C_{ij}(\mathbf{r}) \equiv \langle V_i(0)V_j(\mathbf{r})\rangle/\langle V^2(0)\rangle$, together with their asymptotic behavior (Eq. (4.11) and Eq. (4.12)). Here The diagonal zz and $\perp\perp$ components are presented for two specific directions of $\mathbf{r}$.

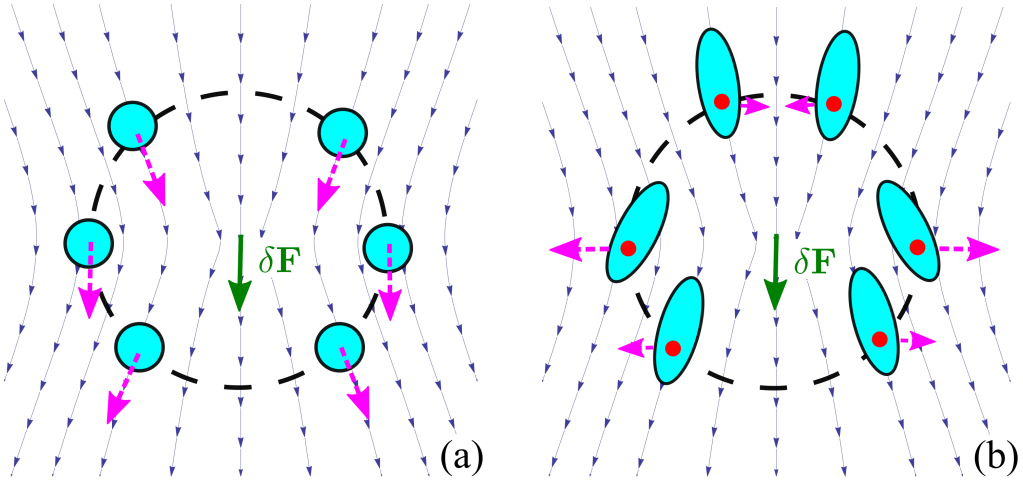

Figure 4.2: Illustration of the mechanism regulating concentration fluctuations. A concentration fluctuation makes a force fluctuation $\delta\mathbf{F}$ (green solid arrow), which in turn creates a flow fluctuation (flow lines). (a) Spherical objects respond isotropically to this flow, with velocities (magenta dashed arrows) along the direction of the flow lines; thus, there is no net flux of objects into the small volume element around the fluctuation. (b) Self-aligning spheroids have an anisotropic response, leading in this example to a total outflux of objects. The resulting flow of objects has a nonzero divergence, which reduces the concentration fluctuations.

4.3 Discussion

Let us now discuss the consequences of these results. The velocity auto-correlation of an object is given, up to corrections of $O(\ell/\xi)$, by the point-correlation of Eq. (4.9). From this expression we immediately see how the finite ξ regularizes the velocity auto-correlations, thus removing the Caflisch-Luke problem [82] for the irregular objects considered here. Indeed, in the limit $\gamma \to 0$ (no self-alignment) the auto-correlation diverges, requiring a different regularization mechanism [88, 94]. Fig. 4.2 illustrates another view of the physical mechanism behind the regularization[6]. A concentration fluctuation within a small volume of the suspension creates a flow, which advects objects in and out of the region. Spherical objects respond to the flow isotropically, leading to mutual cancellation of the influx and outflux (Fig. 4.2(a)). The dipolar, non-divergenceless flow of irregular objects, as described by Eq. (4.3), perturbs this balance, compensating for the deficiency/surplus of objects in the region (Fig. 4.2(b)).

In all of the above we have implicitly assumed that the effective response parameter γ is positive, leading to a positive ξ^2. However, γ may be of either sign, as we now show for self-aligning spheroids. These objects, already introduced in Chapter 3, are spheroids whose center of mass is displaced from their centroid. See inset of Fig. 4.3 and detailed calculation in Appendix E. The response parameter resulting from this calculation, shown in Fig. 4.3, reveals a region of negative γ as a function of the spheroid's aspect ratio κ and the off-center position

[6] Although this figure seems similar to the one drawn in Ref. [95] for symmetric, rod-like spheroids (which are not self-aligning), the scenarios are different. Whereas the rods are aligned by the flow lines, the ones depicted in Fig. 4.2(b) self-align with the force and are only perturbed by the flow lines.

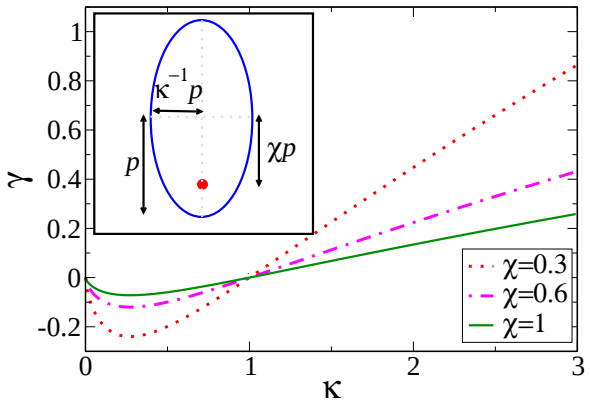

Figure 4.3: Effective response parameter γ describing suppressed fluctuations ($\gamma > 0$) and instability ($\gamma < 0$), as predicted for sedimentation of self-aligning spheroids (inset). The response of the spheroid is calculated as a function of its geometry, characterized by the aspect ratio κ, and the displacement of the forcing point (red dot) from the centroid, given by χ. Prolate self-aligning spheroids ($\kappa > 1$) cause suppression, whereas oblate ones ($\kappa < 1$) undergo instability. For spheres ($\kappa = 1$) our suppression/enhancement mechanism disappears ($\gamma = 0$).

of the forcing point[7] χ. As $\gamma \to 0^+$, the characteristic length ξ becomes indefinitely large. As is clear from the mechanism described above (Fig. 4.2), a negative γ implies de-regularization, i.e., instability in the sedimentation of such objects, with unstable structures of size $\sim \sqrt{-\xi^2}$. The instability clearly calls for additional theoretical and experimental study.

As described by Eq. (4.7) and Fig. 4.1(a) (in the case of positive γ), for any wavevector $\mathbf{q} \nparallel \hat{\mathbf{z}}$ the structure factor decays to zero for small wavevectors as $S(\mathbf{q}) \sim q^2$. This implies hyperuniformity of the fluctuating suspension [108, 137] in any direction but $\hat{\mathbf{z}}$. (See the discussion on hyperuniformity in Sec. 1.6.2.) Calculating the fluctuation δN in the number of objects within a spherical subvolume of radius R, we find $\delta N^2 \sim R^3(R/\xi)^{-1}$, i.e., a variance that grows as the surface area rather than the volume [137]. The hyperuniformity is also manifest in the long-range concentration correlations in the transverse direction, as given in Eq. (4.10). In the $\hat{\mathbf{z}}$ direction $S(\mathbf{q})$ is constant for small q, implying normal Poissonian fluctuations. The angular dependence of the suppression has been qualitatively explained in Sec. 4.1. For $q \neq q_z$ and $q < \xi^{-1}$ the vorticity-tilt effect (with rate $D\xi^{-2}$) dominates diffusion (with the slower rate Dq^2), while for $q = q_z$ this effect is absent. Several systems exhibiting hyperuniformity have been recently studied [108, 110–112]. Our system is different in several essential aspects: (1) it is dynamic, corresponding to continually changing configurations rather than a static absorbing state, (2) it does not require tuning of a control parameter to a critical value, (3) rather than eliminating collisions, it suppresses both positive and negative concentration fluctuations[8].

It has been assumed for simplicity that all the objects are identical, but the qualitative conclusions apply in more general scenarios. The key requirement is that the system contains self-aligning objects, possessing the dipolar anisotropic response treated above. Not all the

[7] In Chapter 3 we use a different representation for this off-center position; see Appendix C.

[8] The one-component plasma [63, 137] is another example of hyperuniformity brought about by long-ranged pair-interactions (electrostatic interactions in this case), falling off as $1/r$.

objects in the suspension need to be self-aligning, and the self-aligning ones do not need to be identical. In any of these scenarios they will tilt and glide in response to the nonuniform flow, thus producing the suppression or instability mechanisms discussed here.

We now compare our screening mechanisms with the ones suggested for the sedimentation of spheres (see discussion in Sec. 1.6.1). Those theories also yielded suppression of fluctuations, but out of different physics. (Indeed, hyperuniformity was found in numerical simulations [91] and experiments [90] of sedimenting spheres.) In the theory of Ref. [88] the effects result self-consistently from the nonlinear coupling between concentration and velocity fluctuations, giving $\xi_{\mathrm{LRFB}} \sim \ell\varphi^{-1/3}\mathrm{Pe}^{-2/3}$. The mechanism of Ref. [94] relies on a steady concentration gradient (stratification), yielding $\xi_{\mathrm{strat}} \sim \ell\varphi^{-1/4}\mathrm{Pe}^{-1/4}$. Which of these is the actual screening mechanism for spheres remains an open question. If the LRFB mechanism is the one that operates for spheres, then, for asymmetric objects, our linear mechanism with $\xi = \ell\gamma^{-1/2}\varphi^{-1/2}\mathrm{Pe}^{-1/2}$ should replace the nonlinear one; the linear glide solution is perturbatively stable against the nonlinear term at steady state, as explained in Appendix G. If stratification is the active mechanism for spheres, then screening will be caused by a combination of both stratification and asymmetry. Another distinctive feature of the asymmetry mechanism is that it remains in place as the system approaches detailed balance ($D = N$), whereas the LRFB screening disappears [88]. Thus, we expect the present mechanism to hold for arbitrarily small sedimentation Péclet number (while keeping the thermal Pe large).

Chapter 5

Summary and Outlook

Establishing the role of hydrodynamic interactions in a driven suspension of asymmetric colloids is the central achievement of this Thesis. The results highlight the qualitative difference between driving symmetric objects and asymmetric ones in the inertia-less regime. The theoretical results in Chapters 2–4 set the ground for further related theoretical studies and experimental investigations, as will be outlined below.

5.1 Pair Hydrodynamic Interactions

5.1.1 Summary

Chapter 2 and Chapter 3 have aimed to provide a comprehensive description of the translational and orientational hydrodynamic interactions between two forced objects, focusing on the generic features of these interactions. The study can be divided into two aspects (not directly related to the partition into the two chapters): the first deals with the instantaneous response of a given pair configuration, whereas the second addresses the time-dependent trajectories of object pairs.

In the first aspect, we have derived a formalism to predict from the system's symmetry alone whether the hydrodynamic interactions create relative motion (orientational or translational) between the objects. Where relative motion is present, we have analyzed its multipole expansion. In particular, based on the multipole expansion in ℓ/R of the pair-mobility in the case of two arbitrarily shaped objects having typical size ℓ, and separated by a distance R, we have shown that HI linearly degrades orientational alignment between self-aligning objects. The leading order of the interaction is dipolar, $\sim R^{-2}$, and can be written as a product of medium-dependent and object-dependent responses (see Eq. (2.12)). In addition, we have

shown how symmetry-based arguments can be useful in examining the instantaneous translational response of a pair. We have proven that spatial inversion symmetry dictates the vanishing of relative translation. In addition, we have managed to include under the same framework of geometrical considerations: (*i*) the previous theoretical studies of experiments in which apparent interactions were observed, e.g., radial separation between two spheres forced to move along a ring [66]; (*ii*) new predictions of apparent interactions, e.g., the separation between two spheres sedimenting one above the other parallel to a wall.

While our symmetry-based results for the instantaneous interaction are rigorous, in the second aspect of the study we could provide only qualitative general trends concerning the time-dependent relative motion. We have focused particularly on irregular, self-aligning objects, and on the asymptotic dynamics at long times. By carrying out numerical simulations to study the evolution of pair trajectories (translational and rotational), we have found that self-aligning objects typically repel each other, and thus, retain their alignment at long times as the $\sim R^{-2}$ HI gets weaker. The temporal asymptotic evolution follows the law $R(t) \sim t^{1/3}$. A quantitative explanation of this behavior has been given by treating analytically a simpler case of self-aligning spheroids. The typical $t^{1/3}$ separation between self-aligning objects is qualitatively different from the $R(t) \sim t$ law characterizing the case of uniform prolate spheroids.

The symmetry-based results concerning the relative translation of a pair (Sec. 3.1) remain intact even if the objects are at close proximity (see Sec. 3.3). However, the two analytical results which rely on the far-field approximation— the instantaneous degradation of orientational alignment (Sec. 2.2) and the typical repulsive trend between two self-aligning objects (Sec. 3.2.3)— may change qualitatively when the distance between the objects is comparable to their size. In addition to the higher order terms of the pair-mobility matrix that contribute to the dynamics at small separations, there are hydrodynamic, near-field repulsive interactions, i.e., lubrication effects, which dominate at close proximity [1]. It is difficult to anticipate whether and when the near-field dynamics would differ qualitatively from the one in the far-field regime. In particular, the typical repulsion between object pairs, caused by a mutual tilt-and-glide effect, might be irrelevant when the objects start at small initial separation— although lubrication effects are repulsive (thus, pushing the objects toward larger separation, where the far-field result becomes more relevant), higher multipoles of the pair hydrodynamic interaction can change the picture. For example, the separation between two uniform spheroids, which start at close proximity, exhibits a periodic trajectory [124].

5.1.2 Experimental Significance

The initial motivation for this Thesis was to explore the feasibility of achieving orientational order of asymmetric colloids by a time-dependent forcing protocol, as was suggested by Refs. [34, 46–48]. Our results imply that such an orientationally ordered system of steerable colloids is restricted to dilute suspensions, as hydrodynamic interactions degrade alignment. In particu-

lar, we have estimated an upper bound of $\varphi \sim 10^{-3}$, above which HIs have a significant effect on the orientational dynamics in a suspension. The usage of other driving mechanisms such as electrophoresis, that do not include net external force on the objects, and therefore involve weaker HI, is thus preferable.

The results have an impact on other, simpler, colloidal systems. The general theory presented in Chapter 3 can be used to obtain simple qualitative predictions, which are readily testable in experiment. A particularly simple example is the sedimentation of two identical spheres, positioned one above the other parallel to a vertical planar wall. This configuration will result in one sphere instantaneously approaching the wall, while the other being repelled from the wall. Another example is a modification of the experiment presented in Ref. [66]. Two identical spheres placed in a ring and forced in the radial direction will develop relative translation in the tangential direction. Clearly, similar symmetry-based predictions can be readily made for other configurations. We note that the general symmetry criterion concerns only the existence or absence of interaction. To determine the sign of the interaction, whether it is repulsive or attractive, one needs additional information such as the Green's function of the given hydrodynamic problem.

Another result, which can be verified in a simple experimental setup, is the asymptotic power-law time dependence of the separation between two self-aligning objects. For the particular system comprising a pair of self-aligning (non-uniform) prolate spheroids we have shown analytically a $t^{1/3}$ law (Sec. 3.2). In the case of two, arbitrarily shaped self-aligning objects, where repulsion is not a general law, we have reported several examples with a similar trend. These examples, which are represented by the red curve in Fig. 3.4, are not sensitive to initial conditions. For spheroids, the effect of opposite tilts on the mutual repulsion is captured by the positive glide parameter β in Eq. (3.11). The sign of β is dictated by the elongated shape of the individual spheroid. (An oblate spheroid has a negative β, see Appendix E.). Therefore, good candidates for arbitrarily shaped, repulsive pairs may be elongated objects, whose properties, when averaged over rotations about the eigen-direction, resemble those of self-aligning spheroids. A suggestion for an experiment includes tracking the sedimentation of two micron-sized, self-aligning objects in a viscous fluid, where optical traps can be used to place the objects at a fixed initial separation, perpendicular to gravity. The effect should not depend on the initial orientations of the objects, as their alignability guarantees that after a short transient they will be close to their aligned state.

5.1.3 Future Theoretical Directions

The tools that we have developed to treat hydrodynamic interactions— multipole expansion and symmetry considerations— can be generalized to examine other driving mechanisms. One example is electrophoresis, the transport of charged colloids in electrolyte as a response to external electric field. Electrophoretic motion is force-free, as the driven object is effectively neu-

trally charged due to the cloud of counter-ions surrounding it. While previous works studied the response of specific pair configurations, it will be useful to lay a framework of multipole expansion, similar to the one in Sec. 2.2, to study the coupled electrophoretic motion of two arbitrarily shaped objects. Symmetry considerations, similar to those we have employed for not-force-free objects, might be useful to understand pair electrophoretic response. The motion of two identical spheres, or spheroids, with the same constant surface charged distribution do not induce relative translation [138–140] (moreover, the interaction in this case completely vanishes, *viz*, the presence of one object does not affect the individual response of the other). This surprising and general result calls for symmetry-based explanation. There is a previous study in this spirit, given in Ref. [141], concerning the motion of single object. It indicated what geometrical properties of the individual object can yield complex motion such as rotation under unidirectional external electric field.

Another future direction is to study the hydrodynamic interaction between asymmetric objects possessing a magnetic dipole, which are driven by a rotating magnetic field. On a single object level, such objects align, rotate and translate according to the external rotating field, and their dynamics can be easily controlled via the frequency of the field [2]. Therefore, these objects acquire orientational alignment with the direction of the field's rotation axis, similar to the self-aligning objects studied in this Thesis. The ideas and methods developed in Chapter 2 and Chapter 3 can be generalized to the case in which a total torque is acting on each object. For example, since a torque is a pseudo-vector, one can show by symmetry arguments that the hydrodynamic interaction can induce a relative linear velocity between an enantiomorphic pair subjected to the same torque. In addition, the second order (dipolar) term of the pair-mobility matrix, given in Eq. (A.2), produces a translation of one object due to a torque on the other. However, this term does not induce rotation. Therefore, in the presence of external torque alone, the tilt-and-glide effect and degradation (or enhancement) of orientational alignment will be weaker than in the case of self-aligning objects. A system of asymmetric objects actuated by a rotating magnetic field is an example of steerable colloids which can be realized in experiments [2]. Studying the effects of hydrodynamic interactions in such systems is an interesting direction of research that can be based on the results obtained in this Thesis.

The typical effective repulsion between pairs of self-aligning, arbitrarily shaped stokeslets objects, which were reported in Chapter 2, is not a general law; Attractive trajectories and bound states have been observed as well. This fact brings to mind two directions to extend the study of pair HI. First, what is the mechanism dictating attraction? It can be an opposite tilt-and-glide effect. Indeed, we know of objects with such property (for example, oblate self-aligning spheroids, whose response causes an unstable sedimenting suspension, as can be inferred from Fig. 4.3) . If this is the case, then one should answer the question what is the relation between the self-aligning character and the gliding response, as our randomly generated 4-stokeslets objects usually exhibit positive tilt-and-glide response.

A second interesting direction concerns the bound state trajectories, as the one shown by

the blue dashed curve on Fig. 2.5e . Bound states were observed earlier in the case of symmetric objects [124]. Here a further study should examine the following issues: (*i*) the basin of attraction of bound states, (*ii*) whether such states are restricted only to close proximity or can occur also in the far-field regime, and (*iii*) the relation between the object's shape and the existence of a bound state. These general points can be explored by considering the far-field mobility derived in Sec. 2.2, and by further numerical investigation of stokeslets object dynamics. In addition, one may treat also the case of two non-identical objects.

Finally, we mention one of our symmetry-based conclusion— an enantiomorphic pair under opposite drive should maintain their relative orientation in space (see Sec. 3.3). This interesting prediction might have impact on colloidal systems in which there is a central force between the suspended objects. In particular, the effect can be related to colloidal synchronization or lock-and-key mechanisms, and thus, it clearly calls for further theoretical and numerical investigation.

5.2 Sedimentation

5.2.1 Summary

In Chapter 4 we have studied the overdamped sedimentation of non-Brownian objects of irregular shape using fluctuating hydrodynamics. We have found that the anisotropic coupling between the external drive, hydrodynamic interactions, and objects' orientations, directly suppresses concentration and velocity fluctuations. This allows the suspension to avoid the anomalous fluctuations predicted for suspensions of symmetric spheroids. The suppression of concentration fluctuations leads to a correlated, hyperuniform structure. For certain object shapes, the anisotropic response may act in the opposite direction, destabilizing uniform sedimentation.

5.2.2 Experimental Significance

The findings presented above for asymmetric dispersions can be checked experimentally, e.g., using light scattering or video microscopy. Our results highlight the different physics underlying the sedimentation of irregular objects as compared to spheroidal ones. This includes a distinctive, direct, screening mechanism, a different length scale ξ beyond which hyperuniformity sets in, and unstable dynamics for certain object shapes. These results may offer new means of controlling the stability of driven suspensions such as fluidized beds.

5.2.3 Future Theoretical Directions

The study on the sedimentation of self-aligning objects can be extended further in several aspects. The model we have utilized in Sec. 4.2 is general, treating arbitrarily shaped self-aligning objects whose alignability is captured by the shape-dependent response tensor Φ. We have developed methods (Sec. 2.3 and Appendix E) to explicitly determine this response for specific shapes. One can use this analysis to provide quantitative estimates of the strength of the stabilization mechanism for simple object's shape, and examine how geometry controls homogenization ($\gamma < 0$) or instability ($\gamma > 0$) of the suspension.

We have shown that the behavior of a driven, many-body system of self-aligning objects is qualitatively different from the one of spheres, which shows screening, and uniform spheroids, which exhibit instability. Therefore, it is natural to ask what is the interplay between the alignment mechanism that we have studied, and the ones which govern the behavior of suspensions of regular objects. As the fundamental details of each system, spheres or spheroids, are still not fully understood (or under debate) [78], a unified theory for sedimentation is far from reach. Yet, one can relate the known models of each regular class to that of the self-aligning class.

Spheres: our mechanism dominates at sufficiently small volume fractions, large distance scales, and no stratified suspension (i.e., without vertical concentration gradient). The fluctuating hydrodynamics model we have employed is a standard model to study sedimentation of spheres. One can use this framework to study the interplay between our tilt-and-glide effect and the screening mechanism induced by stratification [94], or three-body interactions [63].

Spheroids: the essential ingredient of the instability in sedimentation of spheroids [78, 95] resembles the alignment mechanism— gradients of fluid flow affect the probability of orientations, which is otherwise isotropic. The resulting anisotropic distribution of orientations gives rise, through gliding response, to divergence-less objects' fluxes; see Figure 1 in Ref. [95]. The predictions for the γ parameter of self-aligning spheroids (Fig. 4.3) are not applicable to describe this scenario, since the calculation relies on the assumption of slightly tilted spheroids. We have quantified this by the inequality $\alpha \gg \varphi^{2/3}$ in Eq. (E.6). One way to interpolate between the two effects is to calculate an effective $\Phi(\varphi)$ tensor that captures the response of both self-aligning spheroids and uniform ones. For a dilute system, with strong alignability, our calculation of Φ is valid; for high concentration and weak alignability, the value of Φ should give the divergence-less flows of objects according to the Koch and Shaqfeh theory [95]. A generalized theory, for self-aligning objects and non-alignable ones, will allow to draw a phase diagram of screened and unstable phases, which will depend on the volume fraction φ, and the suspended objects geometry, given by the parameters κ and χ (Fig. 4.3).

Appendices

Appendix A

Pair-Mobility: Further Details

The pair-mobility matrix has been at the core of the analysis in Chapter 2 and Chapter 3. In this Appendix we provide more details (especially technical ones) of this quantity.

A.1 Change of Object's Origin

Here we derive the transformation of the pair-mobility matrix under change of objects' origins. Consider a new choice of origins given by $\mathbf{R}'^{,a} = \mathbf{R}^a + \mathbf{h}^a$ and $\mathbf{R}'^{,b} = \mathbf{R}^b + \mathbf{h}^b$, and denote the objects' properties with respect to the new origins with $'$. Following Ref. [34], the transformations for the generalized velocities and forces can be written as $\underline{\mathbf{V}}'^{,x} = [\mathbb{I}_{6\times6} - (\mathbb{B}^x)^T]\underline{\mathbf{V}}^x$ and $\underline{\mathbf{F}}'^{,x} = [\mathbb{I}_{6\times6} + \mathbb{B}^x]\underline{\mathbf{F}}^x$ for $x = a, b$, where

$$\mathbb{B}^a = \begin{pmatrix} 0 & 0 \\ -\mathbf{h}^{a\times} & 0 \end{pmatrix} \text{ and } \mathbb{B}^b = \begin{pmatrix} 0 & 0 \\ -\mathbf{h}^{b\times} & 0 \end{pmatrix}.$$

Using $[\mathbb{I}_{6\times6} + \mathbb{B}^x]^{-1} = [\mathbb{I}_{6\times6} - \mathbb{B}^x]$ we have

$$\begin{pmatrix} \mathbb{M}'^{,aa} & \mathbb{M}'^{,ab} \\ \mathbb{M}'^{,ba} & \mathbb{M}'^{,bb} \end{pmatrix} = \begin{pmatrix} [\mathbb{I}_{6\times6} - (\mathbb{B}^a)^T] & 0 \\ 0 & [\mathbb{I}_{6\times6} - (\mathbb{B}^b)^T] \end{pmatrix} \begin{pmatrix} \mathbb{M}^{aa} & \mathbb{M}^{ab} \\ \mathbb{M}^{ba} & \mathbb{M}^{bb} \end{pmatrix} \begin{pmatrix} [\mathbb{I}_{6\times6} - \mathbb{B}^a] & 0 \\ 0 & [\mathbb{I}_{6\times6} - \mathbb{B}^b] \end{pmatrix}. \tag{A.1}$$

A.2 Proof of General Properties of Interaction Multipoles

Here we prove the two general results presented in Sec. 2.2 concerning the interaction multipoles.

Multipole expansions are constructed by repeated projections ("reflections"), between the two objects, of the Green's function and its derivatives. The self-blocks of the mobility matrix result from even projections, and the coupling blocks from odd projections. In our case $\mathbb{G}$, the Oseen tensor, has even parity and scales as $1/R$.

The Green's function $\mathbb{G}$ itself appears only once in the expansion, in the first $(1/R)$ multipole. This is because the force monopoles acting on the objects are prescribed. This monopolar (odd) interaction appears only in the coupling blocks. The leading multipole appearing in the self-blocks is constructed by projecting the induced force dipole on object 2 (proportional to $\nabla\mathbb{G}$) back onto object 1 (by another $\nabla\mathbb{G}$). Thus, this leading multipole is of 4th order, proportional to $1/R^4$. This proves the first result in Sec. 2.2. Its particular manifestation for two spheres is well known [32].

Now, consider the nth multipole, proportional to $1/R^n$. Assume that it contains k $\mathbb{G}$'s and $n-k$ derivatives. Its parity is $(-1)^{n-k}$. As explained above, for self-blocks k is even, and for coupling blocks it is odd. Hence, the parity of the nth multipole is $(-1)^n$ in the self-blocks and $(-1)^{n+1}$ in the coupling blocks. This proves the second result.

A.3 General Form of the 2nd-Order Multipole of the Pair-Mobility

The basic properties of the 2nd-order multipole of the pair-mobility matrix, $\mathbb{M}_{(2)}$, have been studied in Sec. 2.2. Here we provide the general form of the coupling block in this multipole term, $\mathbb{M}^{ab}_{(2)}$, and point out the number of its independent components. This is done by decomposing the tensors Φ and Θ into their symmetric and anti-symmetric parts; see Appendix B below. Without loss of generality we choose the separation vector between the two objects to be along the x axis, $\hat{\mathbf{R}} = \hat{\mathbf{x}}$. For two not necessarily identical objects the matrix $\mathbb{M}^{ab}_{(2)}$ has the form

$$\mathbb{M}^{ab}_{(2)} = \left(\frac{\ell}{R}\right)^2 \begin{pmatrix} \begin{pmatrix} A^a_{xx}-A^b_{xx} & -A^b_{yx} & -A^b_{zx} \\ A^a_{yx} & 0 & 0 \\ A^a_{zx} & 0 & 0 \end{pmatrix} & \begin{pmatrix} -T^b_{xx} & -T^b_{yx} & -T^b_{zx} \\ 0 & 0 & 1 \\ 0 & -1 & 0 \end{pmatrix} \\ \begin{pmatrix} T^a_{xx} & 0 & 0 \\ T^a_{yx} & 0 & 1 \\ T^a_{zx} & -1 & 0 \end{pmatrix} & 0 \end{pmatrix}, \tag{A.2}$$

where the A_{ij}^{x} and T_{ij}^{x} are functions of $\mathbf{R}$ and the shape and orientation of object x, $(x = a, b)$. For two identical (in shape and orientation) objects we have

$$\mathbb{M}_{(2)}^{ab} = \left(\frac{\ell}{R}\right)^2 \begin{pmatrix} \begin{pmatrix} 0 & -A_{yx} & -A_{zx} \\ A_{yx} & 0 & 0 \\ A_{zx} & 0 & 0 \end{pmatrix} & \begin{pmatrix} -T_{xx} & -T_{yx} & -T_{zx} \\ 0 & 0 & 1 \\ 0 & -1 & 0 \end{pmatrix} \\ \begin{pmatrix} T_{xx} & 0 & 0 \\ T_{yx} & 0 & 1 \\ T_{zx} & -1 & 0 \end{pmatrix} & 0 \end{pmatrix}. \tag{A.3}$$

A.4 Pair-Mobility Matrix of two Spheres Near a Wall

In Sec. 3.1.2 we have analyzed, based on symmetry considerations, a system comprising two spheres near a wall. While the symmetry arguments indicate a relative translation between the spheres, it does not tell us whether the objects repel or attract under a given forcing direction. Here we provide more detail regarding the pair-mobility matrix of that system. We write down the blocks structure of the corresponding $\mathbb{A}$ (derivable from symmetry alone), and provide an explicit expressions for the case of point-like objects.

A schematic description of the system is given in Fig. 3.2b. Without loss of generality we assume that the spheres are located along the x-axis, where $\mathbf{R} = x\hat{\mathbf{x}}$ points from the origin of sphere a to the origin of sphere b, and the wall is placed parallel to them at height $z = h$. The spheres' radii are denoted by ϱ. Hereafter we consider the projection of $\mathbb{A}$ onto the xz-plane. The properties of the y-axis components can be deduced from the additional symmetry of reflection about the xz-plane, which was not included in our analysis above. According to the discussion in Sec. 3.1.2 the pair-mobility matrix of this system has the following form:

$$\mathbb{A} = \begin{pmatrix} A_{xx}^{\text{self}} & A_{xz}^{\text{self}} & A_{xx}^{\text{coupling}} & A_{xz}^{\text{coupling}} \\ A_{zx}^{\text{self}} & A_{zz}^{\text{self}} & A_{zx}^{\text{coupling}} & A_{zz}^{\text{coupling}} \\ A_{xx}^{\text{coupling}} & -A_{xz}^{\text{coupling}} & A_{xx}^{\text{self}} & -A_{xz}^{\text{self}} \\ -A_{zx}^{\text{coupling}} & A_{zz}^{\text{coupling}} & -A_{zx}^{\text{self}} & A_{zz}^{\text{self}} \end{pmatrix}. \tag{A.4}$$

The number of independent components can be reduced further by using the fact that $\mathbb{A}$ is symmetric. This property is not related to the system geometry, which is the issue of Sec. 3.1.2, but rather results from Onsager relations or conservation of angular momentum in the system [31–33]. The symmetry of $\mathbb{A}$ connects between the xz and zx components: $A_{xz}^{\text{self}} = A_{zx}^{\text{self}}$ and $A_{xz}^{\text{coupling}} = -A_{zx}^{\text{coupling}}$. Finally, we get

$$\mathbb{A} = \begin{pmatrix} A_{xx}^{\text{self}} & A_{xz}^{\text{self}} & A_{xx}^{\text{coupling}} & A_{xz}^{\text{coupling}} \\ A_{xz}^{\text{self}} & A_{zz}^{\text{self}} & -A_{xz}^{\text{coupling}} & A_{zz}^{\text{coupling}} \\ A_{xx}^{\text{coupling}} & -A_{xz}^{\text{coupling}} & A_{xx}^{\text{self}} & -A_{xz}^{\text{self}} \\ A_{xz}^{\text{coupling}} & A_{zz}^{\text{coupling}} & -A_{xz}^{\text{self}} & A_{zz}^{\text{self}} \end{pmatrix}. \tag{A.5}$$

In the case of point-like objects, i.e., spheres with infinitely small radius, the blocks can be calculated explicitly. The self blocks are given by the self-mobility of a single sphere near a plane wall (first-order in ϱ/h) [32]

$$\mathbb{A}^{\text{self}} = \frac{1}{6\pi\eta\varrho}\begin{pmatrix} 1-\frac{9}{16}\frac{\varrho}{h} & 0 \\ 0 & 1-\frac{9}{8}\frac{\varrho}{h} \end{pmatrix}.$$

The coupling blocks, which correspond to the direct HI between the spheres, are given by the Green function of the Stokes equation with a no-slip, plane wall boundary (Eq. (1.17))

$$\mathbb{A}^{\text{coupling}} = \begin{pmatrix} \frac{2x^2(4h^2+x^2)^{5/2}-2(12h^4+4h^2x^2+x^4)|x|^3}{(4h^2+x^2)^{5/2}|x|^3} & -\frac{12h^3x}{(4h^2+x^2)^{5/2}} \\ \frac{12h^3x}{(4h^2+x^2)^{5/2}} & \frac{(4h^2+x^2)^{5/2}-48h^4|x|-10h^2|x|^3-|x|^5}{(4h^2+x^2)^{5/2}|x|} \end{pmatrix}.$$

The component $\mathbb{A}^{\text{coupling}}_{xz} = -12h^3x/(4h^2+x^2)^{5/2}$ is the one which was used in Ref. [64] to explain the effective attraction between two like-charged spheres near a similarly charged wall.

Appendix B

Properties of the Tensor Φ

Below we provide a more detailed discussion regarding the rank-3 tensor Φ introduced in Sec. 2.2 of Chapter 2 (the averaged Φ tensor, presented in Chapter 4, will be discussed in Appendix E). We consider its symmetries and its dependence on the choice of origin. We separate Φ into a translational part— linear velocity response to a flow gradient, denoted by Φ_{tran}, and a rotational part— angular velocity response to a flow gradient, denoted by Φ_{rot}. We show that Φ_{tran} is symmetric with respect to its last two indices while Φ_{rot} has also an antisymmetric part which is the Levi-Civita tensor. In addition, we show that Φ_{tran} depends on the choice of the object's origin whereas Φ_{rot} does not, and derive the transformation of the former under change of origins.

In order to prove the symmetry properties of Φ we consider its transpose tensor $\Phi^T = \tilde{\Phi}$ which gives the force dipole around the object when subjected to external forcing, $(\underline{\mathbf{rf}}) = \tilde{\Phi} \cdot \underline{\mathbf{F}} = \tilde{\Phi}_{\text{tran}} \cdot \mathbf{F} + \tilde{\Phi}_{\text{rot}} \cdot \boldsymbol{\tau}$. We write the force dipole as a sum of symmetric and anti-symmetric terms, $\frac{1}{2}\left[(\underline{\mathbf{rf}}) + (\underline{\mathbf{rf}})^T + \epsilon \cdot \boldsymbol{\tau}\right] = \tilde{\Phi}_{\text{tran}} \cdot \mathbf{F} + \tilde{\Phi}_{\text{rot}} \cdot \boldsymbol{\tau}$, where ϵ is the Levi-Civita tensor. The last equality implies that $(\tilde{\Phi}_{\text{tran}})_{ski}$ is symmetric with respect to s and k and that the anti-symmetric part of $(\tilde{\Phi}_{\text{rot}})_{ski}$ is $\frac{1}{2}\epsilon_{ski}$.

Following this analysis, in Chapter 3, we use the notation

$$\Phi_{\text{tran}} = \Pi, \tag{B.1}$$

$$\Phi_{\text{rot}} = \Psi - \frac{1}{2}\epsilon. \tag{B.2}$$

Next we consider the transformation of Φ under change of origins. Let us assume that an object is given in a constant, arbitrary shear flow $\mathbf{u}(\mathbf{r}) = S \cdot \mathbf{r}$, where S is not necessarily a symmetric matrix. The object's linear velocities measured about $\mathbf{R}$ and $\mathbf{R}' = \mathbf{R} + \mathbf{h}$ are $\mathbf{V} = S \cdot \mathbf{R} + \Phi_{\text{tran}} : S$ and $\mathbf{V}' = S \cdot (\mathbf{R} + \mathbf{h}) + \Phi'_{\text{tran}} : S$ respectively. The tensor Φ_{rot} does not depend on the choice of origin since the angular velocity of the object is independent of that

choice, $\boldsymbol{\omega} = \Phi_{\text{rot}} : S = \Phi'_{\text{rot}} : S$. Using the relation $\mathbf{V}' = \mathbf{V} - \mathbf{h} \times \boldsymbol{\omega}$ we find

$$\Phi'_{\text{tran}} : S = (\Phi_{\text{tran}} - \mathbf{h}^{\times} \cdot \Phi_{\text{rot}}) : S - S \cdot \mathbf{h}.$$

In general, with analogy to Eq. (A.1), we can write

$$\Phi' = [\mathbb{I}_{6\times 6} - (\mathbb{B})^T] \cdot \Phi + \Delta, \tag{B.3}$$

where[1]

$$\mathbb{B} = \begin{pmatrix} 0 & 0 \\ -\mathbf{h}^{\times} & 0 \end{pmatrix} \text{ and } \Delta_{iks} = \begin{cases} -\delta_{ik} h_s & , i = 1 \ldots 3 \\ 0 & , i = 4 \ldots 6 \end{cases}.$$

[1] This corrects a typo in Appendix C of Ref. [127].

Appendix C

Self-Aligning Spheroids

In Chapter 3 and Chapter 4 we have used self-aligning spheroids as a simple example of self-aligning objects. In each chapter we use a slightly different scaling and notation which serve the clarity of the respective analysis. Here we provide a general treatment concerning hydrodynamic tensors of self-aligning spheroids. Then, in Appendix D.1 and Appendix E.2 we relate these to the specific analysis of Chapter 3 and Chapter 4 respectively.

We consider a spheroid whose principal axes are $(\kappa^{-1}p, \kappa^{-1}p, p)$, as depicted in the inset of Fig. 4.3. The spheroid is subjected to an external force at a point which is displaced along the symmetry axis by a distance χp from the center. The axisymmetric shape allows us to represent the spheroid's orientation solely by its eigendirection, $\hat{\mathbf{n}}$, which is directed from the center to the forcing point. Below we consider the following hydrodynamic tensors: the self-mobility matrix $\mathbb{M}$, Eq. (1.23); the translational and rotational response tensors to flow gradient, which are characterized by the tensors of rank 3, Π and Ψ, respectively (see Appendix B).

We begin with the hydrodynamic response tensors of a uniform spheroid, i.e., whose forcing point is at its center ($\chi = 0$). These tensors, which will be indicated by the superscript c, can be found explicitly in the literature, $\mathbb{M}^c$ and Π^c can be found in Ref. [129], and Ψ is given in Ref. [133] (in Appendix B we show that Ψ is independent of the choice of origin, thus, we avoid its indication). In particular, the tensors are of the form:

$$\mathbb{A}^c_{ij}(\hat{\mathbf{n}}) = \frac{1}{6\pi\eta p}\left[A^c_\perp(\kappa)\delta_{ij} + \left(A^c_\parallel(\kappa) - A^c_\perp(\kappa)\right)\hat{n}_i\hat{n}_j\right], \tag{C.1}$$

$$\mathbb{S}_{ij}(\hat{\mathbf{n}}) = \frac{1}{8\pi\eta p^3}\left[S_\perp(\kappa)\delta_{ij} + \left(S_\parallel(\kappa) - S_\perp(\kappa)\right)\hat{n}_i\hat{n}_j\right], \tag{C.2}$$

$$\mathbb{T}^c_{ij}(\hat{\mathbf{n}}) = 0, \tag{C.3}$$

$$\Pi^c_{ij}(\hat{\mathbf{n}}) = 0, \tag{C.4}$$

$$\Psi_{ijk} = -\frac{\psi(\kappa)}{2}\left(\epsilon_{ijm}\hat{n}_m\hat{n}_k + \epsilon_{ikm}\hat{n}_m\hat{n}_j\right). \tag{C.5}$$

(The tensor $\mathbb{S}$, giving the angular velocity as a response to an external torque, is independent of the choice of origin.)

Now, the properties of self-aligning spheroids ($\chi \neq 0$), $\mathbb{A}$, $\mathbb{T}$ and Π, can be derived by change of origin transformation; see Eq. (1.24) for transformations which correspond to the tensors of rank 2, and Eq. (B.3) for transformations concerning the tensors of rank 3. Using these transformations we find that: the tensor $\mathbb{A}$ keeps its form,

$$\mathbb{A}_{ij}(\hat{\mathbf{n}}) = \frac{1}{6\pi\eta p}\left[A_\perp(\kappa,\chi)\delta_{ij} + \left(A_\parallel(\kappa,\chi) - A_\perp(\kappa,\chi)\right)\hat{n}_i\hat{n}_j\right]; \tag{C.6}$$

the twist matrix is antisymmetric,

$$\mathbb{T}_{ij}(\hat{\mathbf{n}}) = \frac{\chi S_\perp(\kappa)}{8\pi\eta p^2}\epsilon_{ikj}\hat{n}_k; \tag{C.7}$$

and the tensor Π is nonzero

$$\Pi_{ijk}(\hat{\mathbf{n}}) = -p\chi\left(\epsilon_{iml}\hat{n}_m\Psi_{ljk}(\kappa) + \delta_{ij}\hat{n}_k\right). \tag{C.8}$$

Finally, we point out the self-aligning character that is captured by the twist matrix $\mathbb{T}$, see Sec. 1.4.3. The twist matrix of a self-aligning spheroid has one real eigenvalue which is zero, where the corresponding eigendirection is $\hat{\mathbf{n}}$. In addition, the rate of alignment is given by $\chi S_\perp(\kappa)/(8\pi\eta p^2)$. The case of a uniform spheroid, i.e., $\chi = 0$, is lack of alignability.

Appendix D

Far-Field Dynamics of Object Pairs

In Sec. 3.2 we have studied the far-field trajectories of object pairs. In this Appendix we elaborate on the equations governing these trajectories in the case of spheroids, and on the numerical scheme that we have used to study the case of stokeslets objects.

D.1 Spheroid Parameters

Here we provide more details on the derivation of Eq. (3.11)-Eq. (3.12), together with indicating the specific parameters used for Fig. 3.4. Eq. (3.8)-Eq. (3.10) contain the single-object-dependent tensors, and the derivatives of the Oseen tensor, $\mathrm{G}_{ij}(\mathbf{R}) = 1/(8\pi R)(\delta_{ij} + R_i R_j/R^2)$. The object-dependent tensors of self-aligning spheroids are given in Appendix C. There, we consider a spheroid whose principal axes are $(\kappa^{-1}p, \kappa^{-1}p, p)$, and whose forcing point is displaced along the symmetry axis by a distance χp from the center. The system studied in Chapter 3, which is depicted in the left panel of Fig. 3.3, is characterized by a different representation where $\ell = 2p$ and $h = \chi p$.

The parameters β, ζ and α in Eq. (3.11)-Eq. (3.12) can be found by inserting the object-dependent tensors of a tilted, self-aligning spheroid into Eq. (3.8)-Eq. (3.10). The tilted tensors are given by evaluating the tensors in Appendix C with the orientation $\hat{\mathbf{n}} = (\theta, 0, -1)$. In particular, one finds that α and ζ change linearly with h. The trajectories presented in Fig. 3.4 correspond to spheroids with aspect ratio of 4. The dash-dotted green and dotted blue curves, respectively, are solutions to Eq. (3.11)–Eq. (3.12) with $h = 0$ (which gives $\beta \approx 1$, α, $\zeta = 0$) and $h \approx 0.31$ ($\beta \approx 0.6$, $\alpha \approx 1.25$, $\zeta \approx 0.95$).

D.2 Integration Scheme for Objects of Irregular Shape

Here we introduce the integration scheme used in Chapter 3 for the far-field dynamics of two irregular objects. This scheme is different from the one in Chapter 2 (outlined in Sec. 2.3.2) in several aspects: (*i*) It is restricted only to far-field dynamics, as only the first two multipoles of the pair-mobility matrix are considered; (*ii*) Instead of explicit integration, we solve a set of coupled non-linear, first-order ODEs using a Matlab routine. This method is more efficient as the hydrodynamic responses of each object are found only once, for a given orientation, instead of at any time step. On the other hand, it is less stable, as the ODE solver does not ensure normalization of the 4-vectors representing orientations. However, this latter stability issue has negligible effects on the repulsive trajectories studied in Chapter 3, unless at very long times.

The dynamics of a symmetric system comprising two spheroids (Fig. 3.3) can be described by the reduced equations, Eq. (3.11)-Eq. (3.12), for one angle $\theta(t)$ and one-dimensional separation $x(t)$. However, in the general case of two irregular objects we are compelled to integrate the full far-field equations, Eq. (3.8)-Eq. (3.10). Below we describe the details of the integration scheme.

The coordinate space includes the separation vector $\mathbf{R}$ and orientational parameters for each object, these are represented by Euler-Rodriguez 4-parameters (or unit quaternions), $(\Gamma^a, \mathbf{\Omega}^a)$ and $(\Gamma^b, \mathbf{\Omega}^b)$. The tensorial properties of a given object, such as the matrix $\mathbb{A}$ or the tensor of rank 3 Π, are calculated only once, in a reference frame affixed to the object. These properties can be derived explicitly for stokeslets objects (Sec. 2.3.1) or self-aligning spheroids Sec. D.1.

Knowing the properties in the body frame, e.g., $\mathbb{A}_{(b)}$ or $\Pi_{(b)}$, one can use a rotation transformation to calculate them in any orientation $(\Gamma, \mathbf{\Omega})$:

$$\mathbb{A}_{ij}(\Gamma, \mathbf{\Omega}) = \mathbb{R}_{il}(\Gamma, \mathbf{\Omega})\mathbb{A}_{(b),lm}\mathbb{R}^T_{mj}(\Gamma, \mathbf{\Omega}),$$

$$\Pi_{ijk}(\Gamma, \mathbf{\Omega}) = \mathbb{R}_{im}(\Gamma, \mathbf{\Omega})\Pi_{(b),mls}\mathbb{R}^T_{lj}(\Gamma, \mathbf{\Omega})\mathbb{R}^T_{sk}(\Gamma, \mathbf{\Omega}),$$

where

$$\mathbb{R}_{ij}(\Gamma, \mathbf{\Omega}) = (1 - 2\Omega^2)\delta_{ij} + 2\Gamma\epsilon_{ikj}\Omega_k + 2\Omega_i\Omega_j$$

is the rotation matrix which is a polynomial in the orientational parameters.

Finally, the equations for the evolution of $(\mathbf{R}, \Gamma^a, \mathbf{\Omega}^a, \Gamma^b, \mathbf{\Omega}^b)$ can be written using Eq. (3.8), and Eq. (3.9)–Eq. (3.10) together with the linear relation between angular velocity and time derivative of the orientation parameters (see Sec. 1.7)

$$\begin{pmatrix} \dot{\Gamma} \\ \dot{\mathbf{\Omega}} \end{pmatrix} = \frac{1}{2} \begin{pmatrix} 0 & -\boldsymbol{\omega}^T \\ \boldsymbol{\omega} & \boldsymbol{\omega}^\times \end{pmatrix} \begin{pmatrix} \Gamma \\ \mathbf{\Omega} \end{pmatrix}. \tag{D.1}$$

Appendix E

The Averaged Response Tensor Φ

Below we explain the emergence of an effective, averaged response tensor Φ for self-aligning objects. This response tensor is at the core of the theory presented in Chapter 4. (This averaged tensor is not identical to the hydrodynamic tensor Φ discussed in Chapter 2 and Appendix B).

The anisotropic response of self-aligning objects to a weak external flow is captured by the effective hydrodynamic tensor Φ in Eq. (4.3). This tensor can be derived from the motion of an isolated object in Stokes flow. Specifically, one should consider the motion of a single rigid object subjected to external force $\mathbf{F}$, and embedded in external flow gradient $\mathbf{E}$. This response encapsulates the two effects that contribute to the far-field dynamics studied in Sec. 3.2.3—gliding response and direct pair HI (in the case of self-aligning spheroids, these two effect are represented by the parameters β and ζ in Eq. (3.11).) . Below, we summarize the main equations from which Φ can be extracted for general self-aligning objects. In addition, we specialize to a simple example of self-aligning spheroids, for which we derive Φ explicitly.

E.1 Instantaneous Response under External Force and Flow

First, we write down the general equations governing the aforementioned hydrodynamic problem. The object is subjected to an external force $\mathbf{F} = -\hat{\mathbf{z}}F$, and placed in an external flow $\mathbf{u}(\mathbf{r}) = \mathbf{r}^T \cdot \mathbf{E}$, where $\mathbf{r}$ is measured from the forcing point, i.e., the point about which the external torque vanishes. We indicate the object's orientation by a set of parameters $\mathbf{Q}$, e.g., $\mathbf{Q}$ can refer to three Euler angles or a unit quaternion as has been done throughout this Thesis. Following Chapter 3, the instantaneous linear and angular velocities of the object, $\mathbf{V}$ and $\boldsymbol{\omega}$,

are given as a linear response to the external fields [24],

$$V_i = -\frac{1}{6\pi\eta\ell}A_{i3}(\mathbf{Q})F + \ell\Pi_{ijk}(\mathbf{Q})E_{kj}, \tag{E.1}$$

$$\Omega_i = -\frac{1}{8\pi\eta\ell^2}T_{i3}(\mathbf{Q})F + \left(\Psi_{ijk}(\mathbf{Q}) - \frac{1}{2}\epsilon_{ijk}\right)E_{kj}, \tag{E.2}$$

The velocity $\mathbf{V}$ in Eq. (E.1) refers to the velocity of the forcing point. Eq. (E.2) is a nonlinear equation for the object's orientation (the relation between $\partial_t\mathbf{Q}$ and $\boldsymbol{\omega}$ is given Appendix D.2 for the case of a unit quaternion representation). The translational motion, described by Eq. (E.1), varies in time as the object rotates.

If $\mathbf{E} = 0$, the object's eigendirection $\hat{\mathbf{n}}$ is aligned with the forcing direction and the object rotates about $\hat{\mathbf{n}}$ with a constant rate $\omega^0 = \lambda_3 F$. The ultimate rotation leads to a helical translational motion (dictated by Eq. (E.1)), where on average, the object translates in the direction of the force. The case of a weak external flow gradient results in tilted dynamics, as was shown in the context of pair-hydrodynamic interaction in Chapter 3. The presence of external flow affects the translational motion directly through the tensor Π, and indirectly due to the orientational motion modified by the tensor $\Psi - 1/2\epsilon$. When $(\Psi + 1/2)E \ll t_{\text{align}}^{-1}$, the aligning behavior and helical trajectory, corresponding to the case of $\mathbf{E} = 0$, are perturbed. In particular, the object preforms a tilted helical motion, where the averaged eigendirection $\bar{\mathbf{n}}$ and the averaged linear velocity $\bar{\mathbf{V}}$, both have components perpendicular to the direction of the force; see Fig. 3.4. This perturbed motion can be analyzed by solving Eq. (E.1) and Eq. (E.2), where Π and Ψ are constants obtained by averaging over the rotations in the (unperturbed) aligned state. Essentially, the tilted helical dynamics can be characterized as a linear response, i.e., $\bar{n}_i = (\eta\ell^2/F)\Sigma_{iks}E_{sk}$ and $\bar{V}_i = \ell\Phi_{iks}E_{sk}$, where Σ and Φ depend solely on the tensors $\mathbb{A}$, $\mathbb{T}$, Π and Ψ. The red curves in Fig. 3.4 illustrate such an averaged linear response in the case of self-aligning sparse objects.

E.2 Self-Aligning Spheroids

Let us now specialize to the case of self-aligning spheroids, which can be treated analytically. We consider a spheroid whose principal axes are $(\kappa^{-1}p, \kappa^{-1}p, p)$, as depicted in the inset of Fig. 4.3. The spheroid is subjected to an external force at a point which is displaced along the symmetry axis by a distance χp from the center, and embedded in an external flow gradient $\mathbf{E}$, which is measured about the forcing point. The spheroids orientation is represented by its eigendirection, $\hat{\mathbf{n}}$, which is directed from the center to the forcing point (indicated by a red dot in Fig. 4.3). The hydrodynamic tensors in Eq. (E.1) and Eq. (E.2) refer to the case where the object's *origin* is the forcing point. For self-aligning spheroids, these tensors are given as a linear transformation from the tensors that correspond to choosing the origin to be the spheroid's center, as given in Appendix C.

The linear velocity of the forcing point is given by

$$V_i = -F\mathbb{A}^c_{iz}(\hat{\mathbf{n}}) + \chi p\,(\boldsymbol{\omega}\times\hat{\mathbf{n}})_i - \chi p\hat{n}_k E_{ki}, \tag{E.3}$$

where $\mathbb{A}^c$ is given in Eq. (C.1). The spheroid's orientational dynamics is given by

$$\omega_i = -\frac{\alpha F}{\eta p^2}\epsilon_{il3}\hat{n}_l + \left(\Psi_{ijk}(\hat{\mathbf{n}}) - \frac{1}{2}\epsilon_{ijk}\right)E_{kj}, \tag{E.4}$$

where we use the twist matrix given in Eq. (C.7), and $\alpha = \chi S_\perp(\kappa)/(8\pi)$ is the alignability parameter. Eq. (E.4) leads to the nonlinear equation for the dynamics of eigendirection $\hat{\mathbf{n}}$,

$$\partial_t\hat{n}_i = \epsilon_{iks}\omega_k\hat{n}_s. \tag{E.5}$$

If $\mathbf{E} = 0$, then the eigendirection and the translational velocity will be ultimately directed along the $-\hat{\mathbf{z}}$ axis,

$$\hat{\mathbf{n}}^0 = -\hat{\mathbf{z}}; \quad \omega^0 = 0; \quad V_i^0 = -\frac{F}{6\pi\eta p}A^c_\parallel(\kappa)\delta_{i3}.$$

This is the self-aligning motion of the isolated object. In the case of weak external flow, i.e.,

$$\eta p^2\psi E \ll \alpha F, \tag{E.6}$$

the dynamics reaches a state where $\hat{\mathbf{n}}$ is slightly tilted from the forcing direction, $\hat{\mathbf{n}} = -\hat{\mathbf{z}} + \mathbf{n}^\perp$. The asymptotic solution can be found by setting $\boldsymbol{\omega} = 0$ in Eq. (E.4) and approximating $\Psi_{iks}(\hat{\mathbf{n}}) = \Psi_{iks}(-\hat{\mathbf{z}})$, which gives

$$\epsilon_{il3}n_l^\perp = \frac{\eta p^2}{\alpha F}\left(\Psi_{ijk}(-\hat{\mathbf{z}}) - \frac{1}{2}\epsilon_{ijk}\right)E_{kj}, \tag{E.7}$$

or

$$n_i^\perp = \frac{\eta p^2}{\alpha F}\epsilon_{i3m}\left(\Psi_{mjk}(-\hat{\mathbf{z}}) - \frac{1}{2}\epsilon_{mjk}\right)E_{kj}. \tag{E.8}$$

Next, let us consider the perturbed translational velocity in Eq. (E.3). Up to linear order in E we have

$$V_i - V_i^0 = \frac{F}{6\pi\eta p}\left(A^c_\parallel(\kappa) - A^c_\perp(\kappa)\right)n_i^\perp + \chi p\hat{z}_k E_{ki}. \tag{E.9}$$

Finally, substituting in Eq. (E.9) the final orientation given in Eq. (E.8), we find

$$V_i - V_i^0 = \frac{p\beta}{\alpha}\epsilon_{i3m}\left(\Psi_{mjk}(-\hat{\mathbf{z}}) - \frac{1}{2}\epsilon_{mjk}\right)E_{kj} + \chi p\hat{z}_k E_{ki} + O(E^2), \tag{E.10}$$

where $\beta = \left(A^c_\parallel(\kappa) - A^c_\perp(\kappa)\right)/(6\pi)$ is the gliding parameter of the object. To summarize, $V_i - V_i^0 = \ell\Phi_{ijk}E_{kj} + O(E^2)$ with

$$\Phi_{ijk} = \frac{p}{\ell}\chi\delta_{ij}\delta_{3k} + \frac{p}{\ell}\frac{\beta}{\alpha}\epsilon_{i3m}\left(\Psi_{mjk}(-\hat{\mathbf{z}}) - \frac{1}{2}\epsilon_{mjk}\right), \tag{E.11}$$

where we take the typical linear size of the spheroid as $\ell = \kappa^{-2/3} p$, since in the definition of ξ in Eq. (4.6) we assume the relation $c_0 \ell^3 \sim \varphi$.

Here we report the following asymptotic values for an extremely oblate spheroid ($\kappa \ll 1$), a sphere ($\kappa = 1$), and an extremely prolate spheroid ($\kappa \gg 1$):

$$\alpha(\kappa, \chi) \equiv \chi S_\perp(\kappa)/(8\pi) = \begin{cases} \frac{3\chi\kappa^3}{32} & , \kappa \ll 1 \\ \frac{\chi}{8\pi} & , \kappa = 1 \\ \frac{3\chi \ln(\kappa)}{8\pi} & , \kappa \gg 1 \end{cases}, \tag{E.12}$$

$$\beta(\kappa) \equiv \frac{A^c_\parallel(\kappa) - A^c_\perp(\kappa)}{6\pi} = \begin{cases} -\frac{\kappa}{32} & , \kappa \ll 1 \\ 0 & , \kappa = 1 \\ \frac{\ln(\kappa)}{8\pi} & , \kappa \gg 1 \end{cases}, \tag{E.13}$$

$$\gamma(\kappa, \chi) \equiv \Phi_{zzz} - \Phi_{z\perp\perp} - \Phi_{\perp\perp z} = \begin{cases} -\frac{\kappa^{2/3}}{3\chi} & , \kappa \ll 1 \\ 0 & , \kappa = 1 \\ \frac{\kappa^{2/3}}{3\chi} & , \kappa \gg 1 \end{cases}. \tag{E.14}$$

For extremely oblate or prolate spheroids, in the limit of $\chi \to 0$ one finds that $|\gamma| \to \infty$; however, in this limit $\alpha \to 0$ and the assumption of weak external flow gradient in Eq. (E.6) breaks; see discussion on this issue in Sec. 5.2.

Appendix F

Real Space Correlations in the Sedimentation of Irregular Objects

Below we summarize the detailed calculations yielding the real space correlations that are given in Sec. 4.2.1.

F.1 Total and Direct Density-Density Correlation Functions

The density-density correlations are the inverse Fourier transform of the suspension's static structure factor:

$$\langle c(0)c(\mathbf{r})\rangle = c_0 \int \frac{d^3\mathbf{q}}{(2\pi)^3} S(\mathbf{q}) e^{-i\mathbf{q}\cdot\mathbf{r}} = \frac{Nc_0}{D} \int \frac{d^3\mathbf{q}}{(2\pi)^3} \frac{q^2 e^{-i\mathbf{q}\cdot\mathbf{r}}}{q^2 + \xi^{-2}(q_\perp/q)^2}.$$

We rescale $r \to \xi R$ and define the rescaled total correlation function

$$h(\mathbf{R}) \equiv \frac{D\xi^3}{Nc_0}\langle c(0)c(\mathbf{R})\rangle = \int \frac{d^3\mathbf{q}}{(2\pi)^3} \frac{q^2 e^{-i\mathbf{q}\cdot\mathbf{R}}}{q^2 + (q_\perp/q)^2}. \tag{F.1}$$

We start with correlations along the direction of gravity

$$h(R\hat{\mathbf{z}}) = \int \frac{dq_\perp dq_z}{(2\pi)^2} \frac{(q_z^2+q_\perp^2)^2 q_\perp e^{-iq_z R}}{(q_z^2+q_\perp^2)^2 + q_\perp^2}. \tag{F.2}$$

Noticing that

$$\int \frac{q_\perp e^{-iq_z R}}{(q_z^2+q_\perp^2)^2 + q_\perp^2} dq_z = -\pi \mathrm{Im}\left(\frac{e^{-\sqrt{q_\perp^2 + iq_\perp} R}}{\sqrt{q_\perp^2 + iq_\perp}} \right), \tag{F.3}$$

we find

$$h(R\hat{\mathbf{z}}) = -\mathrm{Im}\left(\int \frac{dq_\perp}{4\pi}\left[(q_\perp^2+iq_\perp)^{3/2} - 2q_\perp^2\sqrt{q_\perp^2+iq_\perp} + q_\perp^4(q_\perp^2+iq_\perp)^{-1/2}\right]e^{-\sqrt{q_\perp^2+iq_\perp}R}\right). \tag{F.4}$$

In the limit $R\to\infty$, the first term is dominant over the others, which gives

$$\lim_{R\to\infty} h(R\hat{\mathbf{z}}) = -\mathrm{Im}\left(\int (iq_\perp)^{3/2}e^{-\sqrt{iq_\perp}R}\frac{dq_\perp}{4\pi}\right) = \frac{12}{\pi R^5}. \tag{F.5}$$

Next, consider correlations in the direction perpendicular to gravity

$$h(\mathbf{R}_\perp) = \int \frac{dq_z dq_\perp d\phi}{(2\pi)^3}\frac{(q_z^2+q_\perp^2)^2 q_\perp e^{-iq_\perp R\cos(\phi)}}{(q_z^2+q_\perp^2)^2+q_\perp^2} = \int \frac{dq_\perp dq_z}{(2\pi)^2}\frac{(q_z^2+q_\perp^2)^2 q_\perp}{(q_z^2+q_\perp^2)^2+q_\perp^2}J_0(q_\perp R), \tag{F.6}$$

where J_0 is the Bessel function of the first kind. In order to preform the following calculation we use the relations:

$$\frac{q_\perp}{(q_z^2+q_\perp^2)^2+q_\perp^2} = \mathrm{Re}\left(\frac{1}{q_\perp - if_-(q_z)} - \frac{1}{q_\perp+if_+(q_z)}\right)\frac{1}{f_+(q_z)+f_-(q_z)}, \tag{F.7}$$

with $f_\pm(q_z) = \frac{\sqrt{1+4q_z^2}\pm 1}{2}$, and

$$\mathrm{Re}\left(\int J_0(q_\perp R)\frac{dq_\perp}{q_\perp - ib}\right) = K_0(bR), \tag{F.8}$$

where K_0 is the modified Bessel function of the second kind. Integration over $q_\perp$ in Eq. (F.6) reads

$$h(\mathbf{R}_\perp) = M_1 + M_2 + M_3,$$

where

$$M_1 = \int \frac{dq_z}{(2\pi)^2}\frac{q_z^4}{f_+(q_z)+f_-(q_z)}\left[K_0(f_-(q_z)R) - K_0(f_+(q_z)R)\right], \tag{F.9}$$

$$M_2 = -\int \frac{dq_z}{(2\pi)^2}\frac{2q_z^2}{f_+(q_z)+f_-(q_z)}\left[f_-^2(q_z)K_0(f_-(q_z)R) - f_+^2(q_z)K_0(f_+(q_z)R)\right], \tag{F.10}$$

$$M_3 = \int \frac{dq_z}{(2\pi)^2}\frac{1}{f_+(q_z)+f_-(q_z)}\left[f_-^4(q_z)K_0(f_-(q_z)R) - f_+^4(q_z)K_0(f_+(q_z)R)\right]. \tag{F.11}$$

In the limit of $R\to\infty$, the first term dictates the leading order behavior

$$\lim_{R\to\infty} h(\mathbf{R}_\perp) = \int \frac{dq_z}{(2\pi)^2}q_z^4 K_0(q_z^2 R) = \frac{\Gamma^2(5/4)}{2\sqrt{2}\pi^2 R^{5/2}}.$$

Finally, we calculate the direct correlation function, $d(\mathbf{R})$, that can be written explicitly, and not in an integral form, as opposed to the total correlation function given above. The two

functions are related through the Ornstein-Zernike equation, which implies [108]

$$\tilde{d}(\mathbf{q}) = \frac{S(\mathbf{q}) - 1}{c_0 S(\mathbf{q})}.$$

In the case of $N = D$ we have

$$\tilde{d}(\mathbf{q}) = -\frac{\xi^{-2} q_\perp^2}{c_0 q^4},$$

and returning back to real space we get

$$d(\mathbf{r}) = -\frac{1}{c_0 \xi^2} \int \frac{d^3\mathbf{q}}{(2\pi)^3} \frac{q_\perp^2 e^{-i\mathbf{q}\cdot\mathbf{r}}}{q^4} = -\frac{1}{8\pi c_0 \xi^2 r} \left(1 + \frac{r_z^2}{r^2}\right). \tag{F.12}$$

F.2 Velocity Correlations

Let us now calculate the velocity two-point correlation function

$$\langle V_i(0) V_j(\mathbf{R}) \rangle = \frac{NF^2\xi}{D} \int \frac{dq^3}{(2\pi^3)} \frac{\tilde{G}_{iz}(\mathbf{q}) \tilde{G}_{jz}(-\mathbf{q}) q^2 e^{-i\mathbf{q}\cdot\mathbf{R}}}{q^2 + (q_\perp/q)^2}. \tag{F.13}$$

Separating to the cases of correlations along- and perpendicular to the direction of gravity we get the following expressions:

$$\langle V_z(0) V_z(\mathbf{R}) \rangle = \frac{NF^2\xi}{D} \int \frac{d^3\mathbf{q}}{(2\pi)^3} \frac{q_\perp^2}{q^4} \frac{q_\perp^2 e^{-i\mathbf{q}\cdot\mathbf{R}}}{q^4 + q_\perp^2}, \tag{F.14}$$

$$\langle V_\perp(0) V_\perp(\mathbf{R}) \rangle = \frac{\langle V_x(0) V_x(\mathbf{R}) \rangle + \langle V_y(0) V_y(\mathbf{R}) \rangle}{2} = \frac{NF^2\xi}{2D} \int \frac{d^3\mathbf{q}}{(2\pi)^3} \frac{q_z^2}{q^4} \frac{q_\perp^2 e^{-i\mathbf{q}\cdot\mathbf{R}}}{q^4 + q_\perp^2}. \tag{F.15}$$

Note that

$$\frac{1}{q^4} \frac{q_\perp^2}{q^4 + q_\perp^2} = \frac{1}{q^4} - \frac{1}{q^4 + q_\perp^2},$$

thus, the integrals become

$$\langle V_z(0) V_z(\mathbf{R}) \rangle = \frac{NF^2\xi}{D} \left(\int \frac{d^3\mathbf{q}}{(2\pi)^3} \frac{q_\perp^2}{q^4} e^{-i\mathbf{q}\cdot\mathbf{R}} - \int \frac{d^3\mathbf{q}}{(2\pi)^3} \frac{q_\perp^2}{q^4 + q_\perp^2} e^{-i\mathbf{q}\cdot\mathbf{R}} \right), \tag{F.16}$$

$$\langle V_\perp(0) V_\perp(\mathbf{R}) \rangle = \frac{NF^2\xi}{2D} \left(\int \frac{d^3\mathbf{q}}{(2\pi)^3} \frac{q_z^2}{q^4} e^{-i\mathbf{q}\cdot\mathbf{R}} - \int \frac{d^3\mathbf{q}}{(2\pi)^3} \frac{q_z^2}{q^4 + q_\perp^2} e^{-i\mathbf{q}\cdot\mathbf{R}} \right). \tag{F.17}$$

The first integral in the two expressions above can be solved explicitly

$$\int \frac{d^3\mathbf{q}}{(2\pi)^3} \frac{q_\perp^2}{q^4} e^{-i\mathbf{q}\cdot\mathbf{R}} = \frac{1}{8\pi R} \left(1 + \frac{R_z^2}{R^2}\right), \tag{F.18}$$

$$\frac{1}{2}\int \frac{d^3\mathbf{q}}{(2\pi)^3}\frac{q_z^2}{q^4}e^{-i\mathbf{q}\cdot\mathbf{R}} = \frac{1}{16\pi R}\frac{R_\perp^2}{R^2}. \tag{F.19}$$

Finally, the velocity correlations along the longitudinal and perpendicular directions can be found similarly to the integrals calculated above:

$$\frac{D\langle V_z(0)V_z(R\hat{\mathbf{z}})\rangle}{NF^2\xi} = \frac{1}{4\pi R} + \pi \mathrm{Im}\left(\int \frac{dq_\perp}{(2\pi)^2}\frac{q_\perp^2 e^{-\sqrt{q_\perp^2+iq_\perp}R}}{\sqrt{q_\perp^2+iq_\perp}}\right) \tag{F.20}$$

$$\frac{D\langle V_\perp(0)V_\perp(R\hat{\mathbf{z}})\rangle}{NF^2\xi} = -\frac{\pi}{2}\mathrm{Im}\left(\int \frac{dq_\perp}{(2\pi)^2}\sqrt{q_\perp^2+iq_\perp}e^{-\sqrt{q_\perp^2+iq_\perp}R}\right) \tag{F.21}$$

$$\frac{D\langle V_z(0)V_z(\mathbf{R}_\perp)\rangle}{NF^2\xi} = \frac{1}{8\pi R} + \int \frac{dq_z}{(2\pi)^2}\frac{f_-^2(q_z)K_0(f_-(q_z)R) - f_+^2(q_z)K_0(f_+(q_z)R)}{f_+(q_z)+f_-(q_z)} \tag{F.22}$$

$$\frac{D\langle V_\perp(0)V_\perp(\mathbf{R}_\perp)\rangle}{NF^2\xi} = \frac{1}{16\pi R} - \frac{1}{2}\int \frac{dq_z}{(2\pi)^2}\frac{q_z^2\left(K_0(f_-(q_z)R) - K_0(f_+(q_z)R)\right)}{f_-(q_z)+f_+(q_z)} \tag{F.23}$$

Appendix G

Validity of the Linear Theory in Chapter 4

This Appendix addresses the range of validity of the linear model for the sedimentation of self-aligning objects, which has been presented in Chapter 4. The original fluctuating hydrodynamics model, Eq. (4.4), contains an advective term which is linear in c, and a nonlinear one, $\sim c^2$, which underlies the LRFB model. The ratio between the two terms reads

$$\frac{\text{anisotropic linear term}}{\text{LRFB nonlinear term}} = \frac{\ell\gamma\tilde{G}(q)Fq^{-1}\tilde{c}c_0}{\tilde{G}(q)Fq\tilde{c}\tilde{c}} = \gamma\varphi(\ell q)^{-2}\frac{1}{\tilde{c}}. \tag{G.1}$$

The concentration fluctuations appearing in Eq. (G.1) can be related to the static structure factor

$$\tilde{c} \sim \sqrt{S} = \sqrt{N/D}\sqrt{\frac{1}{1+(\xi q)^{-2}}} \underset{q\xi\ll 1}{\to} \sqrt{N/D}q\xi. \tag{G.2}$$

The ratio in Eq. (G.1) is then proportional to $(q\xi)^{-3}$, and thus, much larger than 1 as $q \to 0$. Therefore, the linear term in Eq. (4.4) dominates the nonlinear one in both limits of small concentration fluctuations and small q. In these limits, the linear theory described by Eq. (4.5) is valid.

Bibliography

[1] W. B. Russel, D. A. Saville, and W. R. Schowalter, *Colloidal Dispersions* (Cambridge University Press, 1989).

[2] K. I. Morozov and A. M. Leshansky, Nanoscale **6**, 1580 (2014).

[3] M. E. Cates, D. Marenduzzo, I. Pagonabarraga, and J. Tailleur, PNAS **107**, 11715 (2010).

[4] J. Palacci, S. Sacanna, A. P. Steinberg, D. J. Pine, and P. M. Chaikin, Science **339**, 936 (2013).

[5] M. C. Marchetti, J. F. Joanny, S. Ramaswamy, T. B. Liverpool, J. Prost, M. Rao, and R. A. Simha, Rev. Mod. Phys. **85**, 1143 (2013).

[6] P. H. O'Farrell, J. Biol. Chem. **250**, 4007 (1975).

[7] S. A. Wren and R. C. Rowe, J. Chromatogr. A **603**, 235 (1992).

[8] R. Jean and L. Fan, in *Handbook of fluid dynamics, second edition*, edited by R. W. Johnson (Crc Press, 2016) Chap. 20.3, pp. 20–80.

[9] B. Comiskey, J. Albert, H. Yoshizawa, and J. Jacobson, Nature **394**, 253 (1998).

[10] H. Helmholtz, Ann. Phys. **243**, 337 (1879).

[11] M. v. Smoluchowski, Bull. Int. Acad. Sci. Cracovie **8**, 182 (1903).

[12] F. M. Jr., J. Colloid Interf. Sci. **34**, 210 (1970).

[13] M. Teubner, J. Chem. Phys. **76**, 5564 (1982).

[14] H. Brenner, Chem. Eng. Sci. **18**, 1 (1963).

[15] H. Brenner, Chem. Eng. Sci. **19**, 631 (1964).

[16] Marcos, H. C. Fu, T. R. Powers, and R. Stocker, Phys. Rev. Lett. **102**, 158103 (2009).

[17] M. Makino and M. Doi, Phys. Fluids **17**, 103605 (2005).

[18] R. Kuhn and S. Hoffstetter-Kuhn, Chromatographia **34**, 505 (1992).

[19] S. Sacanna, W. Irvine, P. M. Chaikin, and D. J. Pine, Nature **464**, 575 (2010).

[20] L. Landau and E. Lifshitz, *Fluid Mechanics, 2nd edition* (Pergamon Press, 1987).

[21] G. J. Hancock, P. Roy. Soc. Lond. A Mat. **217**, 96 (1953).

[22] H. Lorentz, Versl. Konigl. Akad. Wetensch. Amst **5**, 168 (1896).

[23] G. Stokes, Camb. Phil. Trans. **9**, 8 (1851).

[24] S. Kim and S. J. Karrila, *Microhydrodynamics: Principles and Selected Applications* (Mineola, N.Y. : Dover Publications, 2005).

[25] H. Diamant, J. Phys. Soc. Jpn. **78**, 041002 (2009).

[26] H. Lorentz, Abhandl. Theoret. Phys. Wetensch. Amst **1**, 23 (1907).

[27] J. Blake, Math. Proc. Cambridge **70**, 303 (1971).

[28] C. Pozrikidis, *Boundary integral and singularity methods for linearized viscous flow* (Cambridge University Press, 1992).

[29] J. R. Blake and A. T. Chwang, J. Eng. Math. **8**, 23 (1974).

[30] E. M. Purcell, Am. J. Phys **45**, 3 (1977).

[31] L. Landau and E. Lifshitz, *Statistical Physics, Part 1, 3rd edition* (Pergamon Press, 1980).

[32] J. Happel and H. Brenner, *Low Reynolds Number Hydrodynamics: with Special Applications to Particulate Media* (Martinus Nijhoff, The Hague, 1983).

[33] D. W. Condiff and J. S. Dahler, J. Chem. Phys. **44**, 3988 (1966).

[34] N. W. Krapf, T. A. Witten, and N. C. Keim, Phys. Rev. E **79**, 056307 (2009).

[35] O. Gonzalez, SIAM J. Appl. Math. **69**, 933 (2009).

[36] R. Cortez, L. Fauci, and A. Medovikov, Phys. Fluids **17**, 031504 (2005).

[37] J. García de la Torre and B. Carrasco, Biopolymers **63**, 163 (2002).

[38] A. Filippov, J. Colloid Interf. Sci. **229**, 184 (2000).

[39] B. Cichocki, B. U. Felderhof, K. Hinsen, E. Wajnryb, and J. Bławzdziewicz, J. Chem. Phys. **100**, 3780 (1994).

[40] B. Cichocki, M. L. Ekiel-Jeżzewska, and E. Wajnryb, J. Chem. Phys. **111**, 3265 (1999).

[41] A. Einstein, Ann. Phy. **324**, 371 (1906).

[42] M. Doi and M. Makino, Prog. Polym. Sci. **30**, 876 (2005), plenary Lectures World Polymer Congress, 40th {IUPAC} International Symposium on Macromolecules.

[43] O. Gonzalez, A. B. A. Graf, and J. H. Maddocks, J. Fluid Mech. **519**, 133 (2004).

[44] S. Strogatz, *Nonlinear Dynamics and Chaos: With Applications to Physics, Biology, Chemistry, and Engineering* (Studies in Nonlinearity, Westview, Cambridge, MA, 1994).

[45] M. Makino and M. Doi, J. Phys. Soc. Jpn. **72**, 2699 (2003).

[46] B. Moths and T. A. Witten, Phys. Rev. Lett. **110**, 028301 (2013).

[47] B. Moths and T. A. Witten, Phys. Rev. E **88**, 022307 (2013).

[48] J. A. Eaton, B. Moths, and T. A. Witten, Phys. Rev. E **94**, 032207 (2016).

[49] B. Carrasco and J. G. de la Torre, Biophys. J. **76**, 3044 (1999).

[50] P. Meakin and J. M. Deutch, J. Chem. Phys. **86**, 4648 (1987).

[51] J. Rotne and S. Prager, J. Chem. Phys. **50**, 4831 (1969).

[52] H. Yamakawa, J. Chem. Phys. **53**, 436 (1970).

[53] H. Brenner and M. E. O'Neill, Chem. Eng. Sci. **27**, 1421 (1972).

[54] A. Goldman, R. Cox, and H. Brenner, Chem. Eng. Sci. **21**, 1151 (1966).

[55] B. Felderhof, Physica A **89**, 373 (1977).

[56] D. J. Jeffrey and Y. Onishi, J. Fluid Mech. **139**, 261 (1984).

[57] S. Wakiya, J. Phys. Soc. Jpn. **20**, 1502 (1965).

[58] W. Liao and D. A. Krueger, J. Fluid Mech. **96**, 223 (1980).

[59] S. Kim, Int. J. Multiphase Flow **11**, 699 (1985).

[60] S. Kim, Int. J. Multiphase Flow **12**, 469 (1986).

[61] S. J. Karrila, Y. O. Fuentes, and S. Kim, J. Rheol. **33**, 913 (1989).

[62] T. Tran-Cong and N. Phan-Thien, Phys. Fluids **1**, 453 (1989).

[63] S. Ramaswamy, Adv. Phys. **50**, 297 (2001).

[64] T. M. Squires and M. P. Brenner, Phys. Rev. Lett. **85**, 4976 (2000).

[65] A. E. Larsen and D. G. Grier, Nature **385**, 230 (1997).

[66] Y. Sokolov, D. Frydel, D. G. Grier, H. Diamant, and Y. Roichman, Phys. Rev. Lett. **107**, 158302 (2011).

[67] H. Nagar and Y. Roichman, Phys. Rev. E **90**, 042302 (2014).

[68] T. Beatus, R. H. Bar-Ziv, and T. Tlusty, Phys. Rep. **516**, 103 (2012).

[69] T. M. Squires, J. Fluid Mech. **443**, 403 (2001).

[70] I. M. Jánosi, T. Tél, D. E. Wolf, and J. A. Gallas, Phy. Rev. E **56**, 2858 (1997).

[71] P. N. Segrè, E. Herbolzheimer, and P. M. Chaikin, Phys. Rev. Lett. **79**, 2574 (1997).

[72] J.-Z. Xue, E. Herbolzheimer, M. A. Rutgers, W. B. Russel, and P. M. Chaikin, Phys. Rev. Lett. **69**, 1715 (1992).

[73] D. Pine, J. P. Gollub, J. Brady, and A. Leshansky, Nature **438**, 997 (2005).

[74] A. J. C. Ladd, Phys. Fluids **9**, 491 (1997).

[75] J. Ham and G. Homsy, Int. J. Multiphas Flow **14**, 533 (1988).

[76] H. Nicolai and É. Guazzelli, Phys. Fluids **7**, 3 (1995).

[77] R. H. Davis and A. Acrivos, Annu. Rev. Fluid Mech. **17**, 91 (1985).

[78] É. Guazzelli and J. Hinch, Ann. Rev. Fluid Mech. **43**, 97 (2011).

[79] G. K. Batchelor, J. Fluid mech. **52**, 245 (1972).

[80] E. J. Hinch, in *Disorder and Mixing*, edited by Y. P. E. Guyon, J.-P. Nadal (Kluwer Academic Publishers, 1988) pp. 153–162.

[81] E. Hinch, J. Fluid Mech. **83**, 695 (1977).

[82] R. E. Caflisch and J. H. C. Luke, Phys. Fluids **28**, 759 (1985).

[83] A. J. C. Ladd, Phys. Rev. Lett. **76**, 1392 (1996).

[84] D. L. Koch, Phys. Fluids **6**, 2894 (1994).

[85] F. R. Cunha, G. C. Abade, A. J. Sousa, and E. J. Hinch, J. Fluids Eng. **124**, 957 (2002).

[86] L. Bergougnoux, S. Ghicini, É. Guazzelli, and J. Hinch, Phys. Fluids **15**, 1875 (2003).

[87] D. L. Koch and E. S. G. Shaqfeh, J. Fluid Mech. **224**, 275 (1991).

[88] A. Levine, S. Ramaswamy, E. Frey, and R. Bruinsma, Phys. Rev. Lett. **81**, 5944 (1998).

[89] M. P. Brenner, Phys. Fluids **11**, 754 (1999).

[90] X. Lei, B. J. Ackerson, and P. Tong, Phys. Rev. Lett. **86**, 3300 (2001).

[91] N.-Q. Nguyen and A. J. Ladd, J. Fluid Mech. **525**, 73 (2005).

[92] É. Guazzelli, Phys. Fluids **13**, 1537 (2001).

[93] J. H. C. Luke, Phys. Fluids **12**, 1619 (2000).

[94] P. J. Mucha, S.-Y. Tee, D. A. Weitz, B. I. Shraiman, and M. P. Brenner, J. Fluid Mech. **501**, 71 (2004).

[95] D. L. Koch and E. S. G. Shaqfeh, J. Fluid Mech. **209**, 521 (1989).

[96] A. A. Dahlkild, J. Fluid Mech. **689**, 183 (2011).

[97] P. Kumar and B. Ramarao, Chem. Eng. Commun. **108**, 381 (1991).

[98] M. A. Turney, M. K. Cheung, R. L. Powell, and M. J. McCarthy, AIChE J **41**, 251 (1995).

[99] B. Herzhaft, E. Guazzelli, M. B. Mackaplow, and E. S. G. Shaqfeh, Phys. Rev. Lett. **77**, 290 (1996).

[100] B. Metzger, J. E. Butler, and É. Gauzzelli, J. Fluid Mech. **575**, 307 (2007).

[101] D. Saintillan, E. Darve, and E. S. G. Shaqfeh, Phys. Fluids **17**, 033301 (2005).

[102] J. E. Butler and E. S. G. Shaqfeh, J. Fluid Mech. **468**, 205 (2002).

[103] K. Gustavsson and A.-K. Tornberg, Phys. Fluids **21**, 123301 (2009).

[104] B. Cichocki, M. L. Ekiel-Jeżewska, G. Nägele, and E. Wajnryb, Phys. Fluids **23**, 083303 (2011).

[105] P. M. Chaikin and T. C. Lubensky, *Principles of condensed matter physics* (Cambridge Univ Press, 2000).

[106] D. Forster, D. R. Nelson, and M. J. Stephen, Phys. Rev. A **16**, 732 (1977).

[107] S.-k. Ma and G. F. Mazenko, Phys. Rev. B **11**, 4077 (1975).

[108] S. Torquato and F. H. Stillinger, Phys. Rev. E **68**, 041113 (2003).

[109] A. Gabrielli, M. Joyce, and F. Sylos Labini, Phys. Rev. D **65**, 083523 (2002).

[110] L. Corte, P. M. Chaikin, J. P. Gollub, and D. J. Pine, Nature Phys. **4**, 420 (2008).

[111] J. H. Weijs, R. Jeanneret, R. Dreyfus, and D. Bartolo, Phys. Rev. Lett. **115**, 108301 (2015).

[112] D. Hexner and D. Levine, Phys. Rev. Lett. **114**, 110602 (2015).

[113] M. Florescu, S. Torquato, and P. J. Steinhardt, PNAS **106**, 20658 (2009).

[114] W. Man, M. Florescu, E. P. Williamson, Y. He, S. R. Hashemizad, B. Y. C. Leung, D. R. Liner, S. Torquato, P. M. Chaikin, and P. J. Steinhardt, PNAS **110**, 15886 (2013).

[115] E. Tjhung and L. Berthier, Phys. Rev. Lett. **114** (2015), 10.1103/PhysRevLett.114.148301.

[116] C. E. Zachary, Y. Jiao, and S. Torquato, Phys. Rev. Lett. **106**, 178001 (2011).

[117] H. Goldstein, *Classical Mechanics, 2nd ed.* (Addison-Wesley, Reading, MA, 1981).

[118] M. D. Shuster, J. Astronaut. Sci. **41**, 439 (1993).

[119] J. Vince, *Geometric algebra for computer graphics* (Springer Science & Business Media, 2008).

[120] J. B. Kuipers, *Quaternions and Rotation Sequences: A Primer with Applications to Orbits, Aerospace and Virtual Reality* (Princeton University Press, 2002).

[121] I. P. Omelyan, Comput. Phys. **12**, 97 (1998).

[122] D. J. Evans and S. Murad, Mol. Phys. **34**, 327 (1977).

[123] D. Rapaport, J. Comput. Phys. **60**, 306 (1985).

[124] R. Kutteh, J. Chem. Phys. , 174107 (2010).

[125] I. M. Ilie, W. J. Briels, and W. K. den Otter, J. Chem. Phys. **142**, 114103 (2015).

[126] L. D. Favro, Phys. Rev. **119**, 53 (1960).

[127] T. Goldfriend, H. Diamant, and T. A. Witten, Phys. Fluids **27**, 123303 (2015).

[128] H. Brenner, Chem. Eng. Sci. **19**, 599 (1964).

[129] H. Brenner, Chem. Eng. Sci. **19**, 703 (1964).

[130] I. L. Claeys and J. F. Brady, J. Fluid Mech. **251**, 411 (1993).

[131] W. B. Russel, E. J. Hinch, L. G. Leal, and G. Tieffenbruck, J. Fluid Mech. **83**, 273 (1977).

[132] T. Goldfriend, H. Diamant, and T. A. Witten, Phys. Rev. E **93**, 042609 (2016).

[133] F. P. Bretherton, J. Fluid Mech. **14**, 284 (1962).

[134] T. Goldfriend, H. Diamant, and T. A. Witten, Phys. Rev. Lett. **118**, 158005 (2017).

[135] P. Tong and B. J. Ackerson, Phys. Rev. E **58**, R6931 (1998).

[136] H. Nicolai, B. Herzhaft, E. Hinch, L. Oger, and E. Guazzelli, Phys. Fluids **7**, 12 (1995).

[137] S. Torquato, Phys. Rev. E **94**, 022122 (2016).

[138] L. Reed and F. Morrison, J. Colloid Interface Sci. **54**, 117 (1976).

[139] S. B. Chen and H. J. Keh, AIChE **34**, 1075 (1988).

[140] K.-L. Sun and W.-Y. Wu, Int. J. Multiph. Flow **21**, 705 (1995).

[141] D. Long and A. Ajdari, Phys. Rev. Lett. **81**, 1529 (1998).

תודות

בראש ובראשונה, אני רוצה להודות לפרופ׳ חיים דימנט על שהכיר לי את תחום המחקר של חומר מעובה רך, ועל ההנחיה והליווי שלו בארבע וחצי השנים האחרונות. חיים, תודה על שחלקת עימי את תהיותך הסקרניות ואת רעיונתך מעוררי ההשראה. לימדת אותי כיצד שאילת השאלות הפיסיקליות הנכונות יכולה להביא תוצאה פשוטה לפתיחת חלון לכיוונים נוספים או לחילופין, לרמוז מתי הגיעה העת לעבור לאתגר הבא. אני חב לך תודה על נחמדותך האופיינית לך וההנחיה המסורה שלך בדרכי למחקר עצמאי.

אני חש בר מזל על האפשרות להודות לפרופ׳ תומאס א. וויטן על שיתוף פעולה פורה ודיונים מאירי עיניים. אני אסיר תודה על שהייתה לי האפשרות המיוחדת לעקוב ולהיות מושפע מקו המחשבה העמוק והיצירתי של טום.

ברצוני גם להודות לחבריי ועמיתיי עוז, יוליה וחן על דיונים מפרים והצעות מועילות.

אני מודה להוריי אֹרנה ודֹב, ולאחיי אמיר, רועי וניר, על העידוד שלהם והתמיכה. ולבסוף, אך חשוב מכל, לאשתי, love of my life, נטע– את היית שם לאורך כל הדרך, במהלך הרגעים הפסימיסטיים הרבים שלי וגם ברגעים האופטימיים הנדירים, שומרת על שפיותי לאורך המסע. לבסוף, אני לא יכול להשלים את רשימת התודות מבלי להזכיר את בתי רעות, שנכנסה לחיי לפני כמה שבועות והעניקה לי פרספקטיבה חדשה על החיים.

בחלק השלישי אנו מראים כי לאפקטים הייחודיים בתנועתם של זוג אובייקטים א-סימטריים ישנה השפעה על הדינמיקה הרב-גופית של קולואידים תחת כוח חיצוני. עבור תרחיף שוקע המכיל אובייקטים מתיישרים-עצמאית, התגובה הלא-איזוטרופית של האובייקטים לזרימה, המושרית מנטיית האובייקטים להתיישר עם כוח הכובד, פועלת כמנגנון שבאופן ישיר מקטין פלוקטואציות בצפיפות ובמהירות התרחיף. מנגנון זה מאפשר לתרחיף להימנע מהפלוקטואציות האנומליות של תרחיפים עם ספרואידים סימטריים. אנו מראים, על ידי שימוש במודל סטטיסטי מחוץ לשיווי משקל (fluctuating hydrodynamics) כיצד הדיכוי של אי-הומוגניות יוצר מבנה היפר-אחיד עם קורלציות ארוכות טווח. עבור מקרים מסויימים, התגובה הלא-איזוטרופית פועלת בכיוון ההפוך ומובילה לחוסר יציבות של תרחיף שוקע הומוגני.

על כן, הממצאים של תזה זו מצביעים באופן ברור על הבדלים איכותיים– הן ברמה הדו-גופית והן ברמה הקולקטיבית– בין הדינמיקה תחת כוח חיצוני של תרחיפים של חלקיקים בעלי צורה סימטרית לבין כאלה המכילים אובייקטים א-סימטריים.

תקציר

תרחיפים (קולואידים) הינם מערכות המורכבות מחלקיקים מזוסקופיים (10 ננומטר-10 מיקרון בגודלם) המפוזרים בנוזל מולקולרי צמיג. מחקרים קודמים על הדינמיקה של זוג, או הרבה, אובייקטים בתרחיף תחת כוח חיצוני התמקדו בחלקיקים סימטריים כדוגמת כדורים או ספרואידים. בחינה מקיפה במקרה של קולואידים א-סימטריים הוצגה לאחרונה ברמת האובייקט הבודד עבורה הדגימו כיצד הצימוד בין תנועה קווית, תנועה סיבובית והכוח החיצוני יכול להניב סוג חדש של הסעה מבוקרת. בתזה זו אני בוחן את האינטראקציות המושרות ע"י זרימת הנוזל (אינטראקציות הידרודינמיות) בין אובייקטים בעלי צורה כלשהי הנעים בהשפעת כוח חיצוני, ובודק את ההשלכות שלהן על יישור קולואידים ועל התנועה הקולקטיבית של תרחיפים לא בראוניים וא-סימטריים.

בחלק הראשון של העבודה אנו חוקרים את האינטראקציה ההידרודינמית בין שני אובייקטיים בעלי צורה כלשהי המוסעים בנוזל צמיג, בגבול שבו מספר ריינולדס מתאפס. אנו חוקרים את המאפיינים הכלליים והסימטריות של מטריצת המוביליות הדו-גופית, המתארת את התגובה המיידית של שני האובייקטים. אנחנו מנתחים אנליטית את הסדר המוביל (מונופולרי ודיפולרי) של האינטראציה, המשפיע על המהירות הקווית והסיבובית של האובייקטים במרחקים גדולים. אנו מתמקדים, באופן פרטני, באובייקטים "המתיישרים-עצמאית"– קבוצה גדולה של אובייקטים בעלי צורה א-סימטרית המתיישרים עם כוח חיצוני בכיוון קבוע, ואף ניתנים לסינכרון עם פרוטוקול כוח המשתנה בזמן. אנחנו מוכיחים שהאינטראקציה ההידרודינמית המיידית מחלישה באופן לינארי את היישור ההדדי בין שני אובייקטים מסוג זה. השפעותיה של האינטראקציה ההידרודינמית לאורך זמן מודגמות באופן מפורש ע"י חישוב נומרי של הדינמיקה של אובייקטים המתיישרים-עצמאית, הממודלים בעזרת אוסף של ארבע נקודות כוח. בנוסף להשפעה על יישור האובייקטים, אנו מוצאים כי הקשר בין האינטראקציה הסיבובית והקווית, ברוב המקרים, מוביל עם הזמן לדחייה בין שני האובייקטים. כתוצאה מכך, בהפעלת פרוטוקול כוח משתנה בזמן, האינטראקציה הדו-גופית, המקטינה את היישור ההדדי בין שני אובייקטים, נחלשת ככל שהאובייקטים מתרחקים זה מזה והמצב המסונכרן מושב על כנו.

תוצאות אלו– התנועה הקווית היחסית המתקבלת כתגובה מיידית לכוח והדחייה האפקטיבית עם הזמן– מובילים אותנו בחלקה השני של העבודה לבחון במפורט את ההשלכות של האינטראקציה ההידרודינמית על הטרנסלציה היחסית בין שני קולואידים מוסעים. עובדה ידועה היא, שבמקרה של שני כדורים זהים השוקעים בנוזל אינסופי האינטרקציה לא מייצרת תנועה קווית יחסית. אנו מדגימים, באופן כללי יותר, שאינטראקציה אפקטיבית זו מתאפסת כאשר ישנה סימטריה מרחבית להיפוך- לדוגמה, במקרה של זוג אננטיומרים המוצבים בתמונת ראי אחד של השני. אנו מראים ששבירת הסימטריה להיפוך כתוצאה מגבולות המערכת מסבירה את התנועה היחסית בין כדורים שנצפתה בניסויים במערכות מתוחמות. עקרון כללי זה של סימטריה מספק גם תחזיות לאינטראקציות אפקטיביות בקונפיגורציות מתוחמות אחרות . בנוסף, אנו בוחנים לעומק את התנועה היחסית המתפתחת בזמן בין זוג אובייקטים המתיישרים-עצמאית. אנו מראים כיצד הדחייה הטיפוסית עבור קבוצה זו של אובייקטים שונה באופן איכותי בהשוואה למקרה הסימטרי יותר של שני ספרואידים. המרחק ההדדי בין שני האובייקטים, עבור כל אחד מהמקרים הללו, מתאים לחוק חזקה שונה עבור ההתפתחות האסימפטוטית עם הזמן.

מוקדש לזכרם של הסבים והסבתות שלי:
שמואל והדסה אירנה גולדפרייזד, אליהו ודבורה זקל.

— אֲצֵא לִי עַל כֵּן, בְּמְעִיל קַיִץ פָּשׁוּט, לְטַיֵּל בֵּין פִּילֵי הַשָּׁמַיִם. ("אל הפילים", נתן אלתרמן)

עבודה זו נעשתה בהדרכתו של

פרופסור חיים דימנט

בית הספר לכימיה, אוניברסיטת תל אביב

הפקולטה למדעים מדוייקים

ע"ש ריימונד ובברלי סאקלר

בית הספר לפיסיקה ואסטרונומיה

חיבור לשם קבלת התואר "דוקטור לפילוסופיה"

דינמיקה של תרחיפים תחת כוח חיצוני

הוגש לסנאט של אוניברסיטת תל אביב על ידי

תומר גולדפריינד

מנחה: פרופ' חיים דימנט

ינואר 2017